AN ABSTRACT OF THE THESIS OF

ChyiShiun Li for the degree of <u>Master of Science</u> in

<u>Electrical and Computer Engineering</u> presented on <u>November 21, 2002</u>.

Title:

<u>Radiation Effects in III-V Compound Semiconductor Heterostructure Devices.</u>

Redacted for Privacy

Abstract approved: _____

S. Subramanian

The radiation effects in III-V heterojunction devices are investigated in this thesis. Two types of heterojunction devices studied are InGaP/GaAs single heterojunction bipolar transistors (SHBTs) and GaN-based heterojunction light emitting diodes (LEDs). InGaP/GaAS HBTs are investigated for high energy (67 and 105 MeV) proton irradiation effects while GaN heterojunction LEDs are studied for neutron irradiation effects. A compact model and the parameter extraction procedures for HBTs are developed, and hence the $I_C - V_{CE}$ characteristics of pre- and post-irradiation HBTs can be simulated by employing the developed model.

HBTs are electrically characterized before and after proton irradiation. Overall, the studied HBT devices are quite robust against high energy proton irradiation. The most pronounced radiation effect shown in SHBTs is gain degradation. Displacement damage in the bulk of base-emitter space-charge region, leading to excess base current, is the responsible mechanism for the proton-induced gain degradation. The performance degradation depends on the operating current and is generally less at higher currents. Compared to the MBE grown devices, the MOVPE grown HBTs show superior characteristics both in initial performance and in proton irradiation

hardness. The 67 MeV protons cause more damage than 105 MeV protons due to their higher value of NIEL (non-ionizing energy loss). The HBT I-V characteristics of pre- and post-irradiated samples can be simulated successfully by employing the developed model.

GaN heterojunction LEDs are electrically and optically characterized before and after neutron irradiation. Neutron irradiation causes changes in both the I-V characteristic and the light output. Atomic displacement is responsible for both electrical and optical degradation. Both electrical and optical properties degrade steadily with neutron fluence producing severe degradation after the highest fluence neutron irradiation. The light output degrades by more than 99% after 1.6×10^{15} n/cm^2 neutron irradiation, and the radiation damage depends on the operating current and is generally less at higher currents.

Radiation Effects in III-V Compound Semiconductor Heterostructure Devices

by

ChyiShiun Li

A THESIS

submitted to

Oregon State University

in partial fulfillment of
the requirements for the
degree of

Master of Science

Presented November 21, 2002
Commencement June 2003

<u>Master of Science</u> thesis of <u>ChyiShiun Li</u> presented on <u>November 21, 2002</u>

APPROVED:

Redacted for Privacy

———
Major Professor, representing Electrical and Computer Engineering

Redacted for Privacy

———
Chair of the Department of Electrical and Computer Engineering

Redacted for Privacy

———
Dean of the Graduate School

I understand that my thesis will become part of the permanent collection of Oregon State University libraries. My signature below authorizes release of my thesis to any reader upon request.

Redacted for Privacy

———
ChyiShiun Li, Author

ACKNOWLEDGMENTS

TABLE OF CONTENTS

TABLE OF CONTENTS (Continued)

LIST OF FIGURES

LIST OF FIGURES (Continued)

LIST OF TABLES

Radiation Effects in III-V Compound Semiconductor Heterostructure Devices

1. INTRODUCTION

1.1. Background and motivation

There are a variety of radiation sources and environments to which electronic systems may be exposed. The one of most interest is space radiation [1]. Radiation in the space environment mainly comes from three categories: (1) the trapped particle belts (2) solar particle events and (3) cosmic rays. The radiation belts (Van Allen belt) consist primarily of electrons of up to a few MeV energy and protons of up to several hundred MeV energy. They are trapped in the Earth's magnetic field; their motion in the magnetic field consists of a gyration about the field lines, a bouncing motion between the magnetic mirrors found near the Earth's poles, and a drift motion around the Earth [2]. During solar events, large fluxes of energetic protons are produced which reach the earth. Such events are unpredictable in their time of occurrence, magnitude, duration or composition. Cosmic rays originate outside the solar system. They consist of protons (85%), alpha particles (14%) and heavy, energetic ions (1%) [3]. As a result, the proton is one of the most dominant particles in near-earth orbits in which most satellites are operated. Hence the proton radiation effects on space application devices deserve very careful consideration.

While traveling through a semiconductor, energetic particles present in radiation environments lose their energy by interacting with the atoms of the material

and through different scattering mechanisms. The two major consequences of energy transfer from radiation to semiconductor materials are ionization and atomic displacement [4]. In an ionization process, the energetic particles lose their energy to the electrons in semiconductors and insulators. The valence band electrons in the solid are excited to the conduction band and electron-hole pairs are produced. The production and subsequent trapping of the holes in oxide layers cause serious degradation in metal-oxide semiconductor field-effect transistors (MOSFETs). Atomic displacement occurs when a high energy particle traverses the solid materials and knocks an atom out of its equilibrium position in a crystal lattice. This struck and displaced atom, known as a "primary knock-on atom" (PKA), may collide many times with other atoms and produce a "cascade" of displacements. The displacement can cause various defects in semiconductors, such as vacancies, interstitials, anti-sites, and more complex defects. These defects may act as generation centers, recombination centers, traps, compensation centers and tunneling centers. In bipolar devices, the displacement damage plays an important role in the radiation-induced performance degradation. Thus, one should take a special consideration of the displacement damage when studying the radiation effects in bipolar devices.

Radiation effects in semiconductor devices are generally grouped into three categories: (1) total dose effects, (2) dose rate effects, and (3) single event effects [1]. The absorption of ionizing radiation in semiconductor devices is studied by the total dose effect. It serves as a measure to determine the total radiation dose at which the performance of a device degrades below a certain acceptable limit. Dose rate effect is used to characterize the radiation damage dependence on time variation of the radiation flux. The devices for space applications may receive relatively low dose rates while those used in nuclear weapons or nuclear reactors can encounter bursts of radiation in a very short period. Such devices may fail long before the device has

received the radiation limit specified by the total dose effect. On the other hand, the enhanced degradation of silicon devices under low dose rate conditions has also been reported, and has received considerable attention in the past few years. Single event effect (SEE) is caused by charge collection at sensitive nodes due to particle radiation. Protons and heavy ions are the sources of SEE in space. The SEE can cause logic upsets (soft errors) in memory elements, and even permanent failures such as gate ruptures in MOS devices. The main focus of this radiation effect study is total dose effect.

Radiation effects in silicon devices like bipolar junction transistors (BJTs) and metal oxide semiconductor field effect transistors (MOSFETs) have been extensively studied. In BJTs, current gain degradation and leakage are the most striking effects of radiation. Atomic displacement in the bulk of semiconductors and ionization in the oxide passivation layers are the two main causes of gain degradation. The displacement damage produces an increase in the number of recombination centers, which reduce minority carrier lifetime. The ionization introduces trapped charges and interface states which increase the minority carrier surface recombination velocity, and hence reduce the gain [4].

Compound semiconductor heterojunction devices are well-known for their superior electron transport properties and flexibility in band gap engineering. However, difficulties in fabrication made the heterostructure devices not commercially plausible until molecular beam epitaxy (MBE) and metal organic chemical vapor deposition (MOCVD) growth techniques were developed in the late 1970s and 1980s. Since then, a large number of III-V-based devices have been developed. Among them, one of the most important devices is the heterojunction bipolar transistor (HBT) which was originally proposed by Shockley in 1948. HBTs are similar to silicon-based bipolar junction transistors except for the wide band gap materials

employed in the emitter layer. The wide band gap emitter provides an additional potential barrier to prevent the back injection of holes from the base to the emitter. This in turn produces the very high emitter injection efficiency and current gain, impossible to achieve in a BJT. At the same time, due to this additional barrier, the emitter doping concentration can be reduced, and the base doping concentration can be significantly increased resulting in lower base resistance, smaller base-emitter junction capacitance, and shorter emitter charge storage time. With these advantages, HBT-based RF Integrated Circuits (RFICs) have gained wide acceptance by all major wireless equipment suppliers as the preferred technology, when performance, high-linearity, efficiency and price competitiveness are a premium. Over the past few years, HBT-based electronic systems have overtaken GaAs MESFET and silicon BJT-based products [6]. As a result, a rapidly growing number of HBTs are employed in high performance electronic communication systems on board commercial and military satellites.

The AlGaAs/GaAs-based HBT has been one of the great compound semiconductor success stories. Radiation effects in various III-V-based HBT devices have also been studied by numerous groups [7–12]. However, the majority of development and production programs of HBTs are now focusing on devices with an InGaP emitter layer. The $In_{0.49}Ga_{0.51}P$ material, which is lattice-matched to a GaAs substrate, offers a larger valence band offset ($E_v \sim 0.3$ eV) [13]. A large E_v at the InGaP/GaAs heterointerface better accommodates the increased Fermi level from the highly doped base and suppresses hole injection into the emitter. Secondly, the high etch selectivity between InGaP and GaAs makes the device processing easier. Moreover, InGaP has no DX center problem which occurs in aluminum-containing compounds. Finally, the InGaP HBT has low surface recombination velocity, and superior long-term reliability [14] [15]. Therefore, it can be expected that more

and more sophisticated InGaP/GaAs-based electronic systems will be employed on board satellites.

Gallium nitride (GaN) is a direct wide band gap III-V compound semiconductor that is a promising material for opto-electronic devices in the blue to UV range as well as for high power, high speed electronic devices. In 1994, Nakamura *et al.* in Nichia successfully developed GaN-based double heterojunction (DH) blue light emitting diodes (LEDs) which could increase optical storage density and are essential for full color display technologies. As a result, tremendous efforts have been put into the development of GaN based devices in recent years. It has been reported that GaN is two orders of magnitude less sensitive to proton irradiation than GaAs. However, limited work has been done on proton irradiation effects of GaN devices, and no work, to our knowledge, has been done on neutron irradiation effects in GaN-based LEDs. Thus, it is of great interest to investigate the response of GaN-based blue LEDs under neutron irradiation.

Considering the high cost of preparing, launching, and maintaining a satellite-based resource, it is very desirable to experimentally study the irradiation effects in these heterojunction devices in advance and to develop a systematic understanding of the relationship between the radiation-induced defects, the degradation mechanisms and the performance degradation of devices. With such an understanding of this relationship, the process and design engineers are in a much improved position to develop better device/circuit designs for greater reliability against radiation effects and a better hardness assurance test methodogy.

1.2. Organization of the study

This thesis presents the experimental study and theoretical modeling on proton-induced damage of GaInP/GaAs HBTs. In this study, various devices with

different emitter sizes and grown by different technologies are employed, in order to develop a systematic understanding of the radiation-induced effects in HBT devices. Through the experimental data analysis and parameter extraction, the mechanisms of device performance degradation can be better understood. An overview of the research work and the organization of the study is given below.

Chapter 2 introduces the basic concepts of HBTs. First, the materials, structures and performance of HBTs are briefly discussed. The experimental setup and measurement configurations used in electrical characterization of the BJT are then discussed. The compact models describing their operation are presented at the end.

Chapter 3 addresses the radiation-induced damage and the radiation effects in semiconductors. First, various types of radiation and radiation environments to which the semiconductor devices might be exposed are introduced. A brief overview of radiation effects as well as damage theory quantities in the semiconductors are then discussed.

Chapter 4 presents the experimental results of proton irradiation in In-GaP/GaAs HBTs. First, the experimental characterization of the device performance degradation is presented. Subsequently, the individual degradation is compared and analyzed through different structures and devices. Through parameter extraction, the theoretical modeling is discussed.

Chapter 5 presents the experimental results of neutron irradiation in GaN-based heterojunction LEDs. The experimental details of electrical and optical characterization are presented. The electrical and optical performance degradation is then discussed. Subsequently, the possible mechanisms responsible for the electrical and optical degradation are discussed.

Chapter 6 presents the conclusions of this study and suggestions for further research.

2. HETEROJUCTION DEVICE FUNDAMENTALS

2.1. Introduction

Heterostructures are the building blocks of many of the most advanced semiconductor devices presently being developed and produced. They are widely employed in high-performance optical devices such as room-temperature injection lasers, light-emitting diodes (LEDs) as well as in high-speed and high-frequency digital and analog devices [16–18]. A heterostructure is a semiconductor structure in which the chemical composition changes with position. The simplest heterostructure is a single heterojunction, which is a junction formed between two different semiconductors. Examples include junctions between InP and InGaAs semiconductors, junctions between GaAs and AlGaAs solid solutions, and junctions between Si and GeSi alloys.

The idea of using heterojunction in bipolar junction transistors was first suggested by Shockley in his 1948 patent. Kroemer later proposed a graded heterojunction as a wide band gap emitter [19]. However, the advantages of this combination were not appreciated because there was no suitable growing technology available at that time. Later, molecular beam epitaxy (MBE) and metal-organic chemical vapor deposition (MOCVD) were developed in the '70s and '80s, respectively. These growth techniques provide the reliable ability to grow the very abrupt heterointerface which is essential for high quality heterostructure devices. Since then, enormous efforts have been put into the development and research of material systems, growth methods, and structure design in HBTs for their superior properties and characteristics. As a result, HBT-based electronic systems have overtaken MESFET and

silicon BJT based products in wireless communication applications in the past few years [6].

In this chapter, first, a general introduction to the material systems, structures and performance of HBTs is given. This knowledge is essential to appreciate the beauty of HBTs. The setups for electrical characterization of HBT devices are subsequently described and models are introduced to explain the BJT's operation. After that, simple procedures for extracting the HBT parameters are described and the modified Ebers-Moll model is developed. Finally, the terminal current-voltage characteristics are simulated by employing the models developed and parameters extracted.

2.2. Heterojunction materials

A heterojunction forms when two different semiconductors are placed in contact. The electrical characteristics of the heterojunction depend on the quality of the heterointerface. The interface departs from the ideal structure when two different arbitrary semiconductors are used in the heterojunction. Thus, the defects are formed at the interface. The most obvious cause of such defects is the mismatch between the lattices of the participating semiconductors. The lattice constants of GaAs and AlAs are nearly equal, so these materials fit together quite well. A high quality heterointerface of GaAs/AlAs is expected. On the contrary, for SiGe devices, the lattice constants of Si and Ge differ significantly, so that over a large area of the heterojunction interface, not every Si atom will find a Ge atom to bond with. This situation produces defects in the form of dislocations. Such dislocations usually affect the electrical characteristics of the system by creating localized states which trap charge carriers. If the density of such interfacial states is sufficiently large, they will dominate the electrical properties of the interface. This is what usually happens

at the poorly engineered heterojunction interfaces. Hence, close lattice match between two participating materials is required to obtain a high quality heterojunction free of defects.

However, if one of the materials forming the heterojunction is made into a sufficiently thin layer, the lattice mismatch can be accommodated as strain in the thin layer. Therefore, some moderately lattice-mismatched systems, such as Si/Si_xGe_{1-x}, can be employed in certain devices such as high electron mobility transistors (HEMTs). Such lattice-mismatched compound systems are called pseudomorphic systems.

The participating materials on each side of the junction can be chemically similar or dissimilar. If both constituents contain elements from the same column of the periodic table, they are chemically similar. It is also possible to grow heterojunctions between chemically dissimilar semiconductors. GaAs/ZnSe is one of these examples. Such junctions were studied early in the development of heterostructure technology, but there are some problems with such junctions. Based upon simple models of the electronic structure of these junctions, one would expect a high density of localized interface states due to the under- or over-satisfied chemical bonds across such a junction [20]. Moreover, the constituents of each semiconductor can act as dopants when incorporated into the other material. Thus any inter-diffusion across the junction produces serious electrical effects which are difficult to control. For these reasons, much effort has been focused on chemically matched systems. The two most important examples are $AlGaAs/GaAs$ and $InP/In_{0.53}Ga_{0.47}As$ heterojunctions.

If the two materials forming a heterojunction are made of a continuum of solid solution, such as the one between GaAs and AlAs, the transition of the chemical composition in the junction need not occur abruptly. Instead, this transition may

be graded over some specified distance. That is, the composition parameter x in $Al_xGa_{1-x}As/GaAs$ might be some continuous function of the position. These kind of junctions are called graded heterojunctions. Such heterojunctions have some desirable properties that we will discuss later.

By convention, in a heterojunction the majority carrier type of the wide band gap material is labeled by an upper case letter, while that of the smaller band gap material is labeled by a lower case letter. If the carrier types are the same on both sides of heterojunction, such as N-n or P-p, it is called an isotype heterojunction. If they are not, such as N-p or P-n, an anisotype junction forms.

A single heterojunction bipolar transistor (SHBT) structure can be simply described by using a wider band gap material for the emitter in a bipolar junction transistor (BJT). Schematic energy band diagrams of a heterojunction with a wide band-gap N-type emitter and a narrow band-gap p-type base before and after formation are shown in Fig. 2.1a and 2.1b, respectively. The difference in the band gaps between the emitter and the base generates discontinuities in the conduction band and valence band at the interface. According to the electron-affinity model proposed by Anderson [21], the conduction band discontinuity (ΔE_c) is given by

$$\Delta E_c = \chi_p - \chi_N \qquad (2.1)$$

where χ_p and χ_N are the electron affinities of the p type narrow band gap semiconductor and N type wide gap semiconductor, respectively. Thus the valence band discontinuity (ΔE_v) is given by

$$\Delta E_v = \Delta E_g - \Delta E_c \qquad (2.2)$$

where ΔE_g is the band gap difference between wide bad gap and narrow band gap materials.

As shown in Fig. 2.1, an additional valence band barrier (ΔE_v) is created due to the wider band gap material used for the emitter in a HBT. This additional

barrier effectively prevents the holes from the base being injected into the emitter. As a result, a very high emitter injection efficiency (practically unity) is produced which is impossible to achieve in a BJT. This allows the doping of the base to be significantly increased, and the doping of the emitter to be reduced. Thus lower base resistance, smaller base-emitter junction capacitance, and shorter emitter charge storage time are achieved resulting in the superior performance of HBTs in the high speed communication electronic systems.
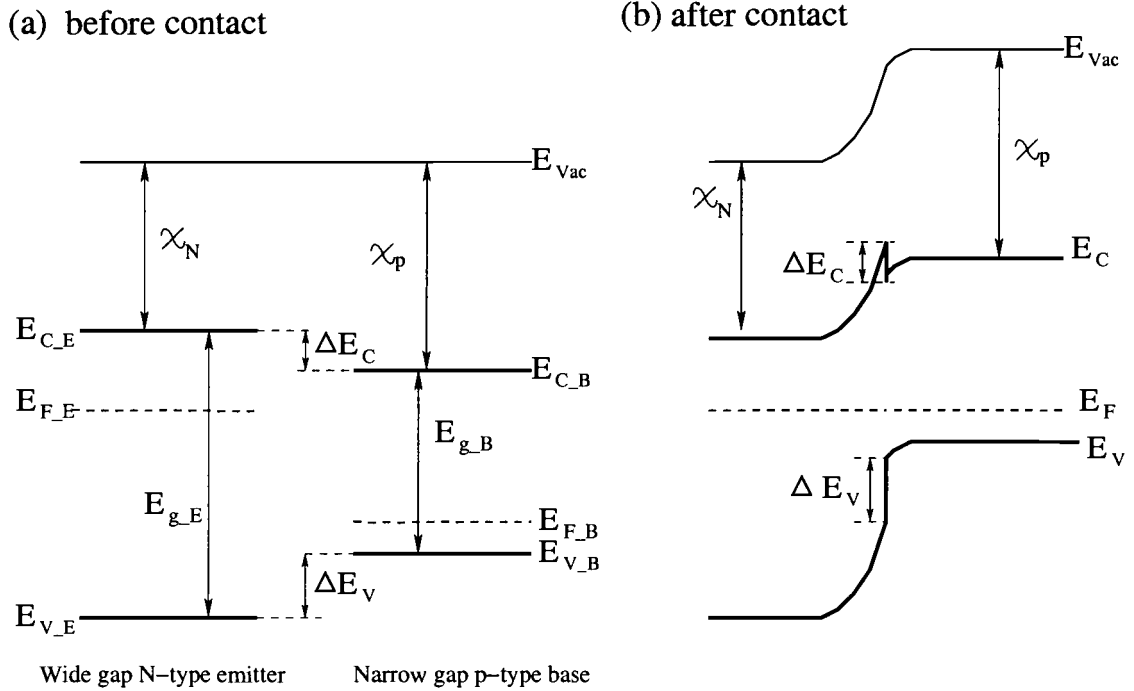
FIGURE 2.1. Energy band diagrams of a heterojunction with a wide bandgap N-type emitter and a narrow bandgap p-type base. (a) before and (b) after formation.

On the other hand, the conduction band discontinuity (ΔE_c) at the interface can cause some undesired problems. This conduction band discontinuity introduces a notch in the conduction band at heterojunction which hinders the injection of electrons from the emitter into the base (thermionic emission). Thus, in a well-engineered device, this conduction band spike would be removed or be reduced to improve the electron injection. This can be done in two ways. One is to employ a compositionally graded heterojunction. This grading of the heterojunction can smooth out the notch in the conduction band, and thus offers near-ideal current-voltage output characteristics, and superior performance. However, it increases the difficulties and complexities of fabrication of the HBT devices. Fig 2.2 shows the band diagrams of SHBTs with abrupt and graded base-emitter heterojunctions.

(a) Abrupt N-p-n SHBT   (b) Graded N-p-n SHBT
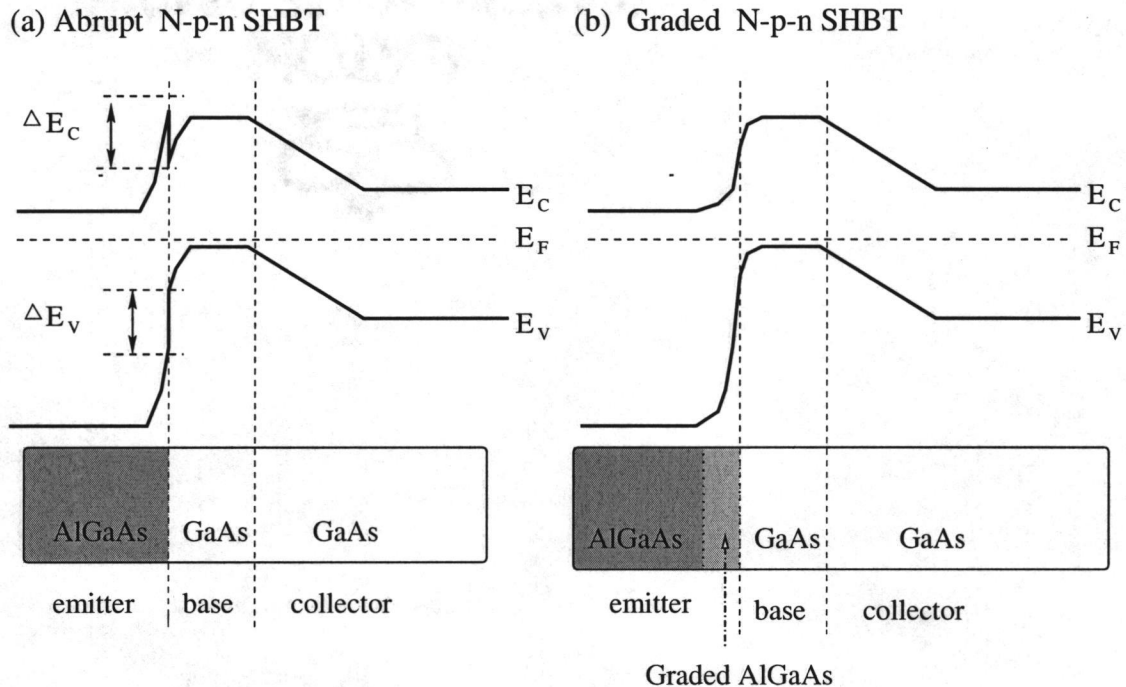
FIGURE 2.2. Energy band diagrams of (a) abrupt SHBT and (b) graded SHBT

Material system	ΔE_g (eV)	ΔE_v (eV)	ΔE_c (eV)	$\Delta E_v/\Delta E_c$
$Al_{0.3}Ga_{0.7}As/GaAs$	0.37	0.13	0.24	0.54
$In_{0.5}Ga_{0.5}P/GaAs$	0.48	0.29	0.19	1.53
$InP/In_{0.53}Ga_{0.47}As$	0.59	0.34	0.25	1.36

TABLE 2.1. The values of band discontinuity in some of the common HBT systems.

The other way is to carefully choose the material systems employed in HBTs. According to equation 2.2, the difference of the band gap (ΔE_g) of the two materials can contribute to the discontinuities in the conduction band (ΔE_c) and in the valence band (ΔE_v). In order to get better performance, one would like to make most of ΔE_g be accommodated in the valance band continuity (ΔE_v). How much of the band gap difference (ΔE_g) is divided into the discontinuities in the valence band and conduction band depends upon the material system used. The values of band discontinuity in some of the common HBT systems are listed in Table 2.1 [22–24]. For example, the value of ΔE_c, and ΔE_v of $Al_{0.3}Ga_{0.7}As/GaAs$ HBT are about 0.24 eV and 0.13 eV, respectively, while those of $In_{0.5}Ga_{0.5}P/GaAs$ HBT are about 0.19 eV and 0.29 eV, respectively. Thus, as compared to $Al_{0.3}Ga_{0.7}As/GaAs$ material system, $In_{0.5}Ga_{0.5}P/GaAs$ material system provides a higher ΔE_v and a lower ΔE_c and hence the InGaP/GaAs HBTs are expected to achieve a superior performance over AlGaAs/GaAs HBTs.

2.3. HBT performance

Heterojunction bipolar transistors, by virtue of their structure, have a number of advantages for high speed applications over other transistors. In comparison with Si bipolar transistors, HBTs have higher cutoff frequency f_T, lower base resistance, lower base-emitter capacitance, higher Early voltage, and better insulating substrates. In comparison with compound field-effect transistors (FETs), HBTs have higher transconductance, higher current and power density, better threshold voltage matching, lower $1/f$ noise and reduced trap-induced effects [25]. Due to this superior performance, tremendous efforts are put into the research and fabrication of HBTs. Since the early '80s, most efforts were focused on AlGaAs/GaAs material system. Intensive study on AlGaAs/GaAs make this material system the first choice for commercial HBTs, and currently the most extensively used III-V heterojunction structure in the high speed, high performance applications. AlGaAs/GaAs HBTs with cutoff frequencies f_T and maximum frequencies of oscillation f_{max} of 100-200 GHz have been reported [26].

GaInP/GaAs heterojunction bipolar transistors (HBTs) grown by MOCVD were first demonstrated by Razeghi et $al.$ [27]. This technology is currently accepted as a superb alternative to AlGaAs/GaAs HBTs due to the absence of DX center, the better etching selectivity, and excellent (10 times better than AlGaAs/GaAs) reliability characteristics [28] [29]. Monolithic broad band GaInP/GaAs HBT amplifiers have been demonstrated with a bandwidth (BW) of 19 GHz as well as their high gain performance [30] [31]. Excellent microwave performance of $f_T = 140$ GHz and $f_{max} = 230$ GHz has been achieved by using GaInP/GaAs HBTs [32].

InP/InGaAs HBTs provide higher electron mobility, lower surface recombination, and higher drift velocity at the high field. They can operate at even higher frequency, such as $f_T = 200$ GHz, and $f_{max} = 236$ GHz [33]. The smaller band

gap of InGaAs (0.75 eV) which is compatible with low loss/dispersion optic fibers makes InGaAs-based HBTs very attractive for high speed fiber-optic communication applications.

Other HBTs also have received great attention due to their special properties. Wide band gap AlGaN/GaN HBTs which provide very high breakdown voltage are very attractive in high power applications. Si/GeSi HBTs which offer the compatibility with well-developed silicon MOSFET processing technologies have also received great attention for the lower cost and reduced complexity of the processing.

2.4. HBT operation

A schematic diagram of an Npn HBT structure is shown in Fig 2.3(a). HBTs can be operated in four modes depending upon the different base-emitter bias (V_{BE}) and base-collector bias (V_{BC}): (1) saturation ($V_{BE} > 0, V_{BC} > 0$); (2) forward active ($V_{BE} > 0, V_{BC} < 0$); (3) inverse active ($V_{BE} < 0, V_{BC} > 0$); and (4) cutoff ($V_{BE} < 0, V_{BC} < 0$).

In most practical applications, HBTs are operated in the forward active mode. The current components of an Npn BJT in the active mode are shown in Fig 2.3(b). An electron current (I_{En}) is injected into the base from the emitter through forward biased base-emitter heterojunction. While this electron current diffuses through a thin base region, a small portion of this electron current undergoes recombination in the bulk and along the periphery of the emitter-base (BE) space-charge region (SCR) and in the bulk and at the surface of the quasi-neutral base region [34]. The rest of it, accelerated by the strong electric field of the reversed biased BC junction, is then swept into the collector region. The base current is contributed by four components: (1) I_{Bp} - the hole current injected into the emitter

(a)

(b)
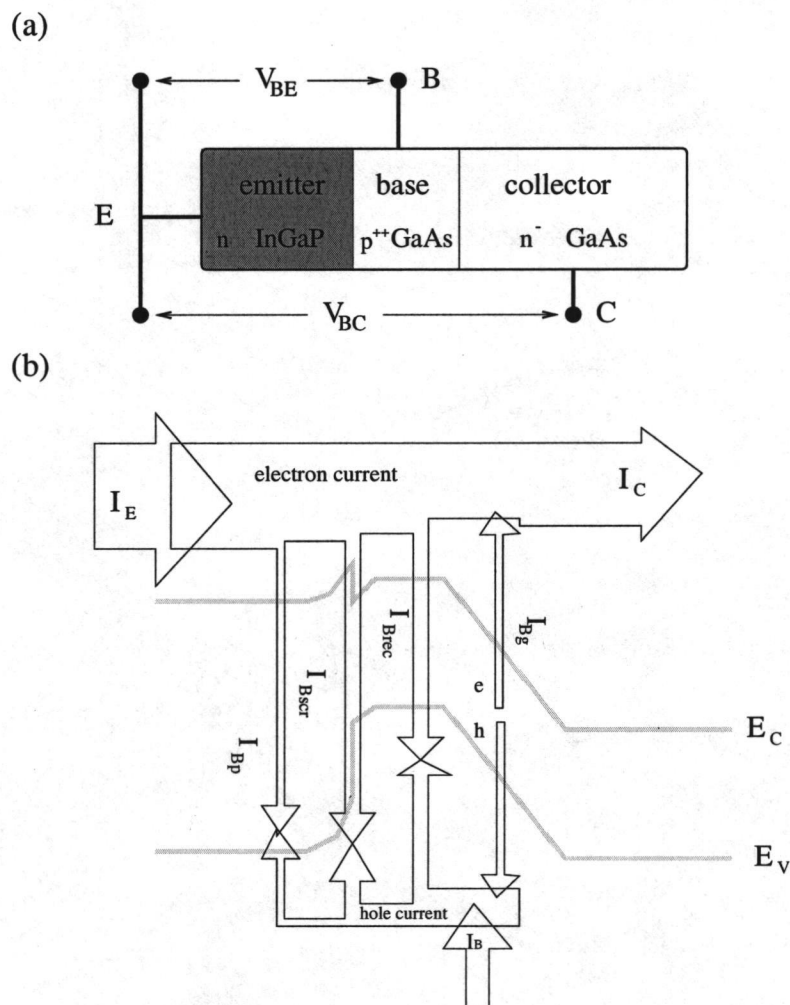
FIGURE 2.3. (a) Schematic diagram of an Npn HBT (b) Current components of an Npn HBT in the active mode

from the base. Since the injection efficiency of an HBT is very close to unity, I_{Bp} may be neglected. (2) I_{Bscr} - the holes and electrons recombined in the bulk and along the periphery of the base-emitter (BE) space-charge region (SCR). (3) I_{Brec} - the holes and electrons recombined in the bulk and at the surface of the quasi-neutral base region. (4) I_{Bg} - the electrons and holes generated by the reverse biased base-collector junction. Thus the collector current is the sum of the unrecombined

injected electron current and the generated current in BC junction. The currents in a HBT can be written as

$$I_E = I_{En} + I_{Bp} \tag{2.3}$$

$$I_B = I_{Bp} + I_{Bscr} + I_{Brec} - I_{Bg} \tag{2.4}$$

$$I_C = I_{En} - I_{Bscr} - I_{Brec} + I_{Bg} \tag{2.5}$$

The typical HBT common-emmiter I_C - V_{CE} curves measured at base current of 0 μA, and 10 μA are shown in Fig. 2.4. In the case of $I_B = 10$ μA, when the V_{CE} sweeps from 0 volt, BE and BC junction voltages adjust themselves to provide enough electrons to match the constant hole current injected from the base. The junction voltages satisfy eq. 2.6, according to Kirchoff's voltage law (KVL).

$$V_{CE} = V_{BE} - V_{BC} \tag{2.6}$$

While $V_{CE} = 0$ volt, both BE and BC junctions are forward biased at the same potential ($V_{BC} = V_{BE}$). Due to the conduction band discontinuity in BE heterojunction, the electrons injected from the emitter face an extra barrier in the BE heterojunction. In order to compensate the hole current injected from the base, the BC junction provides the electron current needed and thus the base hole current flows out of the collector. The collector current consequently becomes negative at low V_{CE} and equal to the base current (10 μA in this case). This regime is shown in Fig 2.4 (a).

As V_{CE} is increased, the BE junction bias increases, and hence, more and more electrons are injected into the base. The BE junction starts competing with BC junction for the constant base current. Thus, less hole current is recombined by the electrons injected from the BC homojunction, and as a result, the V_{BC} decreases.
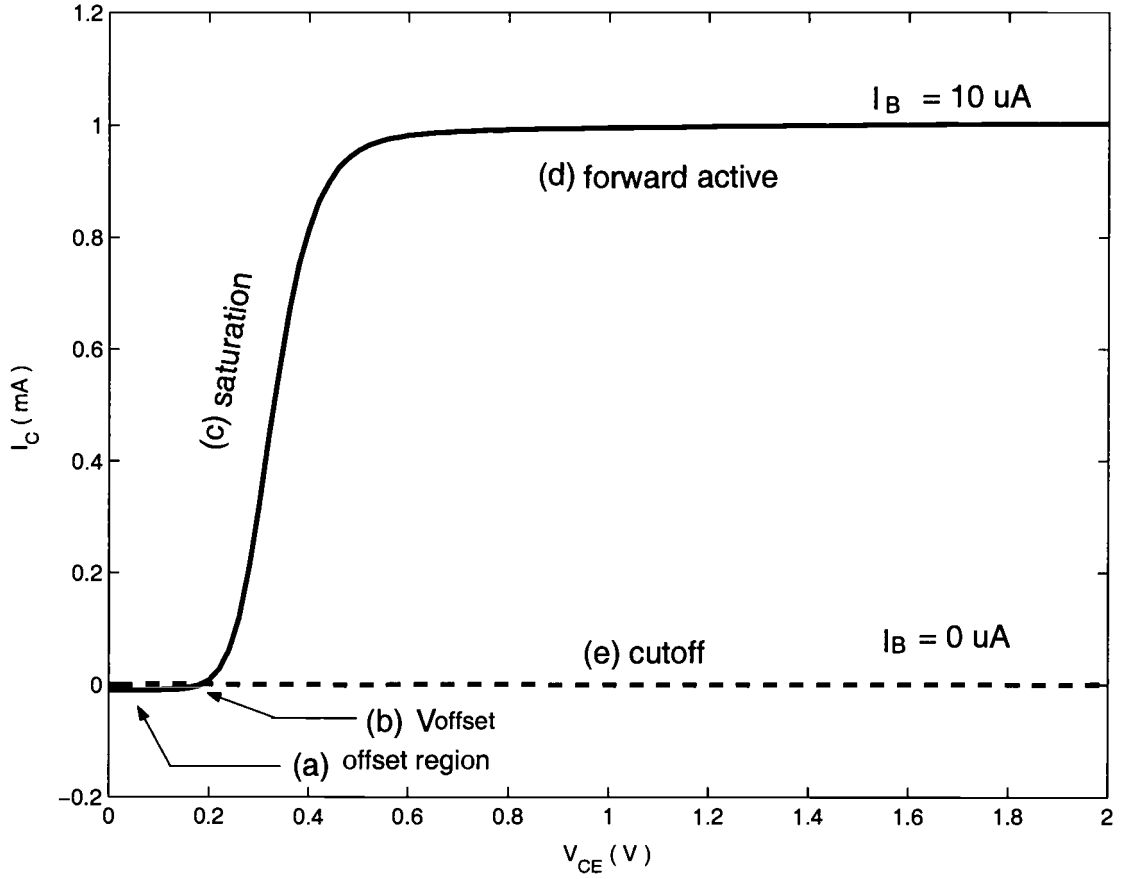
FIGURE 2.4. A typical HBT Common-emitter current-voltage characteristics

At some point, the electron current injected from BE heterojunction will equal that injected from BC homojunction. Thus the collector current becomes zero. At this point, V_{CE} is called the offset voltage ($V_{CEoffset}$) which is shown in Fig 2.4 point (b). As V_{CE} is increased, the forward bias of the BE junction increases and bias of the BC junction decreases. This corresponds to the saturation mode of operation, and is shown in Fig 2.4 region (c).

As V_{CE} is increased further, at some point, the electron current injected from BE junction provides all the electrons for the hole current from the base. The BC

junction reduces to zero and the device enter the forward active mode. After this point, the value of V_{BE} remains constant as V_{CE} is further increased. The further increase of V_{CE} then contributes to the more negative BC junction bias (V_{BC}). As a result, the collector current stays constant in this regime called forward active which is shown in Fig 2.4 region (d).

However, in practical application, I_C usually shows a gradual increase along with increasing V_{CE} in active region. Due to the heavy doping concentration of the base in HBTs, we believe that this increase of I_c in the active region in HBTs is possibly caused by the avalanche multiplication of electrons crossing the high electric field region in the reverse biased BC junction rather than by base modulation effects. This issue will be further discussed in the later HBT modeling section.

2.5. HBT electrical characterization and measurement setup

InGaP/GaAs HBTs employed in this study were grown on GaAs substrates either by MBE or by MOVPE techniques at Infineon Technologies Laboratory. A schematic cross section and epilayer sequence of this HBT devices structure are shown in Fig 2.5. The HBT epitaxial structure consists of a 700 nm n-type heavily doped GaAs subcollector, a 20 nm n-type InGaP subcolletor etch-stop, a 50 nm n-type heavily doped ($5.0 \times 10^{18} cm^{-3}$) and 700 nm lightly doped GaAs collector, a p-ype heavily doped GaAs base, a 40 nm n-type doped ($4.0 \times 10^{17} cm^{-3}$) InGaP emitter, a 150 nm n-type doped ($4.0 \times 10^{17} cm^{-3}$), and a 50 nm n-type heavily doped ($6.5 \times 10^{17} cm^{-3}$) GaAs emitter cap, a 50 nm graded layer from GaAs to $In_{0.5}Ga_{0.5}As$, and 50 nm heavily doped $In_{0.5}Ga_{0.5}As$ contacting layer. The devices tested in this study have three emitter size, 3.2×10, 3.2×14, and 3.2×30 μm^2, respectively.
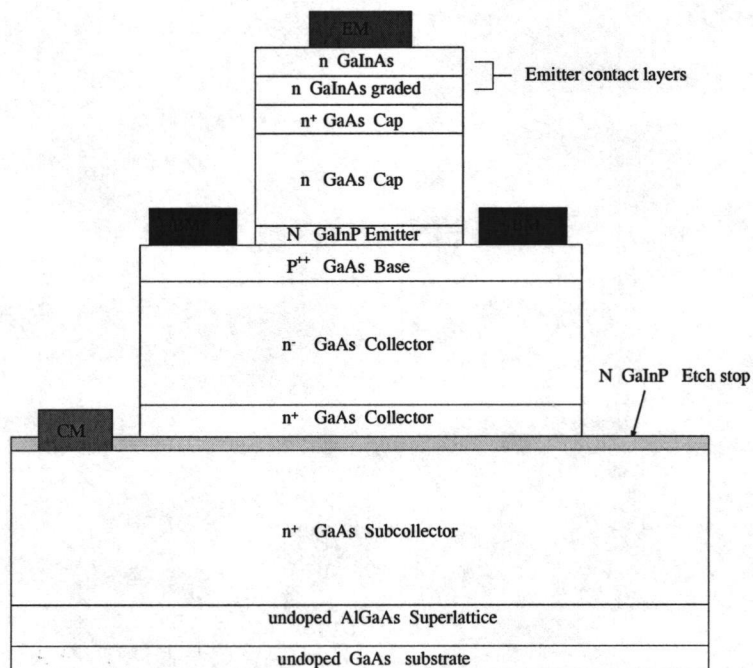
FIGURE 2.5. InGaP/GaAs SHBT structure

Current-voltage (I-V) measurements were performed by employing an HP-4145B parameter analyzer which is connected to a PC through an HPIB interface. The measurement setup is shown schematically in Fig 2.6. There are seven electrical characterizations performed in this study: (1) Common emitter I-V measurement (I_C - V_{CE}); (2) forward Gummel measurement; (3) inverse Gummel measurement; (4) common emitter current gain (h_{FE}) measurement; (5) base-emitter diode characteristics measurement; (6) base-collector diode characteristics measurement; (7) common-base breakdown voltage (BV_{CBO}) measurement.

The measurement configuration for measuring the I_C - V_{CE} characteristics is shown in Fig 2.7 (a). The collector current is measured at different values of the base current, such as 0, 10, 20, 30, 40, 50, 60, 70 and 80 μA, by sweeping the collector-emitter bias (V_{CE}) from 0 to 2 volts.
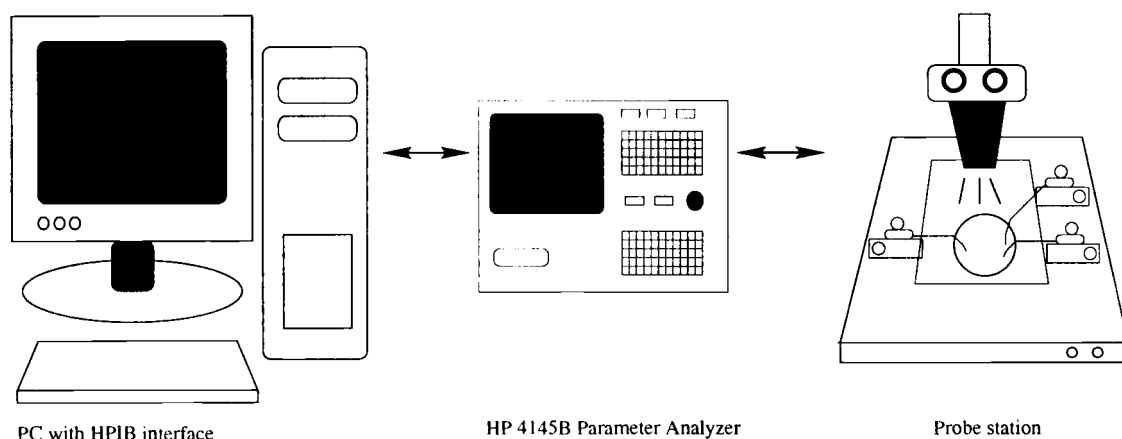
FIGURE 2.6. I-V measurement setup, consisting of a PC with an HPIB interface, HP 4145B parameter analyzer and a microprobe station

The measurement configuration for forward Gummel measurement is shown in Fig 2.7 (b). The base current and collector current are measured by sweeping the base-emitter bias from 0 to 1.5 volts, with the base and collector terminal shorted. Similarly, the measurement configuration for inverse Gummel measurement is shown in Fig 2.7 (c). The base current and emitter current are measured by sweeping the base-collector bias from 0 to 1.5 volts, with the base and emitter terminal shorted. The measurement configuration for common emitter current gain measurement is similar to the one shown in Fig 2.7 (a). The collector current (I_C) is measured by sweeping base current (I_B) with a 2 volt V_{CE} bias. Common-emitter current gain (h_{FE}) can be obtained by dividing I_C by corresponding I_B. Measurement configurations for base-emitter diode characteristics as well as base-collector diode characteristics are shown in Fig 2.8 (a), and (b). The diode currents are measured by sweeping the desired junction bias with the third terminal floating. The configuration of breakdown voltage measurement is shown in Fig 2.8 (c). I_C is measured
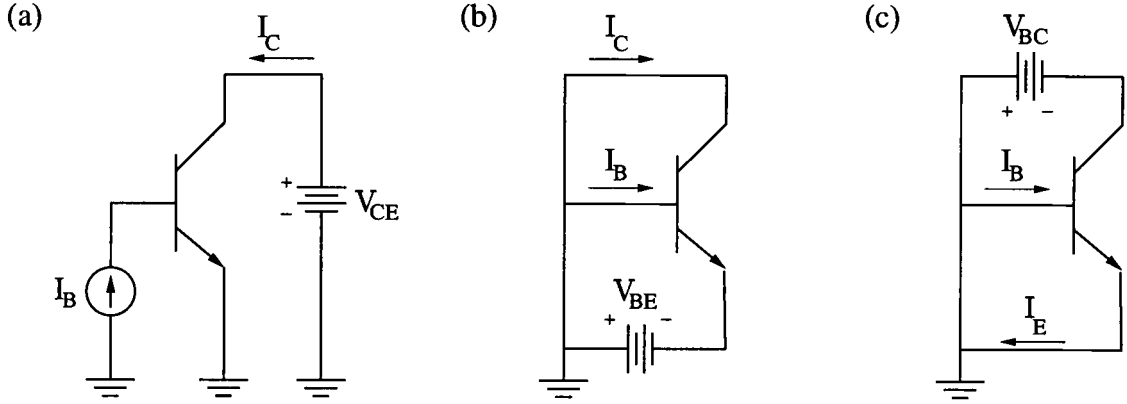
FIGURE 2.7. Circuit configuration used in I-V measurements. (a) common-emitter I-V characteristics ($I_C - V_{CE}$), (b) Gummel plots, and (c) inverse Gummel plots

by sweeping base-collector bias with emitter open, and then the value of BV_{CBO} can be determined by $I_C - V_{BC}$ plot.

2.6. HBT modeling

Understanding of the device behavior without radiation is the key to studying the effects of radiation in semiconductor devices. If the normal operation of a device is understood, the alterations in the device performance resulting from radiation can easily be revealed and can be easily incorporated into the device model for unradiated devices. For this reason, an expanded compact model is proposed. In the compact model, a heterojunction bipolar transistor (HBT), similar to a bipolar junction transistor, is viewed as two pn junctions back to back with a thin base layer [35]. However, device characteristics and operation of heterojunction bipolar transistors differ from those of conventional silicon bipolar junction transistors in several aspects. The determination of HBT device parameters, therefore, needs additional

(a)   (b)   (c)
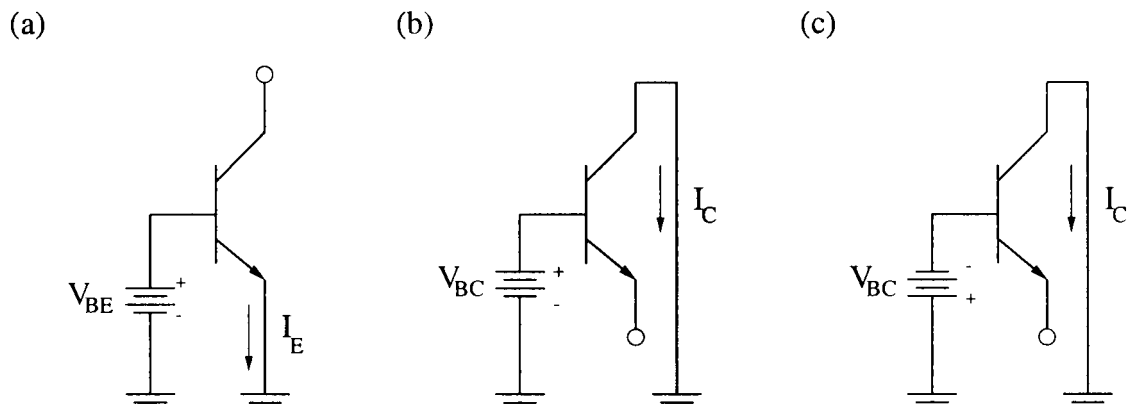
FIGURE 2.8. Circuit configuration used in (a) base-emitter diode characteristics, (b) base-collector diode characteristics, and (c) common-base breakdown voltage (BV_{CBO}) measurement.

consideration, and the models used for analysis deviate from those conventionally used for BJTs.

The compact model employed here is developed from Ebers-Moll (EM) models. The dc operation of conventional silicon BJT can be accurately simulated by EM models. However, due to the strong recombination in base-emitter (B-E) space-charge region (SCR), the value of base current ideality factor varies from 1 to 2 over the bias range. HBTs do not exhibit a region of operation where the current gain is constant. Therefore, Ebers-Moll models cannot correctly simulate the dc I-V characteristics of HBTs. As a result, in order to fit the operation characteristics of HBTs, several modifications are made on the original EM models to include the following effects: (1) carrier recombination in base-emitter junction region and collector-base junction region; (2) avalanche multiplication of carriers in the collector-base region; (3) leakage current at the periphery of the emitter-base junction and collector-base junction.

In this section, a compact dc model and parameter extraction scheme for InGaP/GaAs HBTs are presented. The parameters are extracted directly from various experimental I-V measurements. The parameters extracted include saturation currents, ideality factors, and series resistance. By employing these parameters, the simulated results are compared with the experimental measured data of InGaP/GaAs HBTs.

2.6.1. Description of the model

The modified extended Ebers-Moll large signal representation used is shown in Fig. 2.9. The base current in this model is represented by two sets of parallel diodes. One set corresponds to the base-emitter heterojunction, and the other set corresponds to the base-collector homojunction.

One diode in each set (diodes a, b) corresponds to the base current recombined in the SCR of junctions. These current components are represented by $I_{B,be1}$ and $I_{B,bc1}$ for the BE and BC junctions, respectively. Their ideality factors, n and n', are generally close to 2. The other diode in each set (diode c, d) represents the base current recombined in quasi-neutral base region. This current component is represented by $I_{B,be2}$ and $I_{B,bc2}$ for the BE and BC junctions, respectively. Their ideality factors , m and m', are generally close to 1. At the same time, the leakage currents at the periphery of the emitter-base junction and collector-base junction are taken into account by introducing $I_{B,belk}$ and $I_{B,bclk}$. Thus, the base current can be written as

$$I_B = I_{B,p} + I_{B,be1} + I_{B,be2} + I_{B,bc1} + I_{B,bc2} + I_{B,belk} + I_{B,bclk} \qquad (2.7)$$

and

$$I_{B,be1} = I_{B,be10} \; exp[\frac{q(V_{BE} + I_E R_E - I_B R_B)}{nkT}] \qquad (2.8)$$
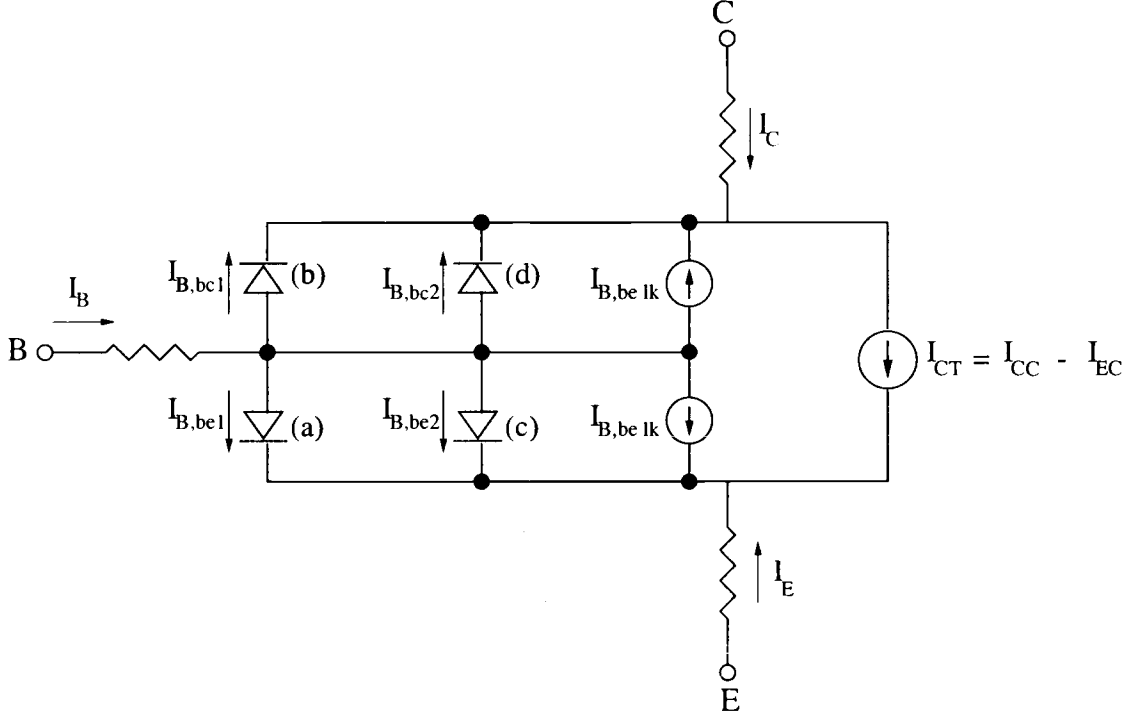
FIGURE 2.9. A modified extended Ebers-Moll large signal model of HBTs

$$I_{B,be2} = I_{B,be20} \; exp[q(V_{BE} + I_E R_E - I_B R_B)mkT] \qquad (2.9)$$

$$I_{B,bc1} = I_{B,bc10} \; exp[\frac{q(V_{BC} + I_C R_C - I_B R_B)}{n'kT}] \qquad (2.10)$$

$$I_{B,bc2} = I_{B,bc20} \; exp[\frac{q(V_{BC} + I_C R_C - I_B R_B)}{m'kT}] \qquad (2.11)$$

where R_E, R_C and R_B are the combined bulk and contact resistance associated with emitter, collector and base region, respectively. The prefactors $I_{B,be10}$, $I_{B,be20}$, and the ideality factors n, m are constants associated with the recombination in the SCR and neutral base region of BE junction. Similarly, $I_{B,bc10}$, $I_{B,bc20}$, and the ideality factors n', m' are constants associated with the recombination in the

SCR and neutral base region of BC junction. The leakage currents are assumed to be constant over the junction bias range for simplicity. $I_{B,p}$ is the hole back injection current from the base to the emitter. Due to the very high injection efficiency of HBT, $I_{B,p}$ may be neglected in the first approximation.

The current source (I_{CT}) between the emitter and the collector in Fig 2.9 are defined by the expression

$$I_{CT} = I_{CC} - I_{EC} \tag{2.12}$$

where the reference currents I_{CC} and I_{EC} can be expressed as

$$I_{EC} = I_{E0} \ exp[\frac{q(V_{BC} + I_C R_C - I_B R_B)}{m'kT}] \tag{2.13}$$

$$I_{CC} = I_{C0} \ exp[\frac{q(V_{BE} + I_E R_E - I_B R_B)}{mkT}] \tag{2.14}$$

Thus, collector and emitter terminal currents of the HBT are given by

$$I_C = I_{CT} - (\ I_{B,be1} + I_{B,be2} + I_{B,belk}\ ) + I_{Clk} \tag{2.15}$$

$$I_E = -I_{CT} - (\ I_{B,bc1} + I_{B,bc2} + I_{B,bclk}\ ) + I_{Elk} \tag{2.16}$$

where I_{Clk} and I_{Elk} represent the leakage currents which contribute to the terminal currents of the collector and the emitter, respectively.

2.6.2. Parameters extraction

As shown in Fig 2.9, HBT is modeled as two individual junctions, BE and BC junctions, back to back. In order to reduce the level of complexity of the analysis, forward Gummel and inverse Gummel measurements are employed. These measurements provide the ability to analyze the BE and BC junctions seperately.

First, we consider the BE junction (forward Gummel measurement). In forward Gummel measurement, the base-collector junction is shorted ($V_{BC} = 0$). The collector current and base current are then measured by varying the bias across the base and the emitter (V_{BE}). The current components of an Npn SHBT in the forward Gummel measurement are shown in Fig 2.10
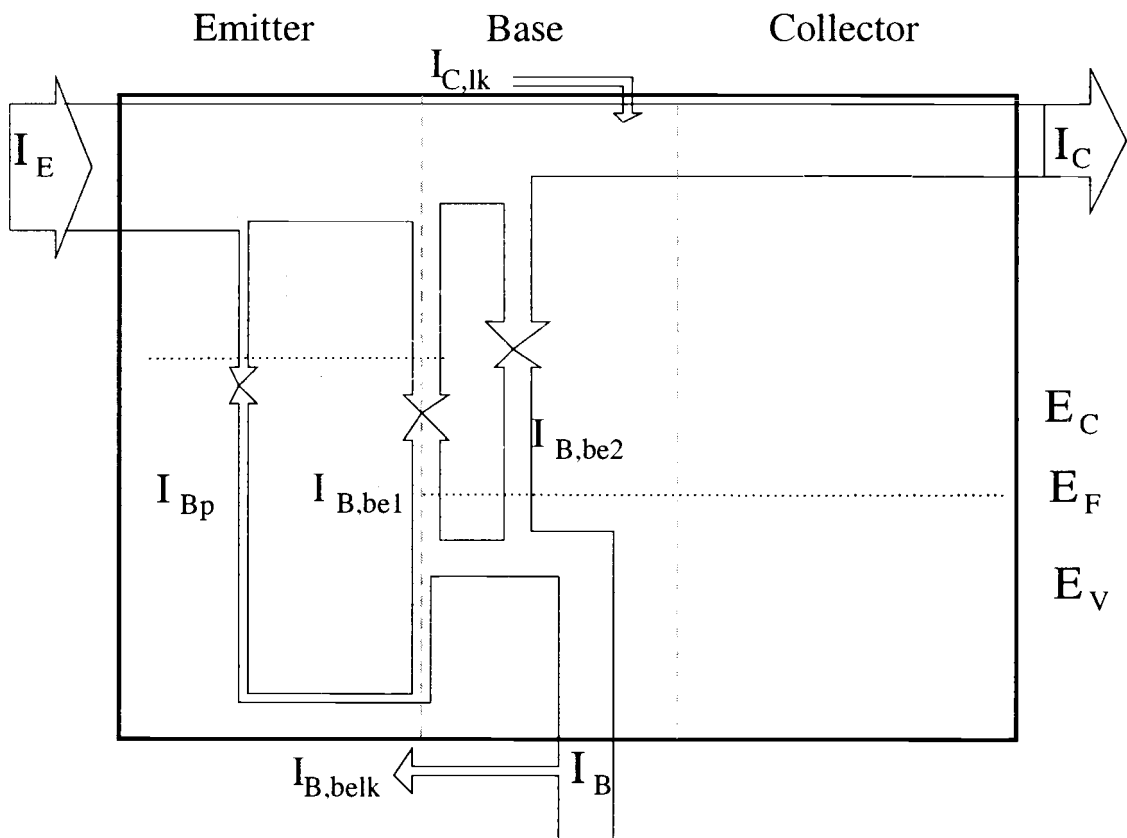
FIGURE 2.10. Current components of an Npn SHBT in the forward Gummel measurement

Due to a relatively large discontinuity of the valence band in the BE heterojunction, the hole back injection current $(I_{B,p})$ from the base to the emitter is efficiently suppressed. In the first approximation, this hole current is neglected throughout this Gummel plot analysis. Thus, the base current is dominated by the recombination of the holes. The holes recombine with electrons injected from the emitter (1) in the bulk and along the periphery of the BE junction space charge region (SCR) and (2) in the bulk and at the surface of the neutral base region. The recombination of the electron-hole pairs through these two processes gives rise to the majority of the base current. At the same time, the leakage current $(I_{B,belk})$ on the BE junction surface is also taken into account. Therefore, the base current in the Gummel plot (I_B) can be expressed as

$$I_B = I_{B,be1} + I_{B,be2} + I_{B,belk} \qquad (2.17)$$

where $I_{B,be1}$ and $I_{B,be2}$ present the two components of the recombination current mentioned above. Their dependencies on V_{BE} can be expressed as

$$I_{B,be1} = I_{B,be10} \ exp[\frac{q(V_{BE} + I_E R_E - I_B R_B)}{nkT}] \qquad (2.18)$$

$$I_{B,be2} = I_{B,be20} \ exp[\frac{q(V_{BE} + I_E R_E - I_B R_B)}{mkT}] \qquad (2.19)$$

where R_E and R_B are the emitter and the collector series resistance, respectively.

Since the base is very thin in HBTs, the injected electrons that do not undergo recombination will reach the base-collector junction, and are collected by the collector as collector current. This collector current in Gummel plot (I_C) can be expressed as

$$I_C = I_{C0} \ exp[\frac{q(V_{BE} + I_E R_E - I_B R_B)}{mkT}] + I_{C,lk} \qquad (2.20)$$

Since the BE junction is an abrupt heterojunction, values of m slightly higher than unity are usually observed, due to the conduction band discontinuity [36]. From the Gummel plot, the parameters can be easily extracted by following the equations given above.
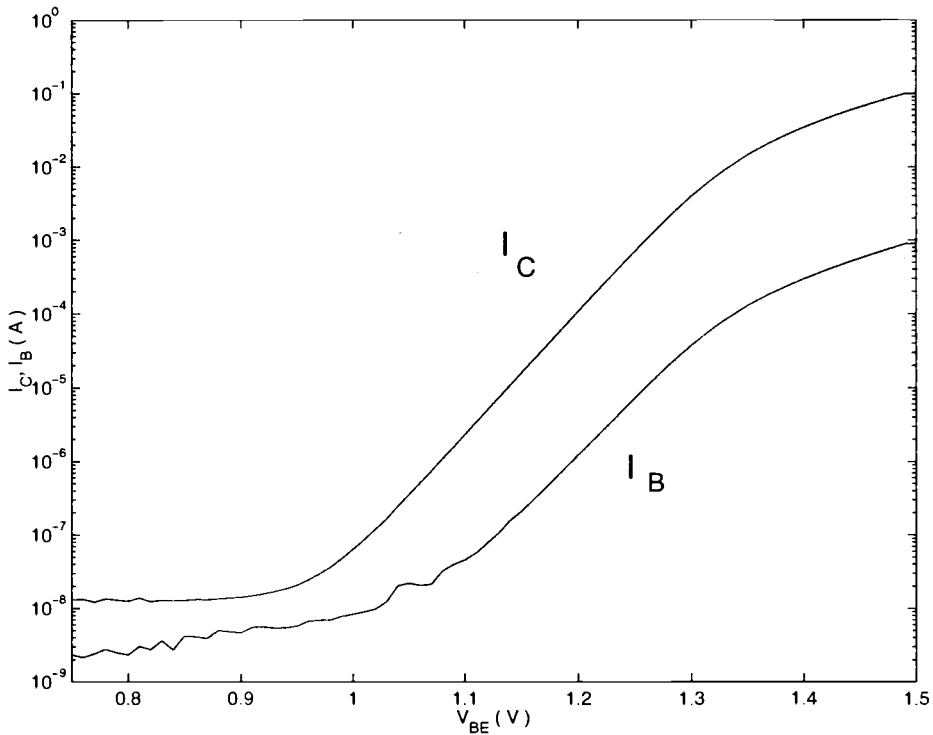
FIGURE 2.11. A typical measured Gummel plot of HBT

A typical measured Gummel plot is shown in Fig 2.11. In the very low V_{BE}, the collector leakage current is the predominant component of the collector current [37, 38]. Hence, the value of $I_{C,lk}$ is approximately equal to the value of I_C in the very low V_{BE} region. As V_{BE} is increased a bit (still very low), the collector and base currents are still sufficiently small, so that the voltage drop across the R_E and R_B may be neglected. According the equation 2.20, we can extract the ideality factor

m from the slope of the $\log(I_C\text{-}I_{C,lk})$ - V_{BE} curve. The prefactor I_{C0} then can be determined from the extrapolation of the linear region of $\log(I_C\text{-}I_{C,lk})$ - V_{BE} plot to $V_{BE} = 0$ axis.

Similarly, in the very low V_{BE} region, the leakage current around the BE junction gives rise to the base current. The value of $I_{B,belk}$ can be estimated from the value of I_B in this region. As V_{BE} is increased a bit, the space-charge recombination component ($I_{B,be1}$) dominates the base current. At the same time, the collector and base currents are sufficiently small, so that the voltage drop across the R_E and R_B may be neglected. Thus, the equation 2.17 may be simplified as

$$I_B - I_{B,belk} = I_{B,be1} = I_{B,be10} \ exp[\frac{q(V_{BE})}{nkT}] \tag{2.21}$$

Therefore, the ideality factor n and prefactor $I_{B,be10}$ can be determined from the slope and the intercept of the $\log(I_B\text{-}I_{B,belk})$ - V_{BE} curve in the region of low V_{BE} in the measured Gummel plot.

Using the already extracted parameters, $I_{B,belk}$, m, n and $I_{B,be10}$, the value of $I_{B,be20}$ is easily determined by fitting the $\log(I_B)$ - V_{BE} curve in the intermediate V_{BE} region where series resistance effects are still small.

So far, there are 6 parameters, I_{C0}, $I_{B,belk}$, m, n, $I_{B,be10}$ and $I_{B,be20}$, introduced by fitting the forward Gummel plot in the low and intermediate V_{BE} region. In the large V_{BE} region, both the collector current and the base current are limited by the series resistance effects. Since value of I_E is typically two order magnitude higher than that of I_B, the voltage drop across R_B is significantly small compared to that across R_E. Thus, the voltage drop across R_B may be neglected, and the value of R_E can be determined by fitting high V_{BE} region in the forward Gummel plot.

After the parameter extraction has been done from the BE junction , we then turn our focus on the BC junction (inverse Gummel plot). In inverse Gummel measurement, the base-emitter junction is shorted (V_{BE}=0). The emitter current

and base current are then measured by varying the forward bias across the base and the collector (V_{BC}). In SHBTs, due to the doping concentration in the base is several orders magnitude higher than that in the collector, the forward junction current is dominated by the injected holes from the base to collector, and the component that comes from the electrons injected from the collector is relatively small. Moreover, in the HBT mesa structure shown in Fig 2.5, the area of base contacts is approximately equal to the base-collector junction. Therefore, most injected electrons are collected by base contacts, and only a small fraction of injected electrons are collected by the emitter as the emitter current. Thus, it is safe to assume $I_B \approx I_C \gg I_E$ and the emitter current in the inverse Gummel plot may be expressed as

$$I_E = I_{E0} \; exp[\frac{q(V_{BC} + I_C R_C - I_B R_B)}{m'kT}] + I_{E,lk} \tag{2.22}$$

where R_C is the collector series resistance. The ideality factor m and prefactor I_{E0} are constant along with V_{BC}. Since, in SHBT, the BC junction is a homojunction, the ideality factor, m', is expected to be very close to unity.

Similar to the forward Gummel plot, in the inverse Gummel plot, the base current ($I_{B,IG}$) can be divided into three components: (1)$I_{B,bc1}$ - recombination current in the BC junction space charge region (SCR) ; (2)$I_{B,bc2}$ - recombination of injected hole from the base with electrons in the neutral collector region ; and (3)$I_{B,bclk}$ - the base leakage current. The current components in inverse Gummel plot are shown in Fig 2.12.

The base current in the inverse Gummel plot, therefore, can be written as

$$I_B = I_{B,bc1} + I_{B,bc2} + I_{B,bclk} \tag{2.23}$$

where $I_{B,bc1}$ and $I_{B,bc2}$ present the two components of the recombination current mentioned above. Their dependencies on V_{BE} can be expressed as

$$I_{B,bc1} = I_{B,bc10} \; exp[\frac{q(V_{BC} + I_C R_C - I_B R_B)}{n'kT}] \tag{2.24}$$
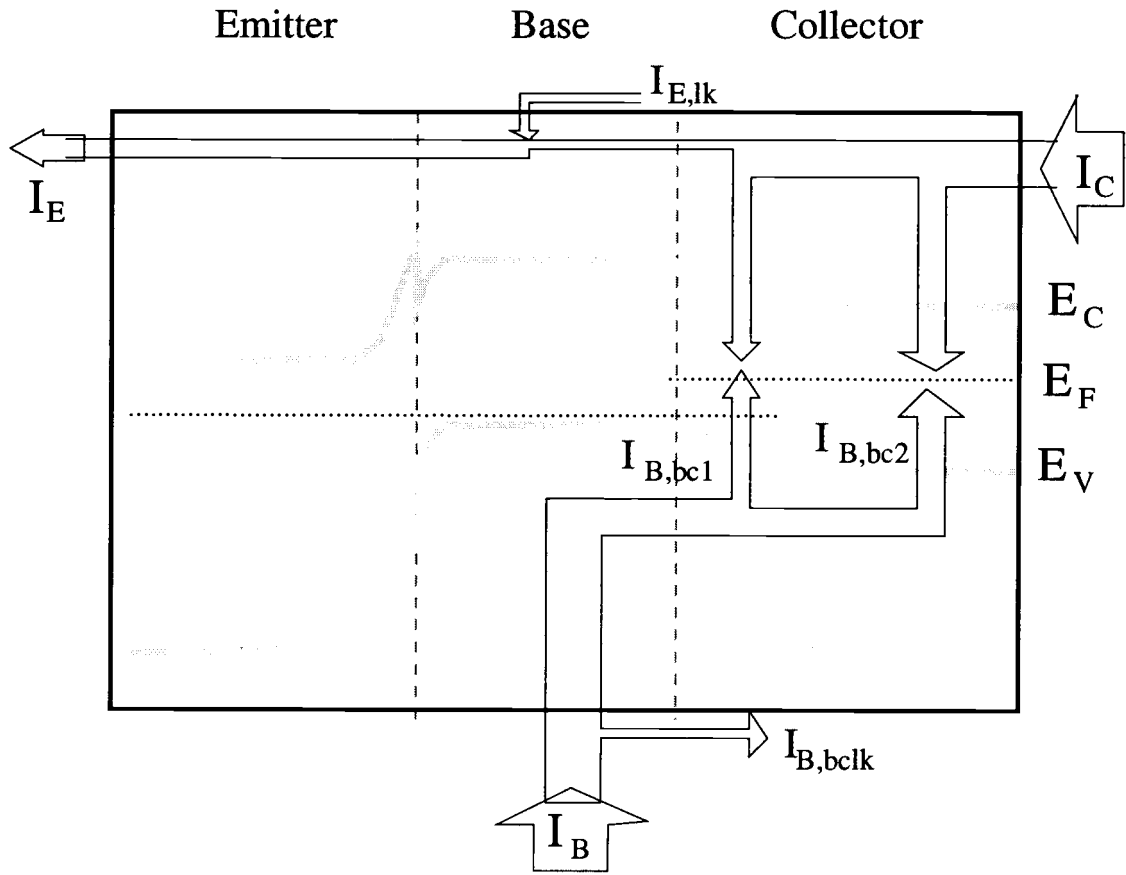
FIGURE 2.12. Current components of an Npn SHBT in the inverse Gummel measurement

$$I_{B,bc2} = I_{B,bc20} \ exp[\frac{q(V_{BC} + I_C R_C - I_B R_B)}{m' kT}]$$ (2.25)

A typical measured inverse Gummel plot is shown in Fig 2.13. A very similar parameter extraction precedure is taken in the inverse Gummel plot. The emitter leakage current ($I_{E,lk}$) is determined by the value of the emitter current in the very low V_{BC}. The ideality factor and the prefactor (m' and I_{E0}) are again determined by the slope and the intercept of the $\log(I_E\text{-}I_{E,lk})$ - V_{BC} curve in the low V_{BC} region.
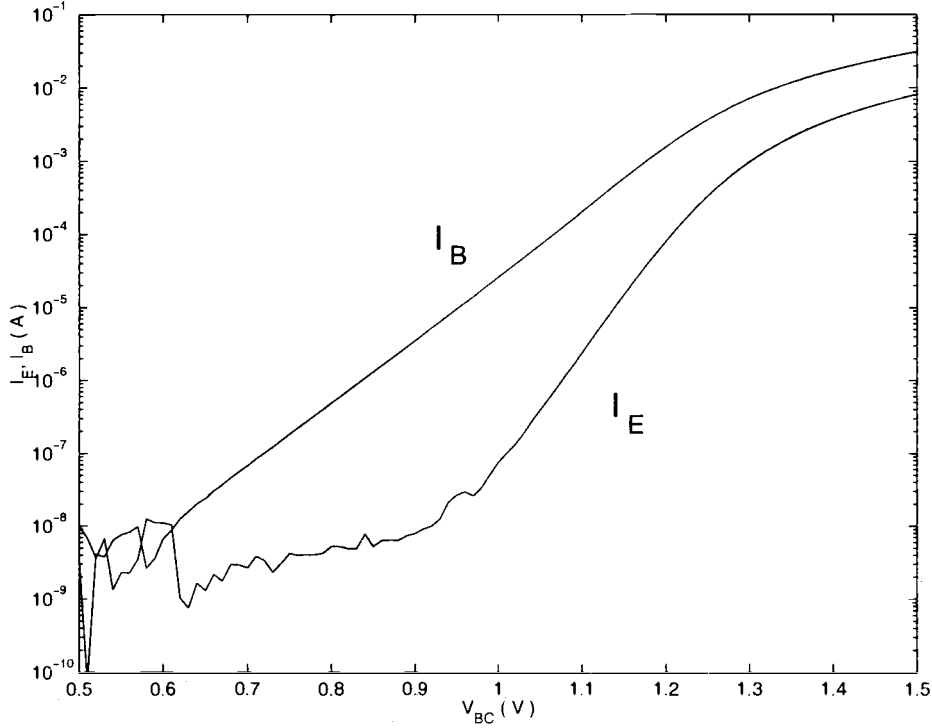
FIGURE 2.13. A typical measured inverse Gummel plot of HBT

Similar to the forward Gummel plot case, in the very low V_{BC} region, the base leakage current gives rise to the base current. The value of $I_{B,bclk}$ can be estimated from the value of base current in the very low V_{BC} region. As V_{BC} is increased a bit, the space-charge recombination component ($I_{B,bc1}$) dominates in the base current. Thus, the ideality factor n' and prefactor $I_{B,bc10}$ can be determined from the slope and intercept of the $\log(I_E\text{-}I_{B,bclk})$ - V_{BC} curve in the region of low V_{BC} where the series resistance effects are not significant.

Using the already extracted parameters, $I_{B,bclk}$, m', n' and $I_{B,bc10}$, the value of $I_{B,bc20}$ is determined by fitting the $\log(I_E)$ - V_{BC} curve in the intermediate V_{BE} region.

Thus, there are 6 parameters, I_{E0}, $I_{B,bclk}$, m', n', $I_{B,bc10}$ and $I_{B,bc20}$, extracted so far by fitting the inverse Gummel plot in the low and intermediate V_{BC} region. Since the value of I_C is very close to that of I_B in inverse Gummel measurement, the value of $R_C + R_B$ may be determined by fitting high V_{BE} region in the inverse Gummel plot.

Finally, the value of $R_E + R_B$ can be estimated by fitting the I-V curve under large forward bias in the base-emitter diode characteristics measurement. Since the value of R_E has been determined in the forward Gummel plot, the value of R_B can then easily estimated. The value of R_C can further be determined from the extracted value of $R_C + R_B$ in the BC diode I-V curves.

2.6.3. Simulations for the I_C-V_{CE} characteristics

In this section, we show how the extracted parameters are employed to model the I_C - V_{CE} characteristics. In the I_C - V_{CE} measurement, I_C is measured as function of the V_{CE} with a constant base current. In order to calculate the collector current, the individual potential drop across the BE and BC junctions (V_{BE} and V_{BC}) for a fixed V_{CE} needs to be calculated.

According to the extended Ebers-Moll large signal model shown in Fig. 2.9, the base current can be written as

$$I_B = I_{B,be1} + I_{B,be2} + I_{B,bc1} + I_{B,bc2} + I_{B,belk} + I_{B,bclk} \qquad (2.26)$$

where $I_{B,be1}$, $I_{B,be2}$, $I_{B,bc1}$ and $I_{B,bc2}$ are given by equations 2.18-2.19 and equations 2.24-2.25. The parameters needed in these equations are known from forward, inverse Gummel plots and diode characteristics analysis. These extracted parameters include prefactors ($I_{B,be10}$, $I_{B,be20}$, $I_{B,bc10}$ and $I_{B,bc20}$), ideality factors (m, n, m' and n') and the base leakage currents ($I_{B,belk}$ and $I_{B,bclk}$).

Thus, there are only two unknowns (V_{BE} and V_{BC}) left in equation 2.26. By employing the relation

$$V_{BE} = V_{CE} + V_{BC} \qquad (2.27)$$

the right hand side of the equation 2.26 can be simplified as a function with only one unknown, V_{BC}, for a fixed I_B and V_{CE}. Thus, for every given V_{CE} the corresponding values of V_{BC} and V_{BE} can be obtained.

Again, according to the extended Ebers-Moll large signal model shown in Fig. 2.9, the collector current can be written as

$$I_C = I_{CT} - (\ I_{B,be1} + I_{B,be2} + I_{B,belk}\ ) + I_{Clk} \qquad (2.28)$$

where

$$I_{CT} = I_{CC} - I_{EC} \qquad (2.29)$$

$$I_{CC} = I_{C0}\ exp[\frac{q(V_{BE} + I_E R_E - I_B R_B)}{mkT}] \qquad (2.30)$$

$$I_{EC} = I_{E0}\ exp[\frac{q(V_{BC} + I_C R_C - I_B R_B)}{m'kT}] \qquad (2.31)$$

For a fixed I_B, and V_{CE}, the collector current can be calculated by putting previously calculated V_{BC} and V_{BC}, and previously extracted parameters into equations 2.28-2.31.

In order to fit the I_C - V_{CE} plot better in the high V_{CE} region, avalanche multiplication of carriers in the reverse-biased base-collector junction region needs to be considered. As V_{CE} is increased, the electric field in the BC junction is also increased. Hence, the injected electrons from the emitter are accelerated by the electric field across the BC junction, and gain sufficient energy to initiate the avalanche multiplication. Thus, the avalanche multiplication factor (M) is introduced into the collector current equation. The collector current now can be written as

$$I_{C,avalanche} = M \times I_C \tag{2.32}$$

where I_C given by eq. 2.28 is the collector current without multiplication. The avalanche multiplication factor (M) is voltage dependent , and can be expressed as

$$M = \frac{1}{[1 - (\frac{V_{CB}}{BV_{CBO}})^r]} \tag{2.33}$$
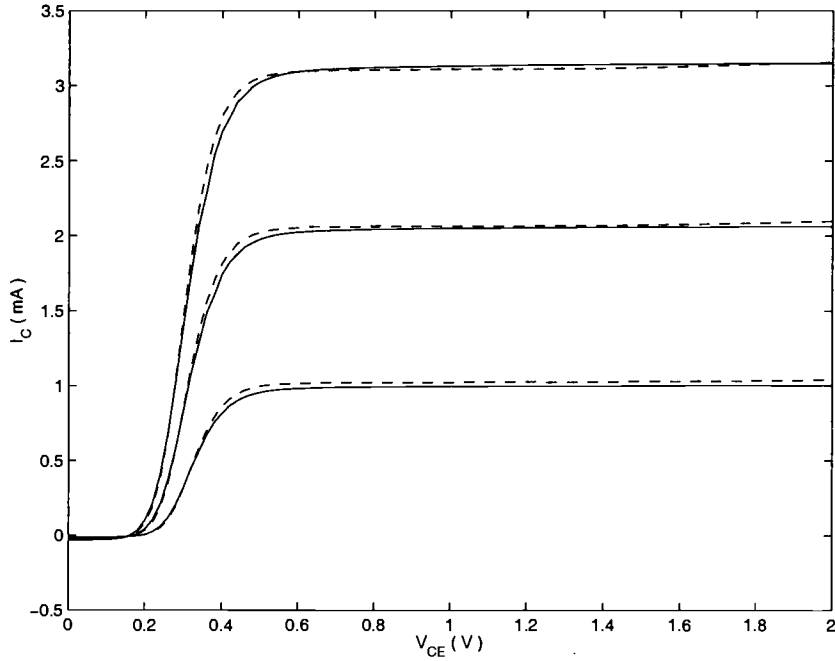
FIGURE 2.14. Comparison of the measured (solid lines) and the simulated (dashed lines) I_C - V_{CE} characteristics for three different base currents (sample D4O8).

where BV_{CBO} is the breakdown voltage of the common-base breakdown voltage, and r is an empirical constant. The value of BV_{CBO} can be measured from common-base breakdown voltage measurement. The empirical constant, r, then can

be estimated by fitting the slope of the experimental I_C - V_{CE} curve in the active region.

The simulated I_C - V_{CE} plot is shown in Fig 2.14. The simulated curves show good agreement to experimental curves, indicating the developed model is well suited to the InGaP/GaAs HBTs.

3. RADIATION EFFECTS IN SEMICONDUCTORS

3.1. Introduction

As electronic devices have become smaller in size and have increased in complexity, they are more sensitive to the radiation environment. The radiation-induced effects in semiconductor devices have become a big concern for the electronic systems employed in radiation environments. In space, energetic particles pass through the semiconductor devices and lose their energy by interacting with the atoms of the material. The two major consequences of energy transfer from radiation to semiconductor materials are ionization and atomic displacement, both of which may damage the performance of semconductor devices.

The radiation environment can cause the performance degradation of the electronic devices and in extreme circumstances lead to their loss. There are a variety of radiation environments to which semiconductor devices may be exposed. The various radiation environments give rise to a variety of irradiation particles with a wide variation in energy spectrum. The different irradiation particles may undergo different interactions with solid material and cause different types of damage in the solid material. Moreover, the specific radiation damage in soild material will cause the corresponding radiation effect in semiconductor devices. Hence, the knowledge of the radiation environments and radiation interactions is essential to the study of the radiation effect in semiconductor devices. The flow chart, Fig 3.1, gives an impression of the variety of the effects which radiation particles may cause in materials and devices. In this chapter, first, the radiation environments as well as the primary radiation composition are introduced. The radiation interactions

and radiation-induced damage in materials are subsequently discussed. Finally, the radiation effects on semiconductor devices and their basic mechanisms are described.

3.2. Radiation environments

There are a variety of radiation environments to which semiconductor devices may be exposed. The various radiation environments give rise to a variety of irradiation particles with a wide variation in energy spectrum. The one of most practical interest is space radiation. There are three naturally occurring sources of radiation in space: (1) the trapped particle belts (Van Allen belts) (2) solar particle events and (3) cosmic rays. The trapped particle belts are energetic particles that are confined to gyrate around the Earth's magnetic field lines. Solar particle events are energetic particles emitted during solar flare events. Cosmic rays consist of galactic and solar cosmic rays. The first two sources are relatively constant, but the third is highly time dependent. Any of these sources may be dominant, depending on the spacecraft orbital. However, protons are the dominant component among all three sources.

Trapped particle belts, first discovered by J. Van Allen and his collaborators, consist primarily of electrons of up to a few MeV energy and protons of up to several hundred MeV energy. They are trapped in the Earth's magnetic field; their motion in the magnetic field consists of a gyration about the field lines, a bouncing motion between the magnetic mirrors found near the Earth's poles, and a drift motion around the Earth [2]. The electron environment shows two flux maxima, inner belt and outer belt. The inner zone extends to about 2.4 earth radii ($R_e = 6380$ Km) and the outer zone from 2.8 to 12 R_e. The gap between 2.5 and 2.8 R_e is called the "slot". The outer belt envelops the inner belt. The proton environment does not exhibit two-zone characteristics like electron environment. The flux varies with
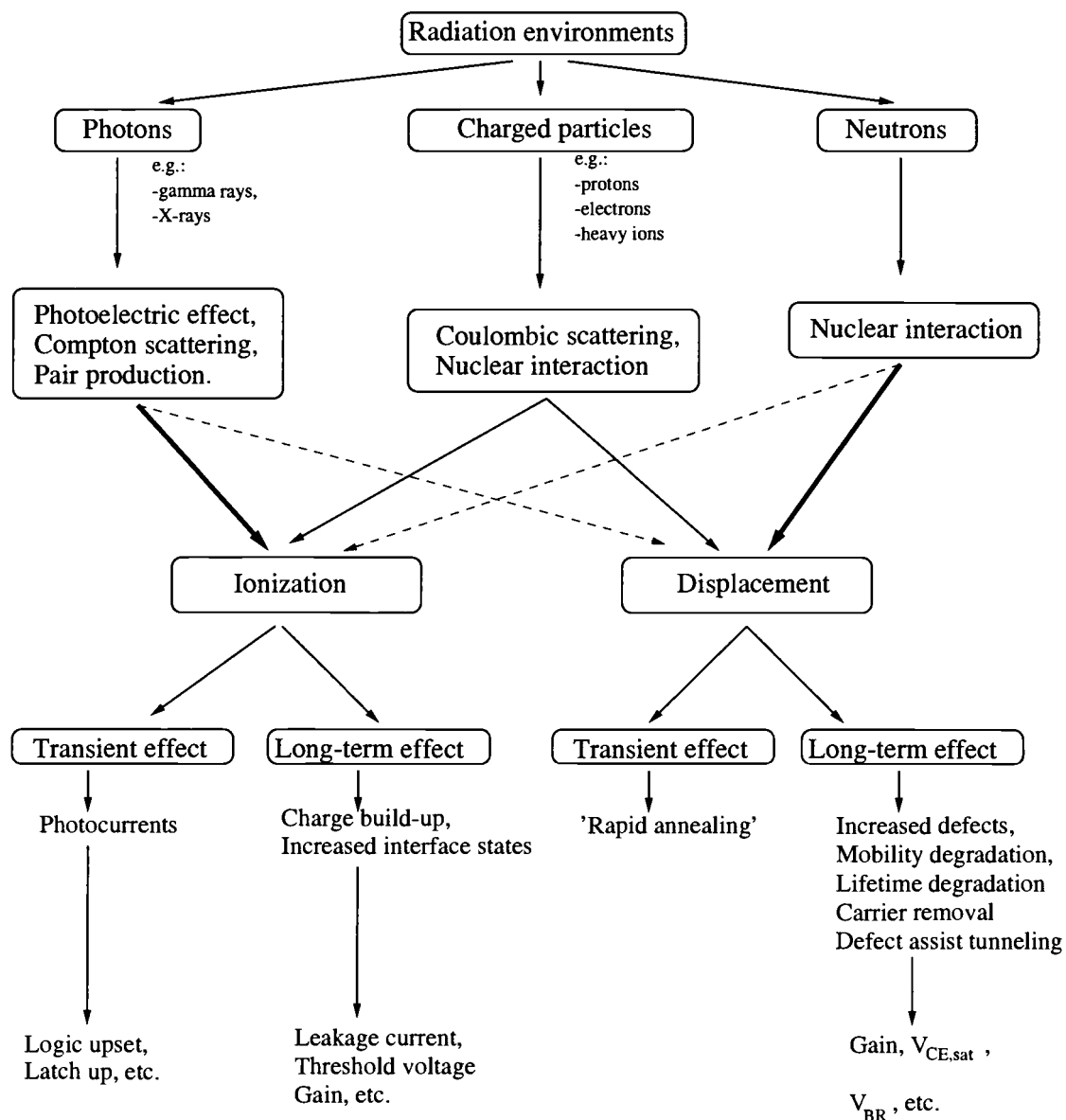
FIGURE 3.1. A flow chart of the radiation-induced damage on material and effects on devices.

distance from earth inversely and monotonically with energy. The outer boundery is at about 3.8 R_e. The trapped protons can have energy as high as 500 MeV [39]. A schematic of the radiation-flux contours for the Van Allen belts is presented in Figure 3.2 for electrons and protons.
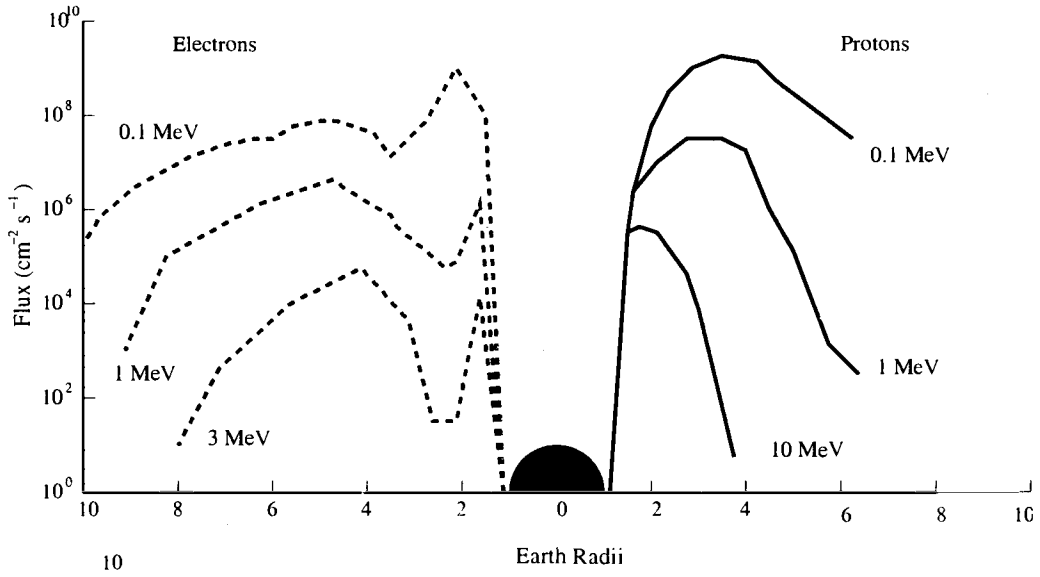
FIGURE 3.2. A schematic of the radiation-flux contours for the Van Allen belts for electrons and protons. (After reference [2])

In a solar flare event, solar flare protons, with a few electrons and heavy ions, are emitted by the sun in bursts during a solar storm. Their fluxes vary with the solar cycle. The energy spectra of solar protons are likely to be softer than those of trapped protons. Because the Earth's magnetic field exhibits a shield effect in the equatorial regions, but funnels protons into the polar regions. Thus, polar orbits may suffer severely from solar proton even at low altitude, whereas equatorial orbits will be shielded from solar protons except at high altitude.

There are two sources of cosmic rays: galactic and solar. Galactic cosmic rays are the primary constituent of the cosmic ray. Galactic cosmic rays originating outside the solar system constitute a continuous, low-flux ($\sim$ 4 particles/cm^2S) of energetic (10^8-10^{19} eV) ionized nuclei. They comprise about 85% proton, 14% alpha particles and 1% heavy ions with energies up to 1 GeV. Solar cosmic rays are the solar particles emitted by the sun during a solar flare. The amount of the solar cosmic rays is dependent on the solar activity. In a solar flare, the majority of the emitted particles are protons ($\sim$ 95%) and alpha particles.

Besides space, some other radiation environments to which semiconductor devices may be exposed are nuclear reactors, nuclear weapons and high-energy physics accelerators. In nuclear reactors and nuclear weapons, neutrons and gamma rays are the predominant constituents of the radiation. In high-energy accelerators, the secondary radiation which escapes from the accelerator tube consists mainly of photons and high-energy neutrons. The dose rates are of the order annually of 10^7 rad. Thus, the requirements for some parts in the accelerator are generally higher than those needed in space radiation or the military environment.

3.3. Radiation interactions with matter

The various radiation sources give rise to various radiation particles with wide variation in energy and dose rate. For example, the space environment consists of a low-level constant flux of energetic charged particles (protons, electron and heavy ions), whereas a nuclear explosion may give out strong pulses of neutrons and gamma rays. From the standpoint of radiation interaction with solid material, the various types of irradiation particles can be divided into three groups: (1) photons (x-rays, gamma rays); (2) charged particles (electrons, protons, alpha particles and heavy ions); and (3) neutrons. The interactions of the radiation with solid-material targets

depend on the mass, charge state, and kinetic energy of incident particle, and on the atomic mass, atomic number and density of the target material. There are a number of specific types of interaction that can take place for each group of irradiation particle mentioned above. The knowledge of the radiation interaction is essential for interpreting the types and degree of the damage introduced in semiconductor material for a specific radiation environment. The purpose of this section is to introduce physical mechanisms responsible for the damage produced by radiation particles.

3.3.1. Photon interactions

Photons interact with matter primarily through (1) photoelectric effect, (2) Compton scattering and (3) pair production. The types of interaction which the photon may undergo depend on the photon energy and atomic number (Z) of the target. The relative importance of the three photon interactions as a function of photon energy and Z is shown in Fig 3.3. In all three caeses, the interactions generate energetic secondary electrons.

In the photoelectric process, the photon is completely absorbed by the emitted outer-shell electrons of the target atom. The probability of a photoelectric interaction decreases with increasing photon energy and increases with Z of target. If the photon is energetic enough to kick out an inner-shell (K-shell) electron, subsequenct interactions are possible. An outer-shell (L shell) electron may subsequently drop down into the inner-shell vacancy and it can emit either an additional x-ray or a low-energy Auger electron. The schematic picture of photoelectric effect is shown in Fig. 3.4(a).

In Compton scattering, contrary to the photoelectric interaction, the high-energy incident photon is not completely absorbed because its energy is much higher
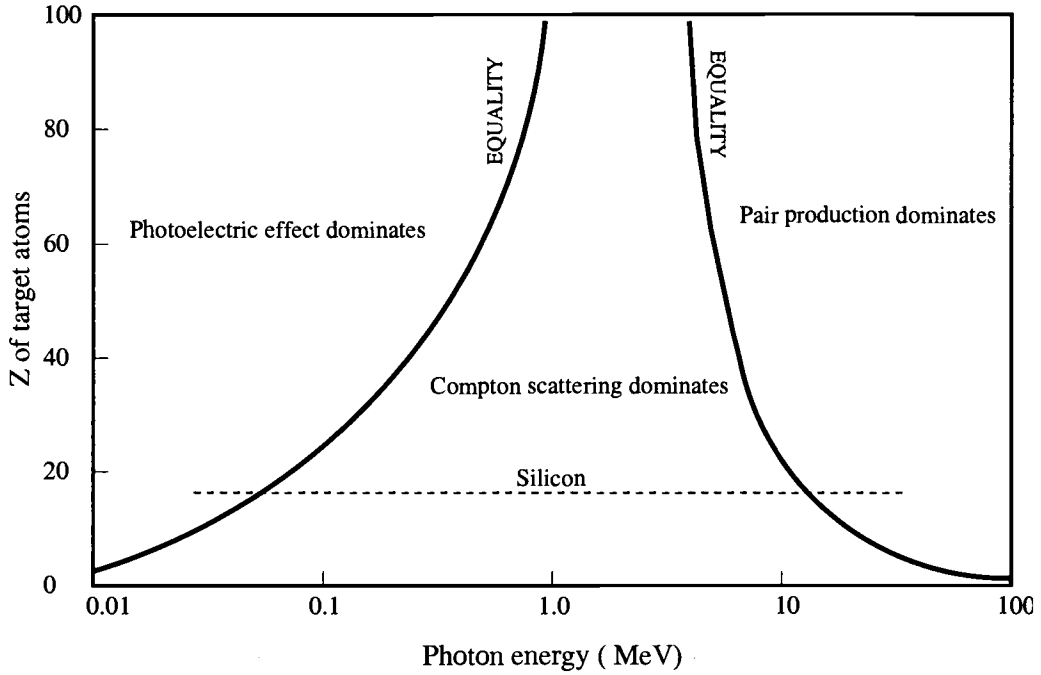
FIGURE 3.3. The relative importance of the three photon interactions as a function of photon energy and Z (After reference [40])

than the atomic-electron-binding energy of the target atom. The incoming photon gives part of its energy to the electron, then the scattered photon has lower energy, lower frequency and longer wavelength. The wavelength change in such scattering depends only upon the angle of scattering for a given target particle. The shift of the wavelength increases with the scattering angle according to the Compton formula:

$$\Delta\lambda = \lambda_f - \lambda_i = \frac{h}{m_e c}(1 - cos\theta) \tag{3.1}$$

where $\frac{h}{m_e c}$ = 0.00243 nm for electrons, called the Compton wavelength for the electron. The schematic picture of Compton scattering is shown in Fig. 3.4(b).

The pair production is an inverse process of pair annihilation in which a particle and a corresponding antiparticle encounter and annihilate with the production of two gamma-rays. The quantum energies of the gamma rays is equal to the sum

of the mass energies of the two particles (including their kinetic energies). In pair production, a high-energy photon gives up its quantum energy to the formation of a particle-antiparticle pair in its interaction with matter.

The rest mass energy of an electron, m_ec^2, is 0.511 MeV, so the threshold for electron-positron pair production is about 1.02 MeV. Above this energy, the highly energetic photon is completely transfering to a high-Z material to create a positron-electron pair. (A positron, an antiparticle of electron, has the same rest mass and charge as an electron, except that the charge is positive.) The schematic picture of pair production is shown in Fig. 3.4(c).

The products (electrons, photons, and positrons) of these interactions can further interact with the target material. It is very important to take these secondary effects into consideration when we estimate the radiation-induced damage in solid material. Also, all three photon interactions mentioned above produce energetic secondary electrons. These energetic electrons may further undergo different interactions with solid material. These charge particle interactions will be discussed in the next section.
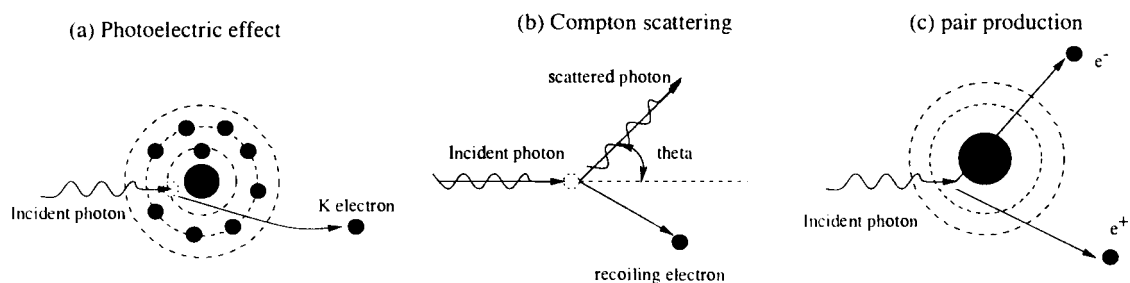
FIGURE 3.4. The schematic pictures of three photon interactions: (a) photoelectric effect, (b) Compton scattering and (c) pair production

3.3.2. Charged particle interactions

Charged particles, such as protons and electrons, interact with matter primarily through (1) Rutherford scattering and (2) nuclear interactions. The Rutherford scattering is typically the dominant interaction. In Rutherford (Coulomb) scattering, the charged particles interact with the electric field of the target atom. The schematic picture of Rutherford scattering is shown in Fig. 3.5. This interaction can cause both excitation and ionization of the atomic electrons. Additionally, the incident charged particle may transfer recoil energy E to a lattice atom, the so-called primary knock-on atom (PKA). For sufficiently energetic impacts, the recoil energy exceeds a material dependent displacement-threshold energy E_d and the PKA leaves its original lattice position, thus a Frenkel (vacancy-interstitial) pair forms. The maximum energy that can be transferred to an atom of mass M by an incident charged particle of mass m and energy E can be address as

$$\Delta E = 4E \frac{mM}{(m+M)^2} \tag{3.2}$$

According to this equation, the energy of the recoil atom for proton irradiation is higher than that for electron irradiation, if protons and electrons have the same energy.

If the displacement-threshold energy of the atom of mass M is E_d, the threshold energy for the incident particle to make a displacement is

$$E_{th} = E_d \frac{(m+M)^2}{4mM} \tag{3.3}$$

Some displacement threshold energy for the commonly used semiconductors are listed in Table 3.1 [41]. For example, E_d for Ga or As in GaAs is about 10 eV. The threshold energy for an electron to cause displacement in GaAs is approximately 290 KeV, whereas only 310 eV is required for protons.

incident charged particles flux

nucleus
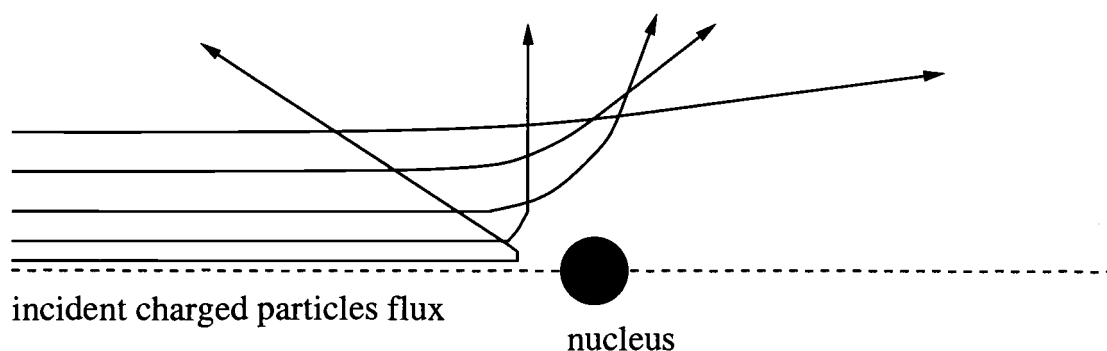
FIGURE 3.5. The schematic pictures of Rutherford scattering

While propagating through a solid, the PKA can cause further ionization and displacement before it comes to rest and the secondary knock-on atoms may knock out more atoms. Thus, depending on the initial kinetic energy of the PKA, the nature of the damage can vary from a simple Frenkel pair to a more complex cluster. We will discuss these radiation-induced ionization and displacement damage in semiconductors later.

In nuclear interaction, the incident particle actually interacts with the atomic nucleus. For example, a proton can be absorbed in a target nucleus, and the nucleus then emits an alpha particle. This process is also called spallation. The alpha particles produced in spallation, and the recoil atoms from displacement mentioned above can transform a proton environment into a heavy ion environment. Nuclear interactions can result in elastic or inelastic scattering and transmutation (through fusion or fission). We will discuss these three interaction mechanisms in more detail in the next section.

Atom	E_d (eV)
Si	21
Ga	10
As	10
In	6.7
P	8.7

TABLE 3.1. Displacement threshold energy for the commonly used semiconductors.

3.3.3. Neutron interactions

Neutrons incident on solid material undergo the following nuclear interaction: (1) elastic scattering, (2) inelastic scattering, and (3) transmutation. In elastic scattering, the neutron is not captured but transfers a portion of its energy into an atom of the target material, and can dislodge the atom from its normal lattice position. This process will occur as long as the imparted energy is larger than that required for displacement. The displaced atom (PKA) can in turn cause ionization or further displacement damage.

In inelastic scattering, the neutron is captured by the nucleus, and subsequently a lower-energy neutron is emitted. The kinetic energy lost in this process can result in the excited atomic nucleus or displacement. The excited nucleus then returns to its ground state by emitting a gamma ray. In transmutation, the neutron is captured by the atomic nucleus and the nucleus subsequently emits another particle such as a proton or an alpha particle. The remaining atom is hereby transmuted.

Thus, this process could make the semiconductor device itself radioactive in the long run.

3.4. Radiation damage

In spite of the seemingly complicated interaction between radiation and semiconductor materials, in the end there are two essential consequences on semiconductor material concerned. They are (1) displacement damage (atoms dislocated from their normal lattice sites) and (2) ionization (generation of electron hole pairs). In general, energetic particles traveling through semiconductor materials transfer a portion of their energy into ionization and the rest into atomic displacement. The amount of energy that goes into ionization is given by the stopping power, or the Linear Energy Transfer (LET), whereas that going into displacement is given by Non-Ionizing Energy Loss (NIEL).

3.4.1. Terminology of radiation exposure

Before go further into the specific effects of ionization and displacement damage in semiconductors, we need to introduce some commonly used terminology in radiation exposure and damage. A summary of these important terms and units is given on Table 3.2. Flux is the particle current density incident on a particular area. The fluence is the time integral of flux over some period of time. The energy spectrum is the distribution of a particle fluence over energy. For ionization radiation, the amount of energy going into ionization is given by the stopping power. The absorbed ionizing dose is the integral over energy of the product of the particle energy spectrum and corresponding stopping power. For displacement damage, NIEL (non-ionizing energy loss) is a calculation of the rate of energy loss due to the

Terminology	Units
Flux	Particles/cm^2·s
Fluence	Particles/cm^2
Energy spectrum	Particles/cm^2·Mev
For ionization:	
Stopping power	Mev/(g/cm^2)
Ionization radiation absorbed dose	rad
Ionization dose rate	rad/sec
For displacement damage:	
NIEL	Mev/(g/cm^2)
Displacement damage dose	rad

1 rad(Si) = 100 ergs/g;   1 Gy = 100 rad

TABLE 3.2. Terminology of radiation exposure.

atomic displacements as an incident particle traverses a material. The displacement damage dose is the integral over energy of the product of the particle energy spectrum and corresponding NIEL. We will discuss stopping power and NIEL in more detail in the later sections.

3.4.2. Displacement damage

As shown in Fig 3.1, the displacement damage is most likely caused by irradiation of neutrons or charged particles, such as protons. An energetic incident particle traversing the material may interacts with a lattice atom via one of the

mechanisms mentioned in previous sections to dislodge it from its normal lattice site , resulting in a Frenkel (vacancy-interstitial) pair (Fig.3.6). The recoil atom, or primary knock-on atom (PKA), may travel some distance in the lattice before it comes to rest. If it has sufficient high energy, PKA may introduce further displacements itself. Moreover, in some cases, secondary knock-on atoms can obtain sufficient high energy to dislodge more atoms. The reflected primary particle may also introduce more displacements as long as its kinetic energy is sufficiently high. Gossick [42] first proposed the possible existence of large disordered clusters in solids after high-energy particle bombardment. In his model, the defect clusters serve as very efficient regions for minority carrier recombination. Later, Summers *et al.* [44] further correlate the types of displacement damage with the PKA energy. At low PKA energies ($\sim$ 2KeV), isolated Frenkel pairs are formed. At intermediate PKA energies ($\sim$ 12 KeV), cascade-clusters are formed along with Frenkel pairs. At even higher PKA energies ($\sim$ 20 KeV), tree-like defect structures are formed with subcascade-clusters. A typical distribution of defect clusters produced by a 50 KeV Si recoil atom is shown in figure 3.7 [43].
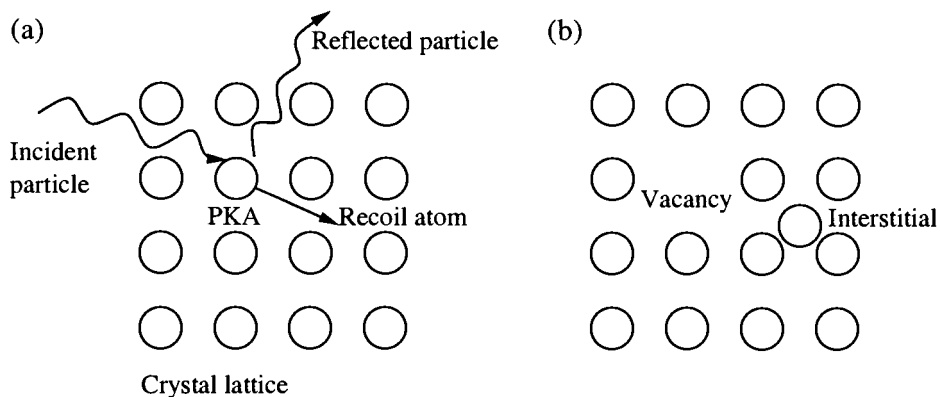
FIGURE 3.6. A schematic picture of (a) a displacement event and (b) a simple Frenkel defect.

As mentioned in previous sections, the electrons and protons interact with matter through Coulomb scattering. According to eq. 3.2, the energy of recoil atoms for electron irradiation is much smaller than that for proton irradiation. The energy of recoil atoms for high-energy electron irradiation is usually in the range of a few tens eV which is just slightly larger than the displacement threshold energy of commonly used semiconductors (see Table 3.1). Thus, only simple point defects (or Frenkel pairs) are expected in the electron irradiation. On the contrary, the energy of recoil atoms for high-energy proton irradiation is much higher. Hence, the defect clusters emerge. Moreover, the nuclear interactions become important in the higher-energy proton irradiation and neutron irradiation giving rise to high recoil energy. Therefore, large subcascade-clusters along with point defects are expected in these two cases.

The band-gap in semiconductors is a consequence of the periodicity of the lattice. The displacement defects disrupt the periodicity of the lattice resulting in localized states inside the bandgap. As a result, these states alter semiconductor device electrical properties. Depending on their energy position, they can act as: (1) Generation centers, (2) Recombination centers, (3) Trapping centers, (4) Compensation centers, (5) Tunneling centers, and (6) Scattering centers. A schematic picture of these centers are shown in Fig. 3.8 [45].

Generation centers are levels near midgap which are responsible for the thermal generation of electron-hole pairs, leading to increased dark currents in devices. As the energy level is moved from midgap, generation rates decrease exponentially. Thus, only centers with energy level near midgap make significant contribution to carrier generation. Recombination centers are the levels responsible for the recombination of electron-hole pairs. A free carrier of one sign, for example an electron, is first captured at a defect center, followed by the capture of a carrier of the opposite
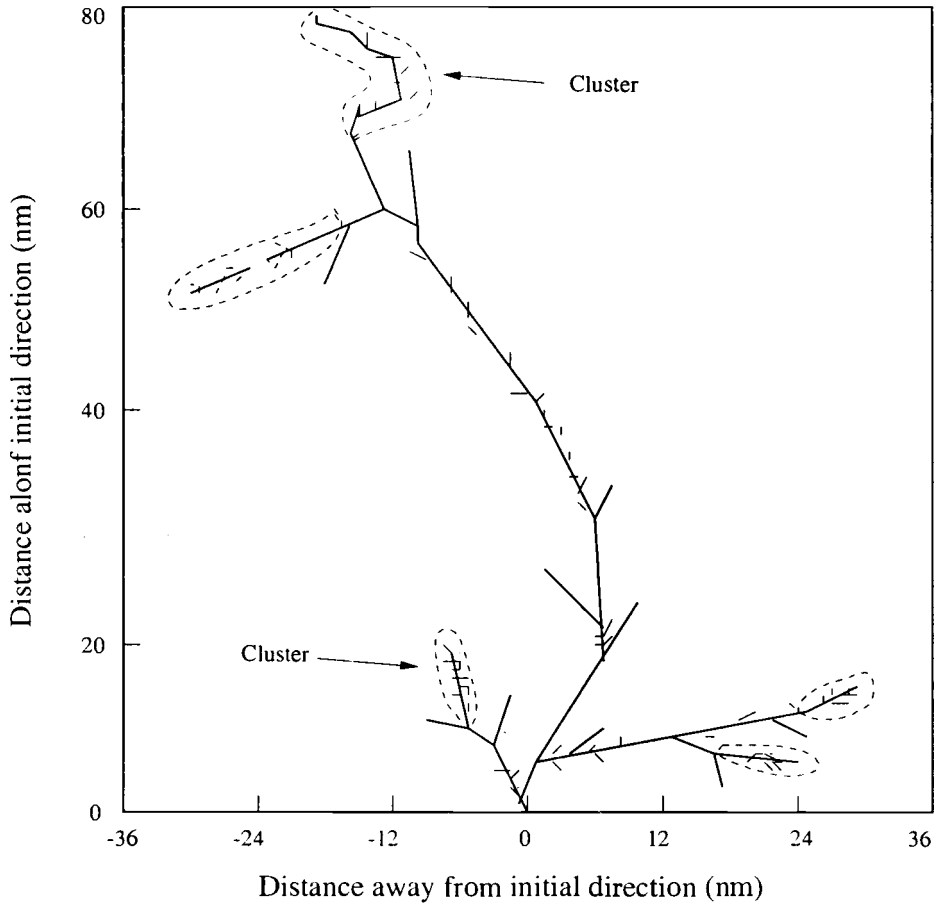
FIGURE 3.7. A schematic picture of typical distribution of defect clusters produced by a 50 keV Si recoil atom. (After reference [43])

sign, for example a hole. Radiation-induced recombination centers may result in a decrease of minority carrier lifetime and gain degradation in bipolar transistors.

Trapping centers are typically shallow levels near the band edges which can capture charges temporarily, and re-emit them back to their band. In general, trapping of both majority and minority carriers can occur, but at different levels. Radiation-induced traps are responsible for decreasing charge transfer efficiency in charge-coupled devices (CCDs). Compensation centers are deep levels which can compensate the majority carriers. As shown in Fig 3.8, some of the free electrons

from the donor level are compensated by deep acceptor levels. This process leads to the carrier removal effect which may alter the device properties which depend on the carrier concentration, such as the increasing collector resistance in bipolar transistors. The tunneling centers are responsible for trap-assisted tunneling which may result in increased junction leakage current. Finally, defects may serve as scattering centers, leading to carrier mobility degradation in devices. Basically, a defect level may serve as any combination of these centers, depending on some factors, such as temperature, carrier concentration, junction bias, and the device region in which it resides.

In short, the most important consequences of radiation-induced displacement defects in semiconductors are decreased minority carrier lifetime, decreased majority carrier concentration (carrier removal), and decreased carrier mobility. Those consequences may lead to performance degradation in semiconductor devices such as gain degradation in bipolar devices. These three major effects of displacement damage can be given by following equations:

$$1/\tau = 1/\tau_0 + K_\tau \Phi \tag{3.4}$$

$$1/\mu = 1/\mu_0 + K_\mu \Phi \tag{3.5}$$

$$N = N_0 + K_N \Phi \tag{3.6}$$

where τ_0 is the minority carrier lifetime, μ_0 is the carrier mobility and N_0 is the carrier concentration prior to irradiation, K_τ, K_μ and K_N are corresponding damage coefficients, and Φ is incident fluence. The value of damage coefficient depends on the type and energy of radiation.

The degradation of bulk electric properties of semiconductor materials has been shown proportional to the absorbed energy that produces atomic displacement,
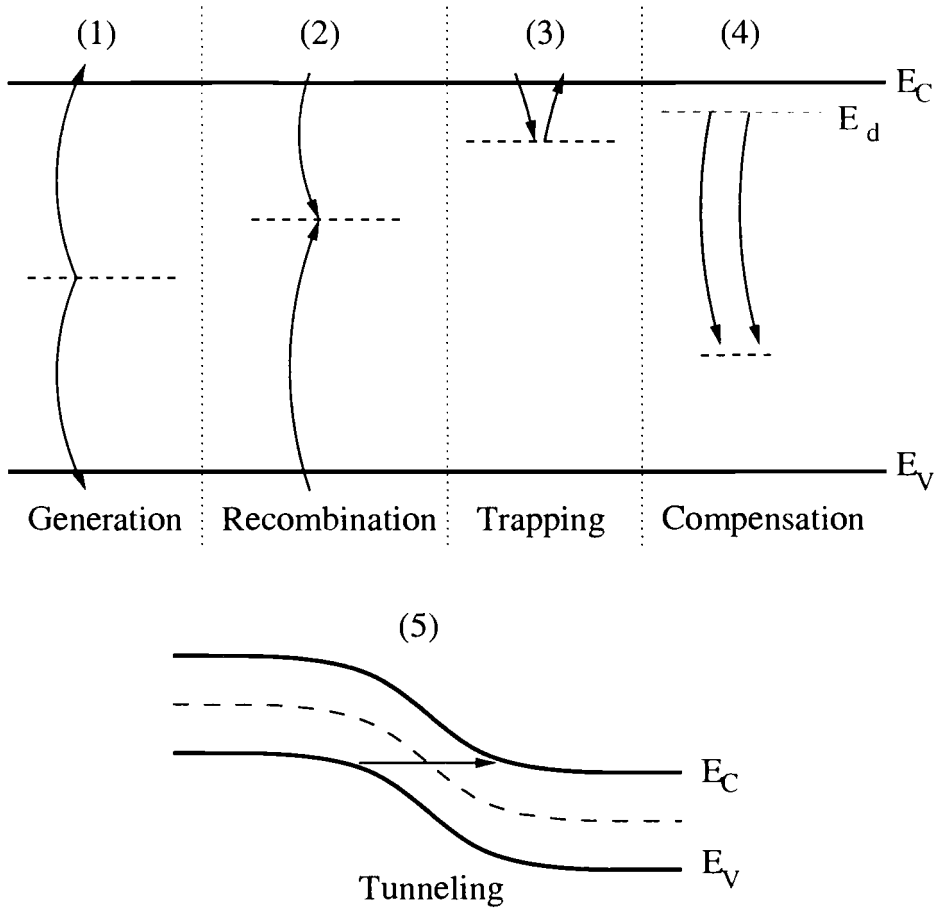
FIGURE 3.8. Electrical effects associated with defect centers in bandgap

e.g. to NIEL [48]. Thus, the damage coefficients used in eqs. 3.4-3.6 may be expressed in terms of NIEL:

$$K_D \propto NIEL \tag{3.7}$$

The concept of NIEL has been widely accepted for correlating displacement damage caused by different types of radiation (e.g. protons, electrons) with different energy spectrua. Thus, the radiation-induce displacement damage in semiconductors can be analyzed quantitatively by non-ionizing energy loss, NIEL. The NIEL can be written as [46]

$$NIEL = \frac{N_A}{A} \int_{\Theta_{min}}^{180^o} L[T(\Theta)] \frac{d\sigma(\Theta)}{d\Omega} d\Omega \tag{3.8}$$

where N_A is Avogadro's number, A is the atomic mass, $T(\Theta)$ is the trans-ferred energy to the target atom nucleus by an incident particle scattered with an angle, $d(\Theta)/d\Omega$ is the differential cross section for elastic scattering of particles into a solid angle increment $d\Omega$,and $L[T(\Theta)]$ is the Lindhard partition factor which es-timates the fraction of transferred energy that is non-ionizing [47]. The lower limit, Θ_{min}, on the integral is the scattering angle for which the recoil energy is equal to the displacement threshold energy. Fig. 3.9 shows electron and proton NIEL in various semiconductors up to 100 MeV [46].

While NIEL has been successful in correlating the displacement damage in silicon devices, some discrepancies have been reported in GaAs devices [49]. In the regime of radiation energies that produce high-energy recoils, the degradation is smaller than that expected from NIEL calculation. One possible explanation is the defect clusters of increasing size produced by high-energy recoil atoms are less effective in the degradation of the bulk properties than constituent defects acting individually.

3.4.3. Ionization

Ionization is primarily caused by the irradiation of photons, such as gamma rays, and charged particles, such as electrons. Since no momentum transfer to the nucleus, the energy required to create an electron-hole pair is relatively small comparing to that for displacement. The energies required to produce an electron-hole pair for some common used materials in semiconductor devices are listed in Table 3.3 [45].
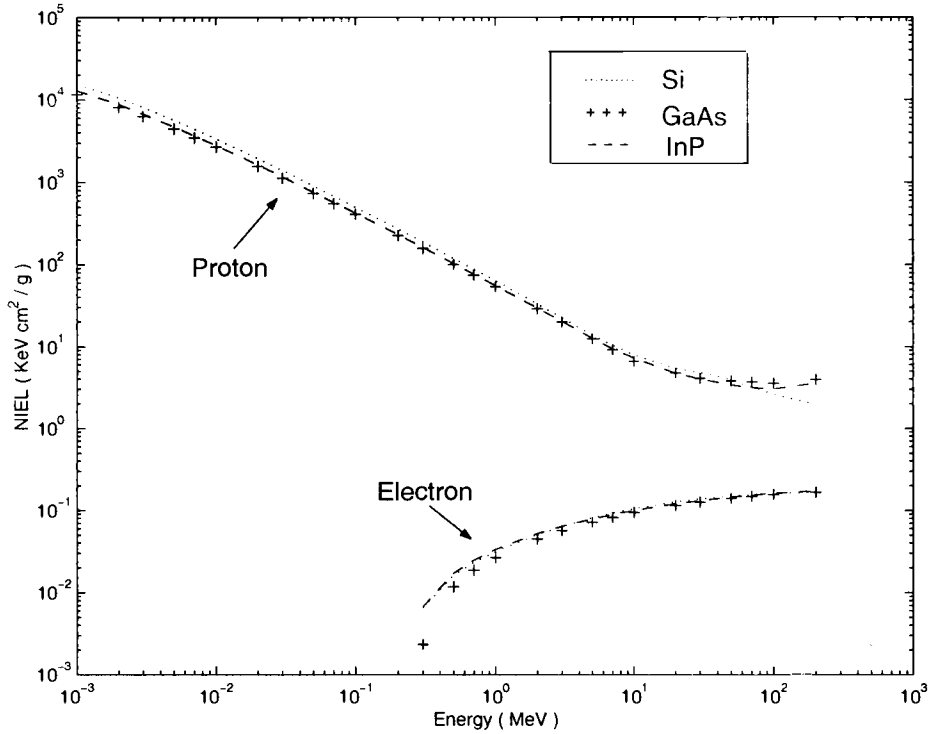
FIGURE 3.9. The electron and proton NIEL in various semiconductors up to 100 MeV [46]

Ionization occurs when an electron in the valence band is excited into a conduction band. In semiconductors (or conductors), the electrons and holes are free to diffuse and drift (if an electric field is applied). Most of the excited electrons in the conductor band and the holes in the valence band soon undergo recombination and hence no long-term radiation effect observed. However, if an electric field is present, the generated electrons and holes get separated resulting in electric currents. These radiation-induced photocurrents may cause fatal problems, such as the transient upset and current latchup, in semiconductor devices.

It is another story in insulators. In insulators, such as SiO_2, the radiation-induced photocurrents are generally not a problem due to the low carrier mobilities,

Material	Pair generation energy (eV)
Si	3.6
SiO_2	17
GaAs	~4.8
Ge	2.8

TABLE 3.3. Electron-hole pair generation energies.

and fewer charges created. However, the ionization goes through the following physical processes: (1) electron-hole pairs generation and initial recombination, (2) charge transport in which positive charges are not very mobile, and some are trapped, while the electrons produced are mobile and removed [45], (3) hole trapping in the oxide. These trapped charges result in radiation-induced oxide charges. The fraction of holes trapped near the interface depends on how the oxide is grown and annealed. For unhardened gate oxide, 20-40 percent of the holes reaching the interface may be trapped. After being trapped, these holes undergo a slow detrapping process primarily due to the tunneling of the electrons. In addition to the trapped holes, ionization radiation also introduces interface traps at the Si/SiO_2 interface. A schematic diagram for these processes is shown in Fig 3.9 [45]. The combined effect of these two mechanisms is the change of the electric field leading to the threshold voltage shift in device operation characteristics. The radiation-induced threshold voltage shift (ΔV_T) can be written as

$$\Delta V_T = V_T - V_{TO} = \Delta V_{ot} + \Delta V_{it} \tag{3.9}$$

where V_T and V_{TO} are the threshold voltages after and before irradiation, respectively. ΔV_{ot} is the change in the threshold voltage due to oxide trapped charge, and ΔV_{it} is the change due to interface traps. This is a major radiation-induced problem in metal-oxide-semiconductor (MOS) devices. In addition to the radiation effects on the gate oxide, the trapped charges in the field oxide and passivation insulator may give rise to radiation-induced leakage currents leading to another major problem. As semiconductor devices are smaller, this is becoming more important in both MOS and bipolar technologies.

The behavior of the ionization associated degradation is usually time dependent, because of the different introducing rates between the trapped holes and interface traps. For example, in thin-gate oxide, the holes are trapped in microseconds whereas the interface traps may take seconds to hours to form. As a result, the ionization effect is not only a function of the total dose but also of the dose rate.
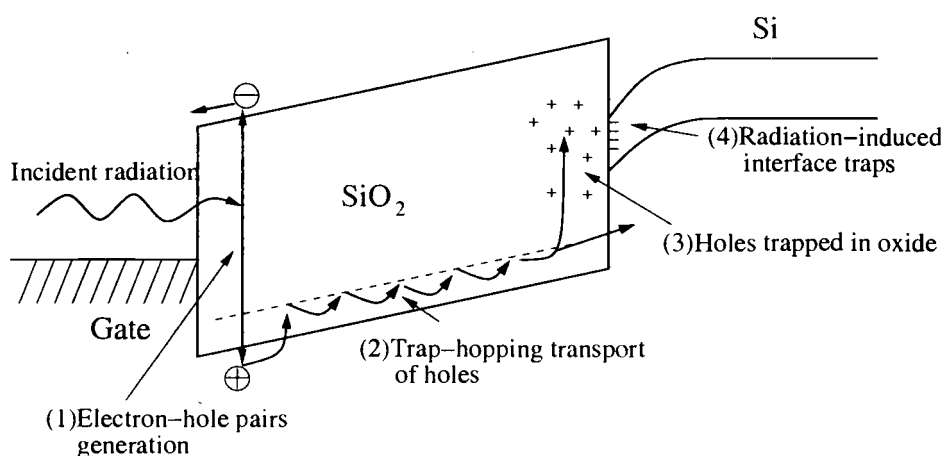
FIGURE 3.10. A schematic diagram for processes of ionization in the oxide

The radiation-induced ionization can be analyzed quantitatively by the stopping power, s, which is also termed linear energy transfer (LET) from health science terminology. The stopping power can be written as

$$s = \frac{dT}{dx} \tag{3.10}$$

where dT is the amount of energy released by a radioactive particle or wave as it transverses matter of thickness dx.

3.5. Measures of radiation effects

The various radiation environments give rise to a variety of irradiation particles with a wide variation in energy spectrum and dose rate. The space environment consists of a low-level constant flux of energetic charged particles (protons, electrons, etc), whereas nuclear explosion may give out strong pulses of neutrons and gamma rays. Although the different particles may undergo different interactions with semiconductors and do various damages in semiconductors, the overall radiation-induced performance degradation in semiconductor devices can be inspected by three effects: (1) total dose effect, (2) dose rate effect, and (3) single event effect.

Total dose effect is studied by subjecting the semiconductor devices to ionizing radiation and serves as a measure of determining the total radiation dose at which a device can sustain before it fails to operate reliably. This measure only concerns the total energy that goes into the semiconductors in spite of the radiation of various types and energy spectrum. It is very useful in predicting the expected radiation-induced degradation in semiconductor devices in a real environment, such as space or a nuclear reactor, from laboratory-based test measurements. This study covered the total dose effects of proton irradiation on III-V compound semiconductor HBTs.

Dose rate effect is used to characterize the performance degradation caused by the time variation of radiation flux. Measurements of performance degradation in devices at the end of irradiation to a fixed total dose but delivered at different dose rates usually will show different results.

The dose rate characterization is appropriate for devices used in nuclear weapons which may take up bursts of radiation in very short pulses. Such devices may fail long before they receive the radiation dose specified by total dose tests. Hence the devices employed in such an environment need to be tested at the high dose rate. On the other hand, devices used in space application which may receive relatively low dose rate radiation are expected not suffering the dose rate effect. However, the enhanced degradation of bipolar devices under low dose rate has been observed recently [81]. These enhanced low dose rate effects (ELDRS) have been contributed to the delayed transportation of defects, e.g. hydrogen, after irradiation. Therefore, in order to take this effect into account, the devices used in space application may need to be tested under the dose rate similar to that encountered in space orbital. This has presented a considerable challenge to the radiation hardness community, since the test may take years at such a low dose rate.

Single event effect (SEE) is caused by charge collection at sensitive nodes due to particle irradiation. Protons and heavy ions are the major sources of SEE in space. SEE may not only cause single event upset (SEU), or 'soft error', in memory elements, but may also lead to latch-up in circuits. SEU is the change of state of a bistable element caused by ionization of a single energetic particle , such as an heavy ion or proton. The ionization induces a current pulse in a p-n junction. The charge injected by the current pulse at a sensitive node may excess the critical charge, and hence, the logic state changes. This upset is nondestructive and may be corrected by 'rewriting' the affected component.

3.6. Radiation effects in III-V compound semiconductors

III-V compound semiconductors are semiconducting crystalline materials similar to silicon. Hence, they are subject to the same basic radiation damage that takes place in silicon, e.g. ionization and atomic displacement. However, there are some different consequences of the radiation damage on the electric characteristics of III-V compounded semiconductor devices. In general, the radiation hardness of III-V compounded semiconductor devices is superior to that of silicon devices.

The resistance of III-V compounded semiconductors to total dose ionization effect is mainly due to (1) no gate oxide employed in III-V compounded semiconductor devices, and (2) the absence of parasitic current leakage paths under passivation insulators. The latter factor is a result of very high interface-state densities for III-V compounded semiconductors before radiation, leading to a pinned Fermi level which makes inverting surface regions very difficult. Additionally, III-V compounded semiconductors also have higher tolerance for minority carrier degradation due to displacement damage, because of their shorter initial carrier lifetime. As previously discussed, the damage coefficient can be a function of NIEL. Several groups have reported that the damage coefficient is linear proprotion to NIEL (eq. 3.11) for proton irradiation on Si, GaAs and InP [46, 51, 52]:

$$K \propto NIEL \tag{3.11}$$

However, unlike the results from proton irradiation, electron irradiation damage coefficients do not always show a linear relationship with NIEL. In p-type Si, the damage coefficients show a quadratic dependence on the electron NIEL (eq. 3.12), while n type silicon and GaAs shows an approximately linear dependence on NIEL [53–55].

$$K \propto NIEL^2 \tag{3.12}$$

3.7. Radiation effects in HBTs

A few radiation effects on Si/SiGe, AlGaAs/GaAs and InP/InGaAs have been reported [56–58, 7–9]. The radiation may lead to the carrier removal and carrier mobility decrease through displacement and to oxide trapped charges and surface states through ionization in HBTs. The main manifestation of radiation-induced degradation in III-V HBTs is the current gain degradation due to the excess radiation-induced base current. This excess base current can be attributed to (1) the increase of recombination current in BE junction SCR and (2) the increase of surface recombination current in BE junction periphery after irradiation. The relative contribution from these two components hinge upon the ratio of device emitter perimeter to its area (P/A) [9]. In neutron irradiation, the results show the gain degradation is not sensitive to P/A, thus the majority of the excess base current may come from the former component. It may imply that the main degradation mechanism is the displacement in neutron irradiation. On the other hand, in gamma irradiation, the main degradation mechanism may be the ionization.

4. RADIATION EFFECTS IN HBTS

4.1. Introduction

After having introduced the radiation effects in semiconductor materials and developed the HBT model in the earlier chapter, we are now ready to analyze the experimental results of the proton irradiation in HBTs. Proton irradiation is chosen as the topic of this study, since it is one of the dominant component of space radiation environment. In addition, the charged nature of protons, which can cause both ionization damage and displacement damage, makes proton irradiation extremely interesting in the study of radiation effects. In general, proton irradiation could lead to displacement damage and introduce scattering centers which can reduce carrier mobility and minority carrier lifetime, and hence degrade the current gain (β) in HBTs [60]. On the other hand, ionization damage of proton irradiation could produce interface states and trapped charges in the passivation layer (e.g. oxide, polyimide etc.) over the space-charge region [59]. In this chapter, a study of proton irradiation effects in InGaP/GaAs SHBTs is presented. First, the experimental detail will be addressed. The effects of proton irradiation on the dc characteristics of InGaP/GaAs HBTs will then be presented. The analyses of radiation-induced damage on semiconductor materials are based on the methods discussed in Chapter 3. The measurements of the radiation-induced performance degradation in SHBTs are based on the configurations discussed in Chapter 2, while the analysis of the radiation effects on SHBTs is based on previously dicussed expanded Ebers-Moll (EM) models. The basic mechanisms of the radiation effects are also disscussed. A conclusion will be given at the end.

4.2. Device Structures

The InGaP/GaAs HBTs used in this study were grown on GaAs substrates either by MBE or by MOVPE techniques at Infineon Technologies Laboratory, Germany. The HBT epitaxial structure consists of a 700 nm n-type heavily doped GaAs subcollector, a 20 nm n-type InGaP subcolletor etch-stop, a 50 nm n-type heavily doped ($5.0 \times 10^{18} cm^{-3}$) and 700 nm lightly doped GaAs collector, a p-type heavily doped GaAs base, a 40 nm n-type doped ($4.0 \times 10^{17} in^{-3}$) InGaP emitter, a 150 nm n-type doped ($4.0 \times 10^{17} cm^{-3}$), and a 50 nm n-type heavily doped ($6.5 \times 10^{17} cm^{-3}$) GaAs emitter cap, a 50 nm graded layer from GaAs to $In_{0.5}Ga_{0.5}As$ and 50 nm heavily doped $In_{0.5}Ga_{0.5}As$ contacting layer. The devices tested in this study have three emitter sizes, 3.2×10, 3.2×14, and 3.2×30 μm^2, respectively. All connections are fabricated by airbridge technology. A schematic cross-section of the HBT device is shown in Fig. 4.1.

4.3. Experimental Detail

Proton irradiation of the devices was performed at the proton irradiation facility (PIF) in TRIUMF Canada's National Laboratory in Vancouver, B.C., Canada. The devices were mounted on circuit boards with terminals floating and exposed to protons at normal incidence to the surface of the samples. The devices are exposed to either 67 Mev protons with 3.22×10^7 $p/cm^2 \cdot sec$ flux or to 105 MeV protons with 2.24×10^7 $p/cm^2 \cdot sec$ flux. The samples were irradiated to cumulative proton fluences up to 3.0×10^{12} p/cm^2. The samples were characterized after the samples cooled down typically 48 hours, until their radioactivity had reached the acceptable safety limits. Some annealing of the defects may happen during this period, however, a stable condition was reached after this delay, which may actually help in
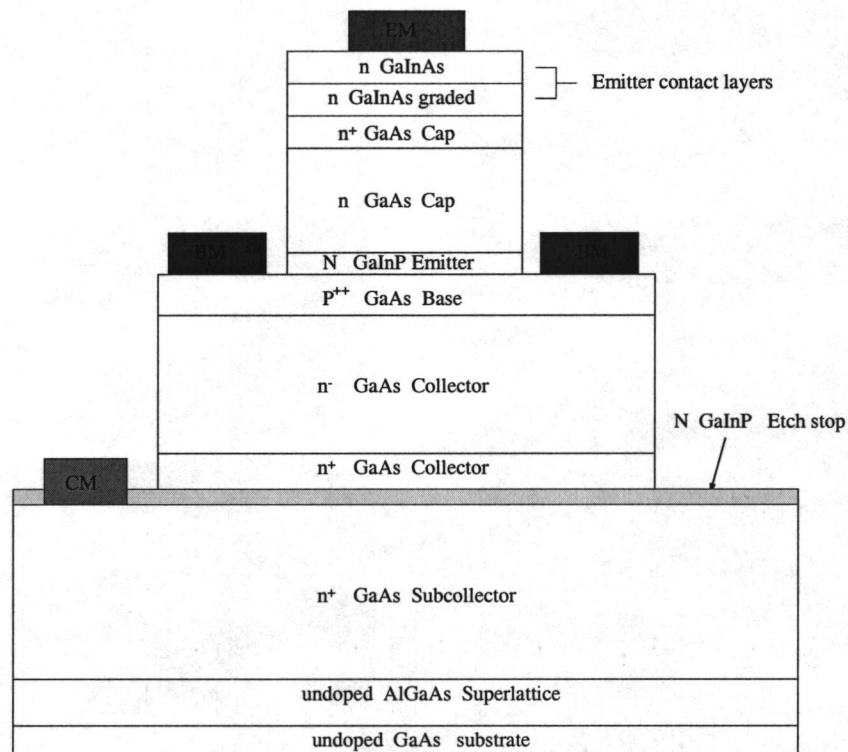
FIGURE 4.1. A schematic cross-section of the HBT device.

obtaining reproducible results. A number of dc measurements were conducted using a HP 4145B parameter analyzer: (1) Common emitter I-V measurement (I_C - V_{CE}); (2) forward Gummel measurement; (3) inverse Gummel measurement; (4) common emitter current gain (h_{FE}) measurement; (5) base-emitter diode characteristics measurement; (6) base-collector diode characteristics measurement; (7) common-base breakdown voltage (BV_{CBO}) measurement.

The measurement configurations are the same as the ones discussed in chapter 2, shown in Fig. 2.7 and Fig. 2.8.

4.4. Proton effects on InGaP/GaAs HBTs

In general, proton irradiation will create generation/recombination (R/G) centers, which effectively reduce the minority carrier lifetime, and hence degradate the current gain in semiconductor devices through atomic displacement. In addition, due to its charged nature, the ionization damage may introduce interface states and trapped charges in the passivation layers. In this section, the effects of the proton-induced bulk defects, interface states and trapped charges on the DC characteristics of InGaP/GaAs HBTs will be discussed.

According to the previous studies on AlGaAs/GaAs HBTs [7–10] and Si/SiGe HBTs [56–59], the main radiation-induced degradations on HBT devices are (1) current gain degradation, (2) shift of offset voltage ($V_{CE,off}$) and (3) breakdown voltage degradation. Fig. 4.2 shows the typical common emitter $I_C - V_{CE}$ characteristics of InGaP/GaAs HBTs measured in this study before irradiation and after 3.0×10^{12} p/cm^2 proton irradiation. The most salient degradation effect shown in Fig. 4.2 is the reduction of the collector current for a constant base current, implying the common-emitter current gain degradation. Fig. 4.3 shows the low V_{CE} and low I_C region of Fig. 4.2. It shows almost no shift in offset voltage ($V_{CE,off}$) and indicates InGaP/GaAs HBTs in this study are not sensitive to the radiation-induced offset voltage ($V_{CE,off}$) shift.

4.4.1. Current Gain Degradation

The reduction of the collector current at a constant base current shown in Fig. 4.2 indicates DC current gain ($\beta = I_C/I_B$) degradation after proton irradiation. In order to study the gain degradation phenomenon in more detail, the common-emitter current gain ($h_{FE} = I_C/I_B$) measurement is carried out by measuring the
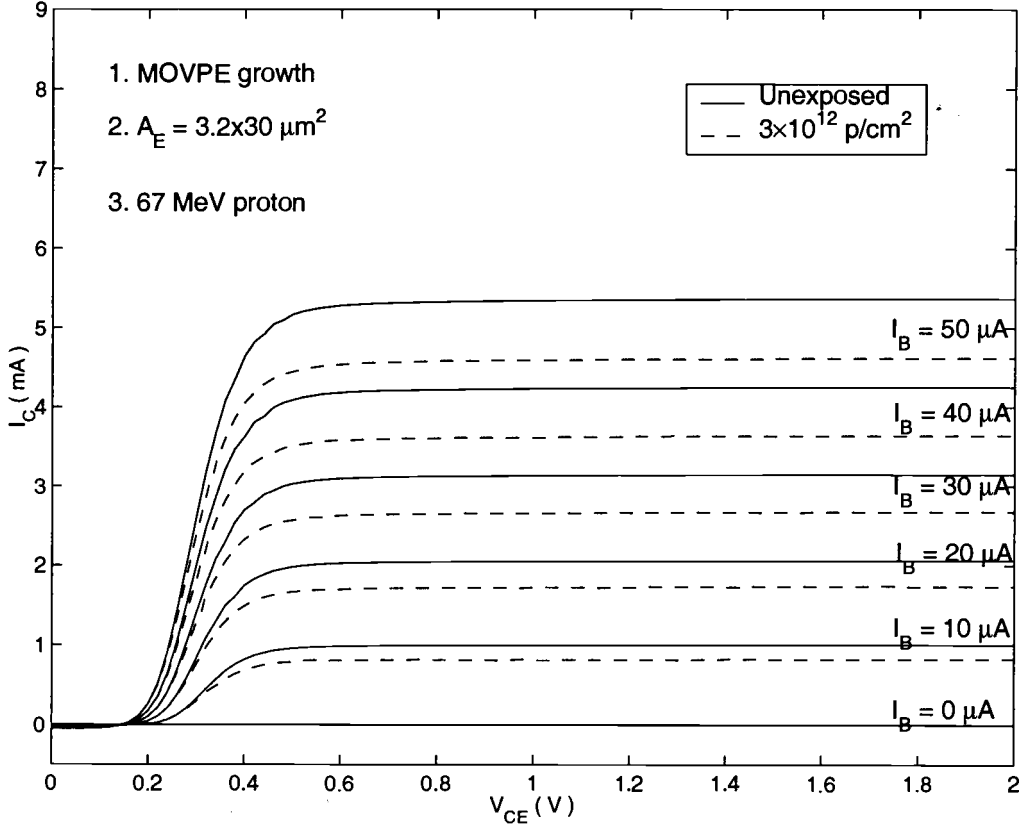
FIGURE 4.2. The common emitter $I_C - V_{CE}$ characteristics of InGaP/GaAs HBTs before irradiation and after 3.0×10^{12} p/cm^2 proton irradiation.

collector current by sweeping the base current. The DC current gain of the devices as a function of proton fluence at two different base currents are shown in Fig. 4.4a. The current gain increases sightly at lower irradiation fluence, before degrading at higher fluence. The current gain degradates steadily at higher proton fluence. The current gain decreases from 109.5 to 100.6 at $I_B = 90$ μA, an 8% degradation, while it decreases from 98.7 to 88.8 at $I_B = 10$ μA, a 10 % degradation after 3×10^{12} p/cm^2 proton irradiation. Compared to the other HBTs previously studied in our group, InGaP/GaAs HBTs are quite robust against proton induced gain degradation.
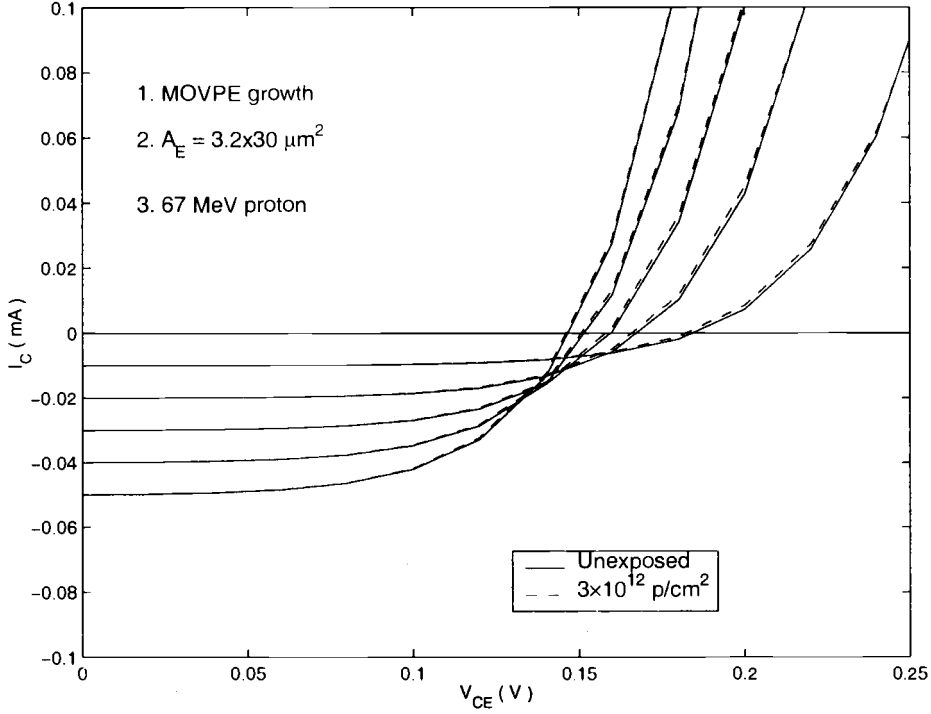
FIGURE 4.3. The common emitter $I_C - V_{CE}$ characteristics of InGaP/GaAs HBT measured before irradiation and after 3.0×10^{12} p/cm^2 proton irradiation.

In general, the current gain degradation at a constant collector current should follow Messenger-Spratt relation

$$\frac{1}{\beta} = \frac{1}{\beta_0} + K_\beta \Phi_P \tag{4.1}$$

where $1/\beta_0$ is pre-irradiation DC current gain, $1/\beta$ is the post-irradiation DC current gain, Φ_P is the proton fulence, and K_β is the gain degradation coefficient. The reciprocal current gains $(1/\beta)$ of the devices as a function of proton fluence at two different base currents are shown in Fig. 4.4 b. The current gain degradation obeys Messenger-Spratt relation in both cases. The gain degradation coeffecient, K_β, can be extracted from the slope of the fitting line. The gain degradation coeffecients are $2.74 \times 10^{-16} cm^2/p$ for I_b=90 μA and $3.76 \times 10^{-16} cm^2/p$ for I_b=10 μA. Thus, the
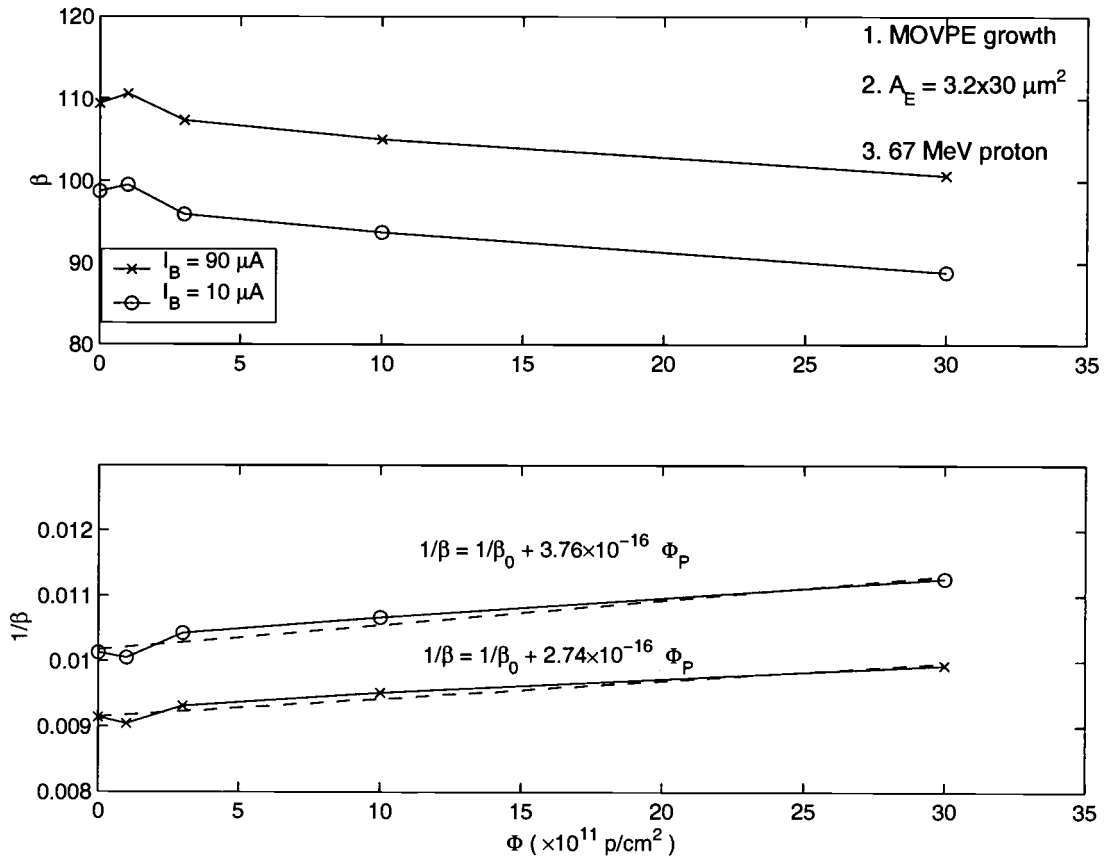
FIGURE 4.4. (a) The DC current gain and (b) the reciprocal gain as a function of proton fluence at two different base currents.

HBT devices suffer slightly more proton-induced gain degradation at lower operating current density.

Fig. 4.5 shows the DC current gain as a function of the base current before and after proton irradiation. Before irradiation, the current gain increases with the base current. It is due to the contribution of SCR recombination current component at lower base currents. After the first dose irradiation, the current gain increased slightly. At higher irradiation fluence, the current gain degraded with increasing
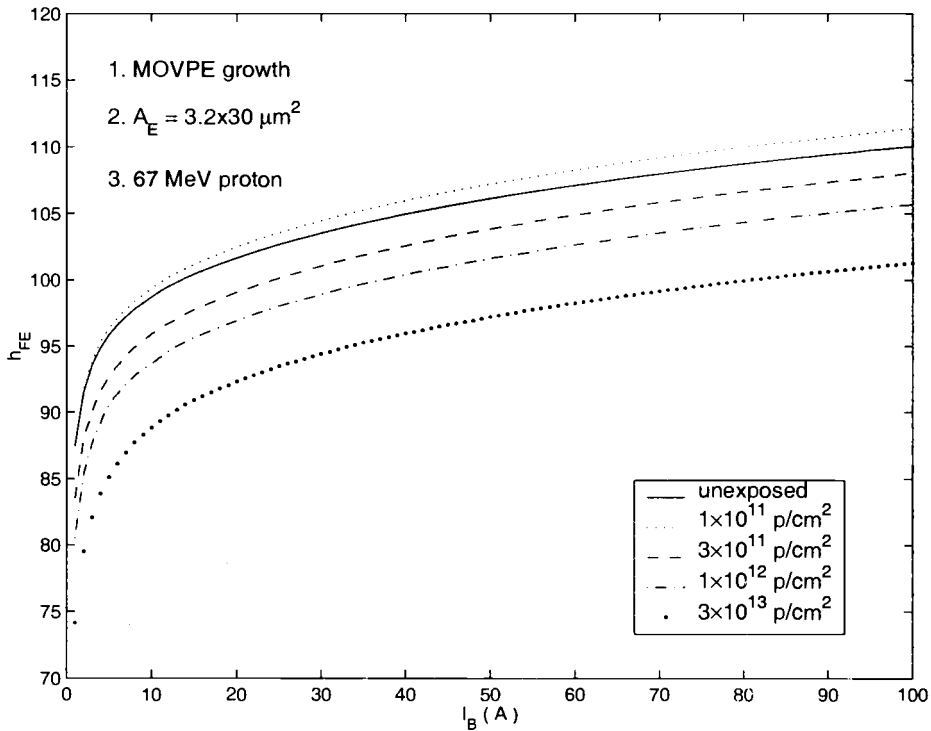
FIGURE 4.5. The common emitter current gain as a function of base current for pre-irradiated and post-irradiated sample at V_{CE}=1.5 V.

proton irradiation fluence. As expected, current gain degrades more as base current decreases. For example, the current gain degrades more than 10% at lower base current region, while it only degrades less 8% at higher base current region. Thus, a conclusion may be drawn here that InGaP/GaAs HBT devices employed in the radiation environment should operate at a higher current level where the current gain degradation can be minimized.

4.4.1.1. Current Gain Improvement at Low Fluence

As mentioned in the last section, the DC current gain of HBT increases slightly at low proton irradiation fluence. Similar radiation-induced improvement

of electronic properties at low fluence irradiation also has been observed in GaAs devices in previous works. It has been reported that the mobility, the minority carrier lifetime, the carrier concentration and the photoluminescence intensity may increase upon irradiation at small fluence [61–65]. It has been proposed that irradiation may restructure the semiconductor crystal, leading to the improvement of electronic properties. Borskovskaya *et al.* proposed a similar process, which they called "radiation induced order effect" that occurs through radiation-stimulated gettering in the semiconductors [62]. They have suggested that radiation-induced order is due to the migration of recombination centers to the surface or interfaces. However, we believe the gain improvement in our devices may be attributed to the irradiation induced charges in passivation layers. As mentioned in Chapter 3, proton irradiation may cause ionization effect which could introduce the charges in the polyimide passivation layer and interface states. Contrary to the slicon dioxide, previous work in our group shows that the irradiation introduces negative charges into the polyimide passivation layers [67]. These negative charges may cause an accumulation layer in the base region and reduce the surface recombination leading to a suppression of the base leakage current ($I_{B,lk}$) [66]. The forward Gummel plots before and after $1 \times 10^{11} p/cm^2$ proton irradiation are shown in Fig 4.6. This figure shows the suppressed base leakage current in the low bias region ($V_{BE} \leq 1$ V), while the collector current shows little change after first dose proton irradiation.

4.4.1.2. Current Gain Degradation Mechanism

After exposure to higher dose irradiation, HBTs show current gain degradation with increasing irradiation fluence. The main mechanism for the gain degradation is due to the increased base current after irradiation. Fig 4.7 shows the forward Gummel plots of the device before and after the highest dose proton irradiation. Col-
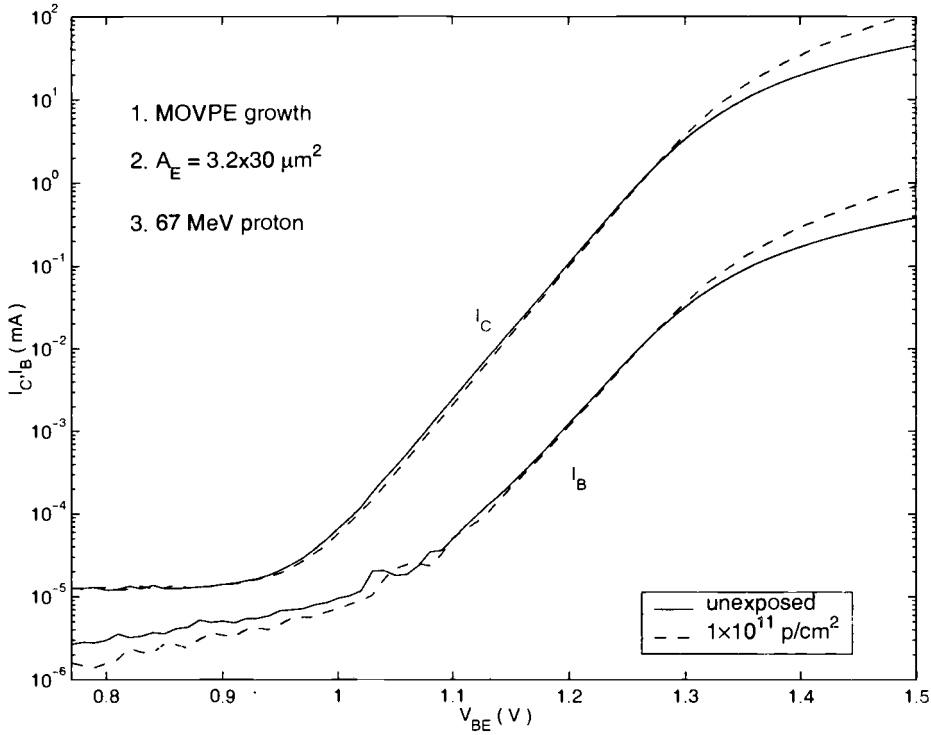
FIGURE 4.6. The forward Gummel plots before and after $1 \times 10^{11} \ p/cm^2$ proton irradiation.

lector current shows a very small but observable change after high fluence proton irradiation. Similar behavior has been observed in proton irradiated SiGe HBTs, but no physical explanation has been given [59]. The base current, on the other hand, shows a different behavior. At the low V_{BE} region (0.7-0.9 V), the base current shows a slight decrease. As mentioned earlier, the accumulated charges in the passivation layer is the cause of this base current decrease. Moreover, the decrease of the leakage here is not as significant as in the lowest fluence proton irradiation, possibly due to the compensation of the proton-induced interface states which may cause more leakage current. At the higher V_{BE} region (≥ 0.92 V), the base current increases significantly. According to the analysis which will be discussed in the later

section, we believe that this excess irradiation-induced base current is due to the recombination in the base-emitter space charge region ($\Delta I_{B,SCR}$). Thus, the irradition damage in the base-emitter space charge region may be the main mechanism leading to the HBT current gain degradation in these devices. Moreover, because this induced recombination current dominates the base current in the lower bias region, the current gain degradation is expected to be more in the low base current region where $I_{B,SCR}$ dominates, consistant with the results presented in Fig 4.4 and 4.5. Finally, both of the post-irradiation I_C and I_B curves show less series resistance effects in the high V_{BE} region ($V_{BE} \geq 1.3$ V) than pre-irradiation values, indicating that the series resistance (R_E or R_B or both) decreases after proton irradiation. The magnitude of the resistance decrease varies a lot from device to device. This proton-induced resistance decrease is unusual and may be attributed to the radiation annealing of the contact materials by local heating. We will discuss this issue in more detail later in the modeling section.

4.4.1.3. Current Gain Dependence on Emitter Size

The proton-induced interface states may cause the increase of the surface recombination base current, while the proton-introduced bulk defects may cause the increase of the bulk recombination base current. Both of these currents may be responsible for the excess base current ($\Delta I_{B,SCR}$) discussed in the previous section. However, the III-V compound semiconductor HBTs are expected to be less sensitive to ionization effects (induced interface states), due to the high density of the interface states (as compared to Si/SiO_2 interface) already present in the unirradiated HBT devices. Thus, the displacement damage in the bulk SCR may be the dominant component of the excess base current in our devices.
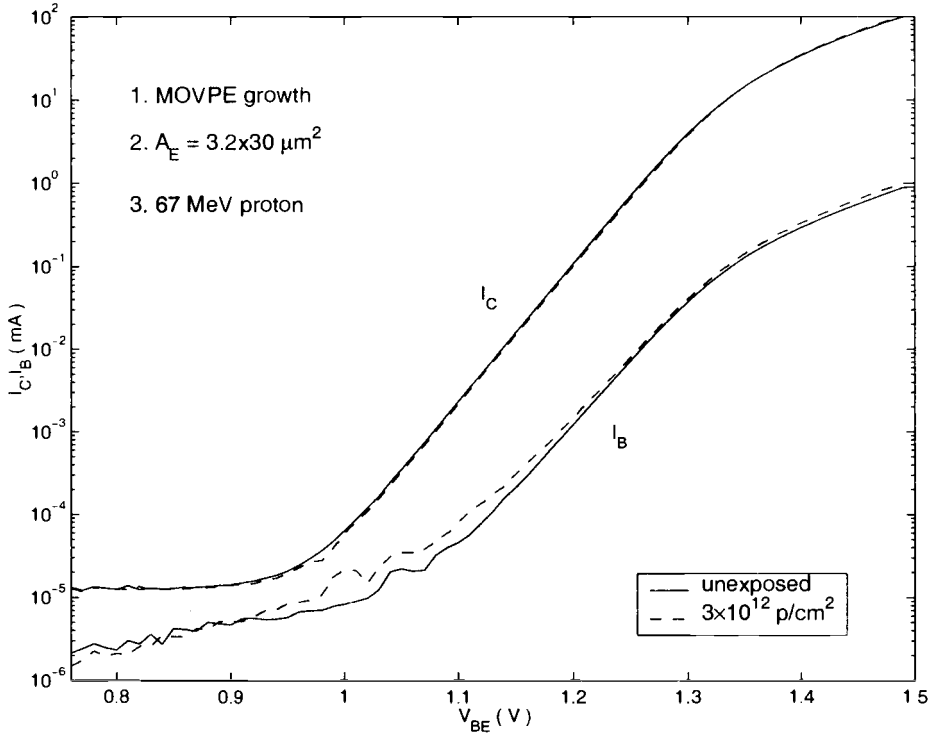
FIGURE 4.7. The forward Gummel plots before and after $3 \times 10^{12} p/cm^2$ proton irradiation.

The contribution of the surface and bulk components to the excess base current can be analyzed more quantitatively by correlating it to the emitter perimeter-to-area ratio (P/A). Fig 4.8 shows the current gain of the HBT devices with different emitter sizes (3.2×10, 3.2×14, and 3.2×30 μm^2) before and after proton irradiation at the same collector current density. The current gain of devices with larger emitter area (i.e. smaller P/A ratio) shows more degradation after proton irradiaiton. According to the results of forward Gummel measurement (Fig. 4.7), the collector current shows little change after proton irradiation, while the base current increases. Thus, the current gain after proton irradiation β can be written as

$$\beta = \frac{I_C}{I_{B0} + \Delta I_B} \tag{4.2}$$
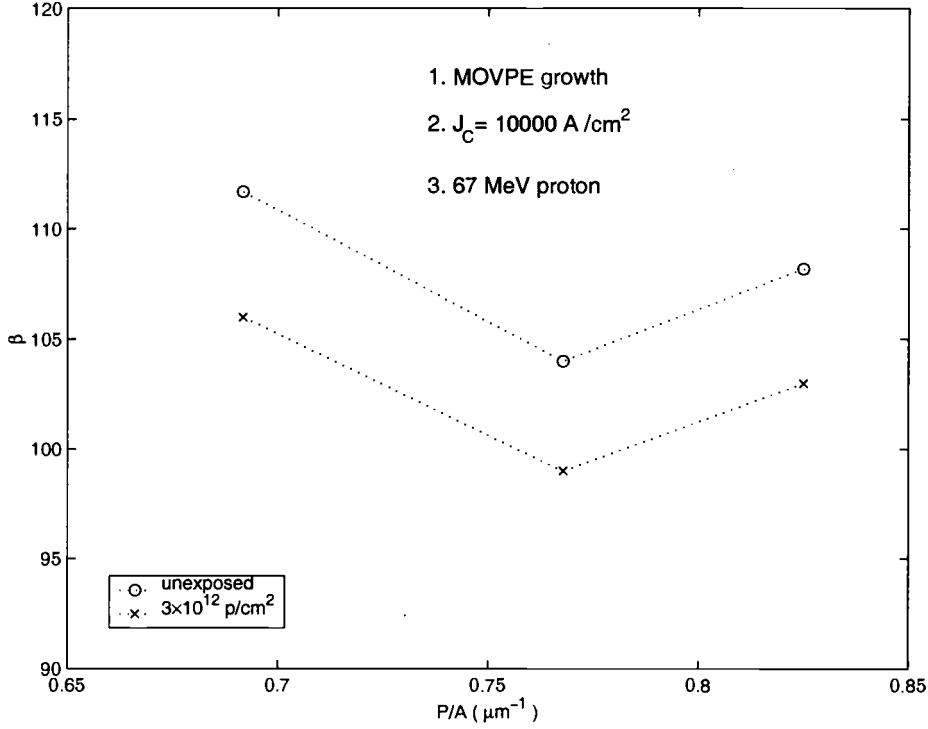
FIGURE 4.8. The current gain of the devices with different emitter sizes (3.2×10, 3.2×14, and $3.2 \times 30 \ \mu m^2$) before and after proton irradiation at the same collector current density.

where I_C is the collecter current, I_{B0} is the base current before irradiation, and ΔI_B is the proton induced base current. Equation 4.2 may be rewritten as

$$\frac{1}{\beta} = \frac{I_{B0} + \Delta I_B}{I_C} = \frac{1}{\beta_0} + \frac{\Delta I_B}{I_C} \qquad (4.3)$$

thus,

$$\frac{1}{\beta} - \frac{1}{\beta_0} = \frac{\Delta I_B}{I_C} = \frac{\Delta J_B}{J_C} \qquad (4.4)$$

where β_0 is the pre-irradiation current gain, J_C is the collector current density and ΔJ_B is the irradiation-induced extra base current density. As mentioned earlier, the excess base current (ΔI_B) can be attributed to bulk ($\Delta I_{B,b}$) and surface component ($\Delta I_{B,p}$). Thus, the excess base current density can be written as

$$\Delta J_B = \frac{\Delta I_B}{A} = \Delta J_{B,b0}(e^{qV/n_b KT} - 1) + \Delta J_{B,p0}(e^{qV/n_p KT} - 1) \times \frac{P}{A} \qquad (4.5)$$

where A is the emitter area, P is the emitter periphery, $J_{B,b0}(e^{qV/n_b KT} - 1)$ and $J_{B,p0}(e^{qV/n_p KT} - 1) \times \frac{P}{A}$ are the bulk and periphery current components, respectively. Thus, equation 4.4 can be rewritten as

$$(\frac{1}{\beta} - \frac{1}{\beta_0}) \times J_C = \Delta J_{B,b0}(e^{qV/n_b KT} - 1) + \Delta J_{B,p0}(e^{qV/n_p KT} - 1) \times \frac{P}{A} \qquad (4.6)$$

Since the ideality factors do not show significant change after proton irradiation, at a constant collector current, the dependence of the value of $(\frac{1}{\beta} - \frac{1}{\beta_0})$ on P/A may used as an indicator to the contribution of surface component. Thus, we can estimate which component is responsible for the excess base current and for the current gain degradation by plotting $1/\beta - 1/\beta_0$ as a function of P/A at a constant J_C.

Fig. 4.9 shows the measured $(1/\beta - 1/\beta_0)$ at a constant collector current density as a function of P/A. In Fig 4.9, $(1/\beta - 1/\beta_0)$ shows independent to P/A, indicating that the surface component is neglegible in the excess base current. Thus, a conclusion can be drawn that the bulk recombination in the base and emitter space charge region is the dominant damage mechanism for the current gain degradation after proton irradiation. This in turn indicates that the displacement damage is the most important factor in the radiation response of these devices. Finally, it needs to be mentioned that values of $\frac{1}{\beta} - \frac{1}{\beta_0}$ are almost constant for these devices indicating the damage coefficients (K_β) are almost the same for all devices with different emitter sizes. Therefore, the radiation effects in our HBT devices are not sensitive to the emitter size.
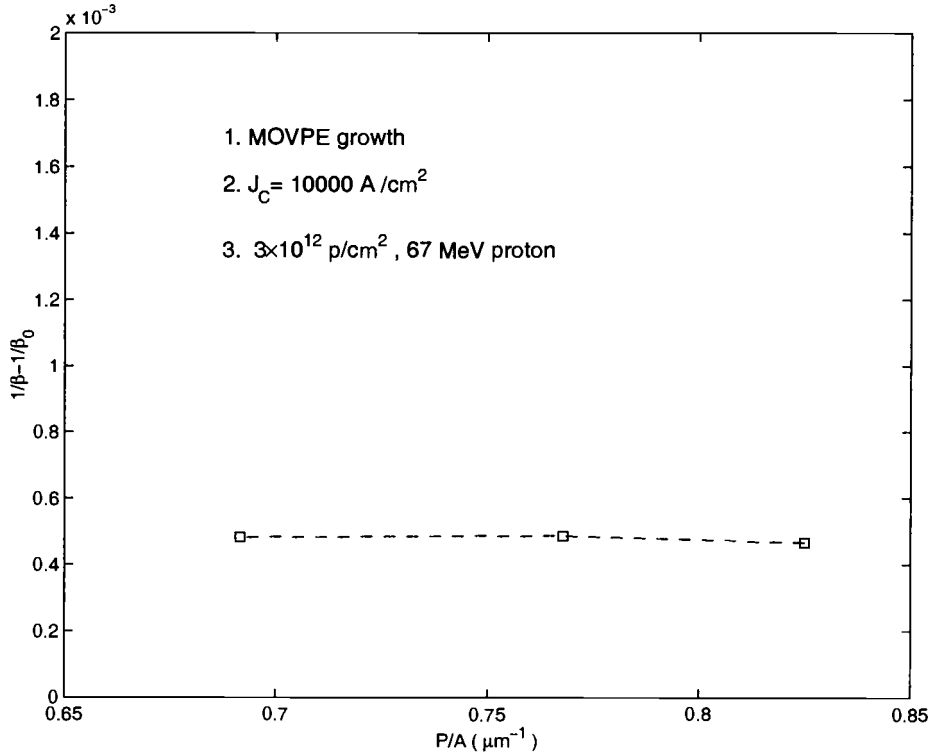
FIGURE 4.9. $\frac{1}{\beta} - \frac{1}{\beta_0}$ at the constant collector current density as a function of P/A.

4.4.1.4. Dependence of Proton Irradiation Effects on Semiconductor Growth Method

InGaP/GaAs epi layers are commonly grown by chemical vapor deposition (CVD) or metalorganic vapor phase epitaxy (MOVPE). The growth process usually plays an important role in the device performance as well as in the irradiation response. It is interesting to compare the pre-irradiation performance and radiation-induced dagradation of the devices with identical structures but grown by different growth processes. Two sets of InGaP/GaAs SHBTs with identical device structure and dimension, but grown by different growth methods (MOVPE and MBE) are tested in this study. Fig. 4.10a shows the current gain of the devices grown by

MOVPE or MBE with the same device structure and same size before and after
proton irradiation. Before proton irradiation, the devices grown by MOVPE show
superior current gain over the ones grown by MBE possibly due to the smaller base
recombination current in MOVPE devices. After $3 \times 10^{12} p/cm^2$ 67 MeV proton
irradiation, the current gains degrade by 8.1% and 6.7% for MOVPE and MBE
samples, respectively. The normailized damages (β/β_0) for both MOVPE and MBE
samples are ploted in Fig. 4.10b. Both MOVPE and MBE samples show similar
normalized damage.
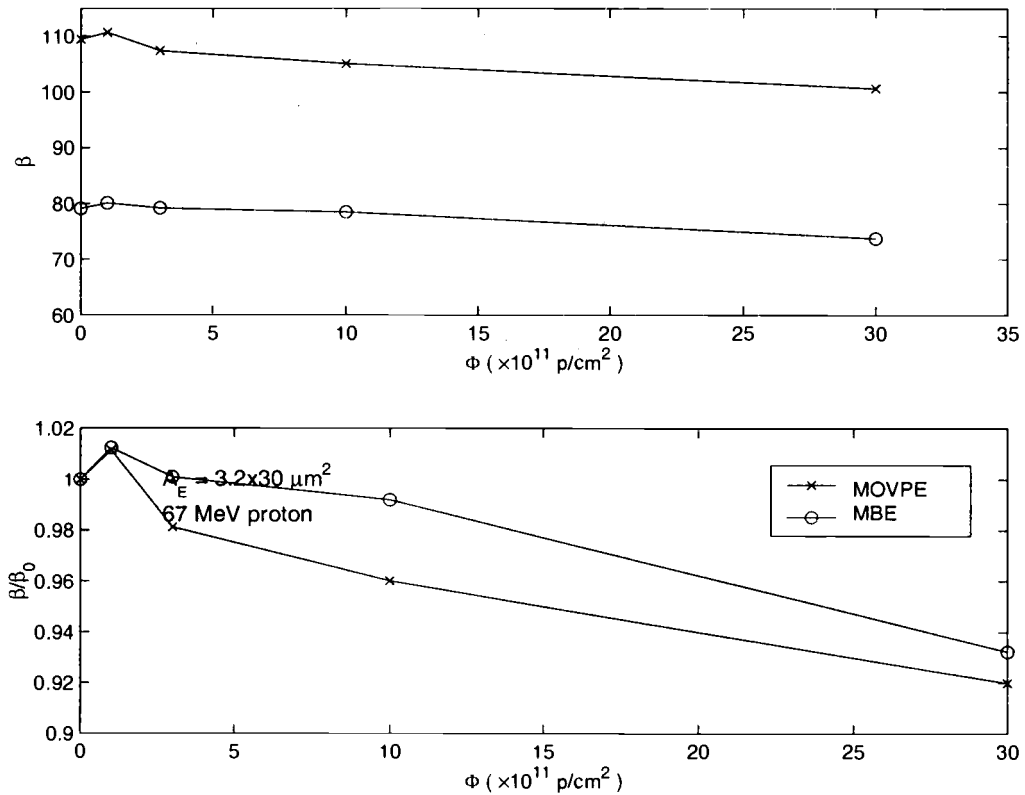
FIGURE 4.10. (a) The DC current gain and (b) the normalized damage (β/β_0)
as a function of proton fluence for MOVPE and MBE samples.

4.4.1.5. Dependence of Proton Irradiation Effects on Proton Energy

According the conclusion drawn from previous sections, the main degradation mechanism of the irradiated HBTs is the bulk defects caused by the atomic displacement. The number of defects introduced by particle irradiation depends on the NIEL of the incident particles. It is interesting to correlate the NIEL for the protons of different energies to the corresponding damage coefficent of HBT devices. The values of NIEL are about 3.7 and 3.5 KeV·cm^2/g for MeV 67 and 105 MeV proton, respectively (see Fig. 3.9). The NIEL of 105 MeV proton is 5.4% smaller than that of 67 MeV proton and thus a bit lower damage is expected for these devices irradiated by 105 MeV proton.

Both the MOVPE and MBE grown HBTs were subjected to 67 MeV and 105 MeV proton irradiation. Fig. 4.11 shows the current gain as a function of proton fluence for MOVPE samples after 67 MeV and 105 MeV proton irradiation. MOVPE samples show a little less gain degradation under 105 MeV proton irradiation. The damage coefficients are $2.74 \times 10^{-16} cm^2/p$ and $2.59 \times 10^{-16} cm^2/p$ for 67 MeV and 105 MeV proton irradiation, respectively. The degradation coefficient for 105 MeV proton irradiation is about 5.5 % lower than that for 67 MeV proton irradiation, showing the good correlation between NIEL and damage coefficient. Thus, the NIEL concept could be useful to predict the radiation damage of our MOVPE grown HBTS in the real radiation environment which may consist of protons with wide range of energy spectrum.

While the MOVPE grown samples show good agreement with NIEL, MBE grown HBTs show much less degradation in 105 MeV proton irradiation than that predicted by NIEL. Fig. 4.12 shows the current gain as a function of proton fluence for MBE samples after 67 MeV and 105 MeV proton irradiation. Unlike MOVPE samples, MBE devices show significantly less degradation under 105 MeV proton

irradiation. The damage coefficients for MBE devices are $3.49 \times 10^{-16} cm^2/p$ and $1.33 \times 10^{-16} cm^2/p$ for 67 MeV and 105 MeV proton irradiation, respectively. The damage coefficient for 105 MeV proton irradiation is about only 38 % of that for 67 MeV proton irradiation. The reason of the deviation in the correlation between NIEL and damage coefficient is not clear, and worth further study.
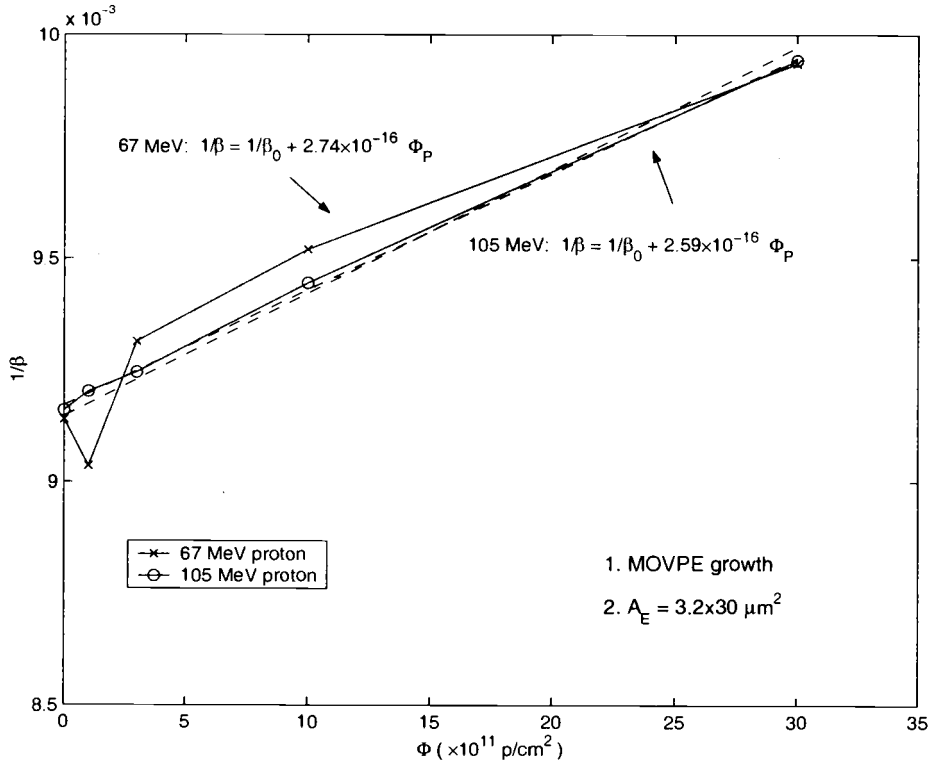
FIGURE 4.11. The DC current gain as a function of proton fluence for MOVPE samples after 67 MeV and 105 MeV proton irradiation.
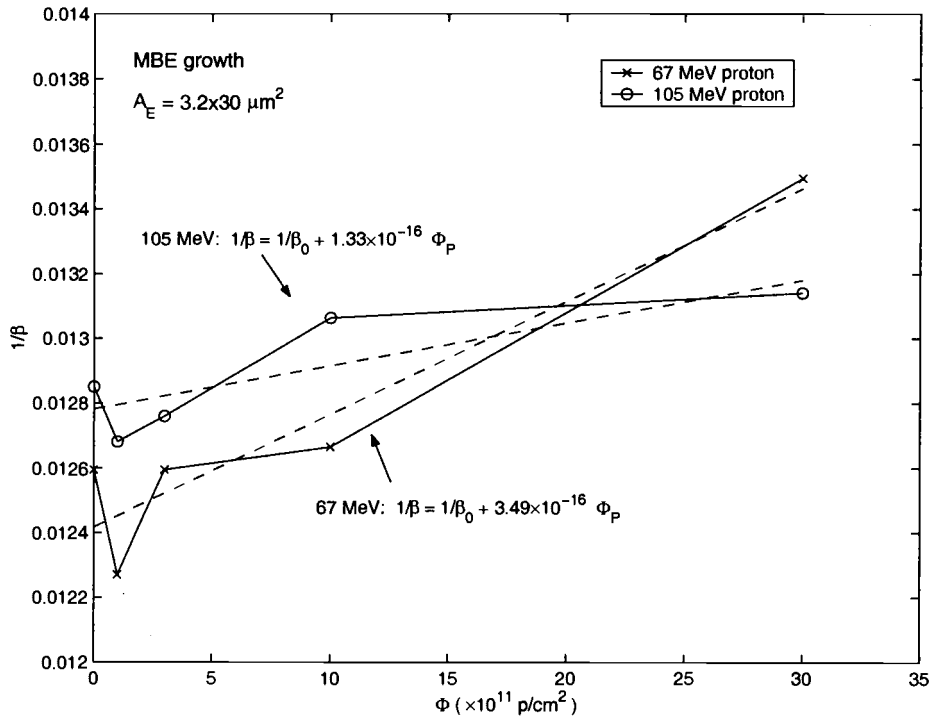
FIGURE 4.12. The DC current gain as a function of proton fluence for MBE samples after 67 MeV and 105 MeV proton irradiation.

4.4.2. Diode I-V Characteristics and Shift of Offset Voltage

The I-V characteristics of base-collector and base-emitter diodes of our HBTs were measured before and after proton irradiation. Fig. 4.13 and Fig. 4.14 show the pre- and post-irradiated I-V characteristic of the B-C and B-E diodes, respectively. The most significant change in these figures is the decrease of the series resistance (increase in the current for $V \geq 1.2$ V) which is consistant with the results of Gummel plots. However, the magnitude of the resistance decrease varies a lot from device to device. The magnitude of the decrease in the individual series resistances (R_E, R_C and R_B) can be estimated by employing the parameter extraction method discussed in Chapter 2. The results (see Table 4.1) show the base series resistance decreased

significantly while the emitter resistance and collecter resistance show little change after irradiation. The cause for this resistance decrease may possibly be attributed to the irradiation-induced annealing of contact materials by local heating. Further investigation in this effect is needed.
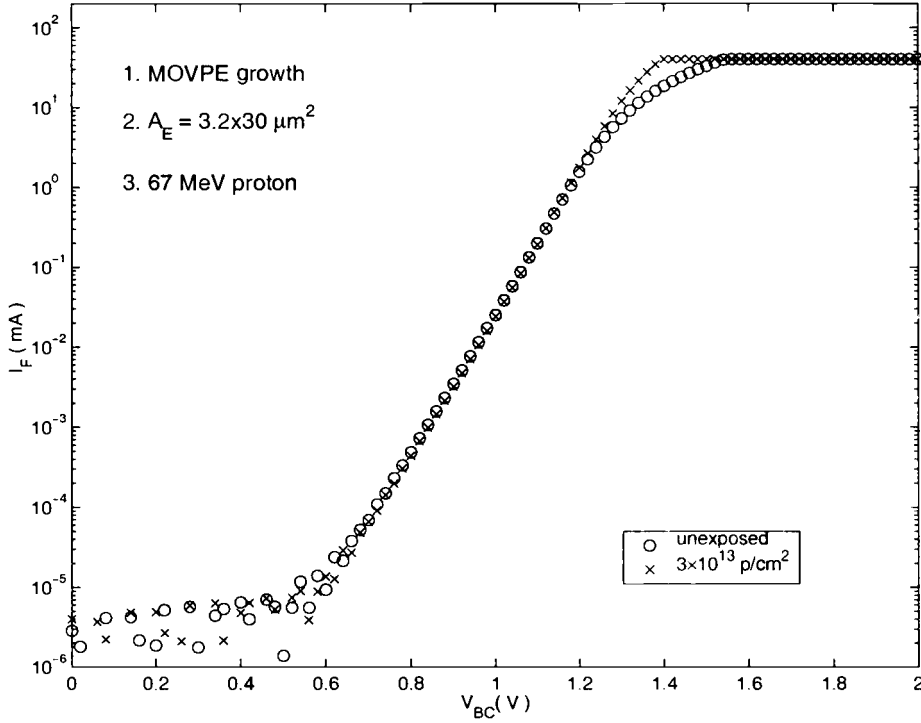
FIGURE 4.13. I-V characteristics of base-collector diode before and after proton irradiation.

In general, the irradiation induced offset voltage shift in the I_C-V_{CE} characteristics is mainly attributed to the irradiation-induced knee voltage shift (or equivalently increase saturation current) of the B-C diode. Fig. 4.13 shows almost no shift in the saturation current of the B-C junctions, consistant with the absence of the proton-induced offset voltage shift in $I_C - V_{CE}$ characteristics (see Fig. 4.3).
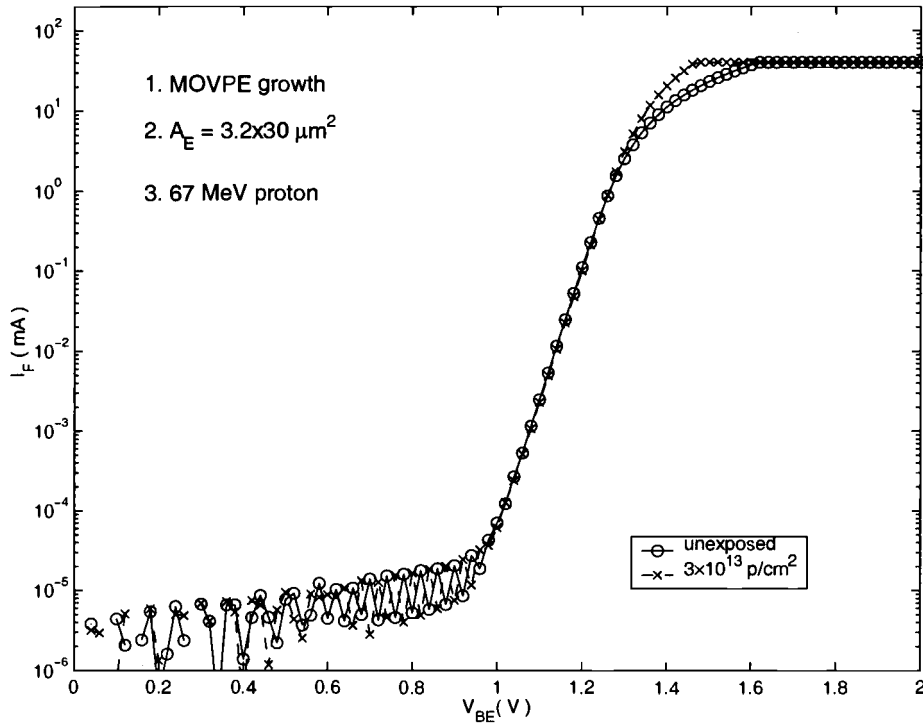
FIGURE 4.14. I-V characteristics of base-emitter diode before and after proton irradiation.

4.4.3. Degradation of Breakdown Voltage

According to previous work in our group, radiation-induced breakdown voltage degradation and increase of output conductance in the active regime were also observed in the unpassivated HBTs [67, 68]. The increase of output conductance after irradiation has been attributed to the avalanche multiplication in the base-collector region, which is due to the breakdown voltage degradation after irradiation. The base width modulation effect is negligible due to the heavily doped base in HBTs. However, previous study shows that the output conductance in the active regime is not very sensitive to the irradiation for the polyimide passivated devices. HBTs employed in this study are also polyimide passivated, thus the output con-

ductance is not expected to be sensitive to proton irradiation (see Fig. 4.2). As expected, the values of common-base breakdown voltage (BV_{CBO}) are about the same (~ 16 V) before and after proton irradiation. The breakdown voltage shows very little degradation even after the highest proton irradiation fluence which is consistant with insensitivity of output conductance in the active regime, suggesting that proton-induced traps in the base and collect regions do not play a significant role in the output conductance effect in these devices.

4.5. Parameter Extraction and Simulation

The proton induced degradation may be analyzed more quantitatively by employing the parameter extraction process and HBT model discussed previously. The degradation characteristics can be revealed by comparing the extracted parameters before and after proton irradiation. The extraction procedures and EM model employed here are similar to those discussed in Chapter 2 (see Fig. 2.9).

4.5.1. Parameter Extraction

First, in the forward Gummel plot (Fig.4.15), the base leakage current ($I_{B,belk}$) and the collector leakage current ($I_{B,lk}$) may be determined in the lower V_{BE} region ($V_{BE} \leq 0.85$ V). The base leakage components from BE junction ($I_{B,belk}$) before and after proton irradiation are about 3.0 and 1.5 nA. The collector leakage components ($I_{C,lk}$) before and after proton irradiation are about 12.6 and 12.5 nA. The base leakage component ($I_{B,belk}$) decreases by a factor of 2, whereas collector leakage component ($I_{C,lk}$) remains the same after proton irradiation. The suppression of the base leakage component ($I_{B,belk}$) is attributed to the accumula-

tion layer in the base region caused by radiation-induced trapped charges, leading to the reduction of the surface recombination.

FIGURE 4.15. The measured (solid lines) and the simulated (dashed lines) forward Gummel plots for HBT (a) before proton irradiation and (b) after proton irradiation

As V_{BE} is increased (0.95 V $\leq V_{BE} \leq 1.15$ V), the collector and base currents are still sufficiently small, so that the voltage drop across R_E and R_B may be neglected. We can extract the ideality factor m from the slope of the $\log(I_C\text{-}I_{C,lk})$ - V_{BE} curve. The prefactor I_{C0} then can be determined from the extrapolation of the linear region of $\log(I_C\text{-}I_{C,lk})$ - V_{BE} plot to $V_{BE} = 0$ axis. The ideality factors, m, and the prefactors, I_{C0}, are 1.03 and 4.2×10^{-24} A for the pre-irradiated devices and

1.02 and 2.0×10^{-24} A for the post-irradiated devices. While the ideality factor m is almost the same, the prefactor I_{C0} decreases slightly after proton irradiation consistant with the collector current decrease in the Gummel plot after irradiation (see Fig 4.7). Similarly, the space-charge recombination component ($I_{B,be1}$) dominates the base current in the low V_{BE}. Thus, the ideality factor n and prefactor $I_{B,be10}$ can be determined from the slope and the intercept of the $\log(I_B - I_{B,belk})$ - V_{BE} curve in the region of low V_{BE} in the measured Gummel plot. The ideality factors, n, and the prefactors, $I_{B,be10}$, are 2.40 and 4.6×10^{-16} A for the pre-irradiated devices ,and 2.44 and 1.8×10^{-15} A for the post-irradiated devices, respectively. The prefactors $I_{B,be10}$ increases quite significantly, by a factor of 4, after proton irradiation, indicating that the radiation damage, which may introduce more recombination centers, occurs in the space-charge region of the BE junction.

By using the already extracted parameters, $I_{B,belk}$, m, n and $I_{B,be10}$, the value of $I_{B,be20}$ is easily determined by fitting the $\log(I_C)$ - V_{BE} curve in the intermediate V_{BE} region (1.25V $\leq V_{BE} \leq$ 1.30V) where the series resistance effects are still negligible. The prefactors, $I_{B,be20}$, are 4.0×10^{-26} A and 2.2×10^{-26} A for pre- and post-irradiated devices, respectively. Finally, the series resistance may be determined by fitting I-V curves in high V_{BE} region in the forward Gummel plot. The emitter series resistances, R_E, are 1.35 and 1.3 Ω for both of pre- and post-irradiated devices, indicating the emitter series resistance is not affected by proton irradiation.

In inverse Gummel plots (Fig. 4.16), similar extraction precedures could be employed to obtain the parameters for BC junction, such as $I_{B,bclk}$, $I_{E,lk}$, m', n' , $I_{B,bc10}$, $I_{B,bc20}$, I_{E0} and $R_C + R_B$. I_{E0} decreased from 7.0×10^{-23} A to 5.5×10^{-24} A after proton irradiation. This decrease of I_{E0} may be attributed to the radiation-induced carrier removal effect in the emitter region, leading to the thicker barrier in the BE heterojunction conduction band for the thermoionic emission electrons.
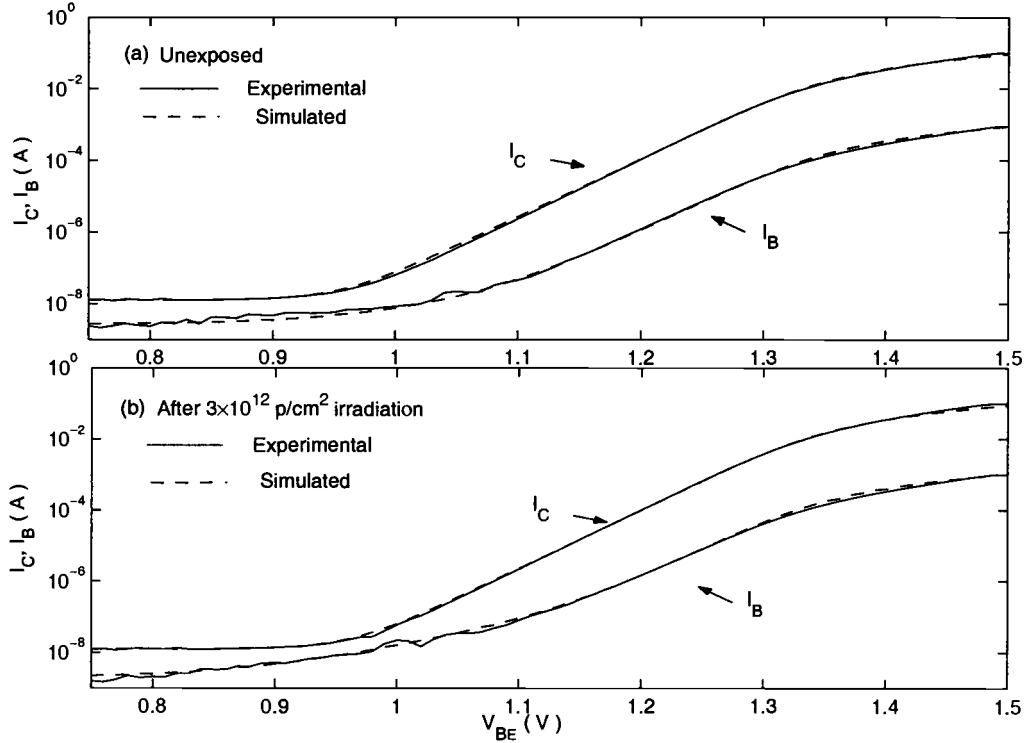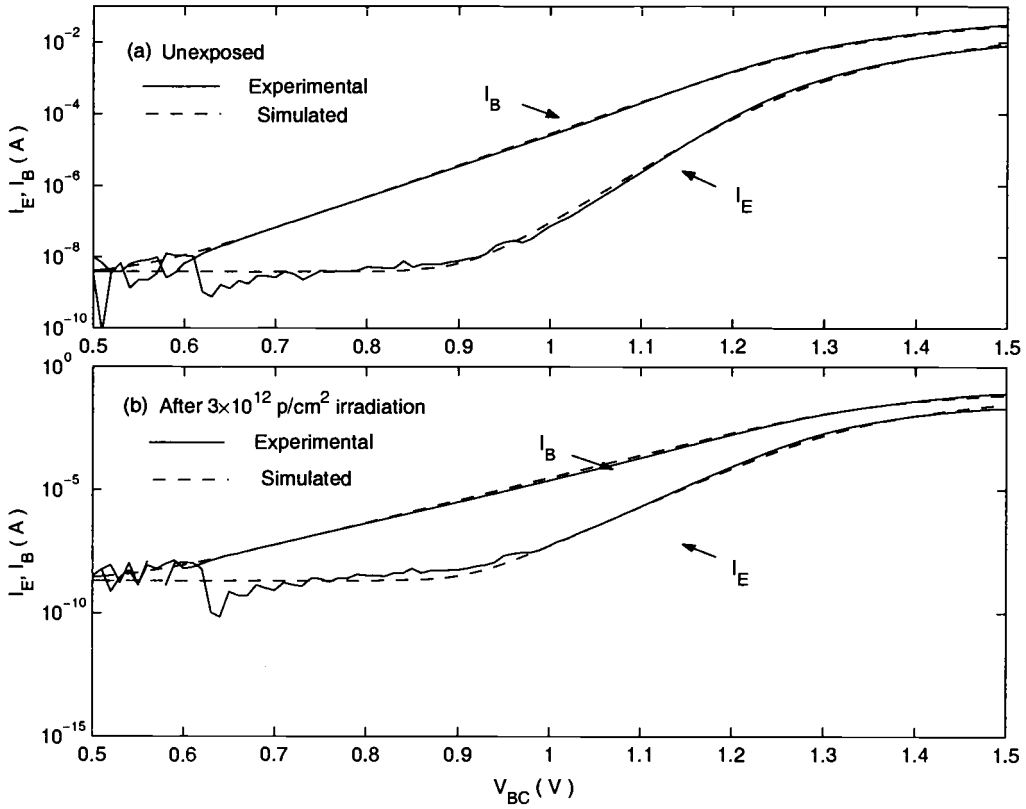
FIGURE 4.16. The measured (solid lines) and the simulated (dashed lines) inverse Gummel plots for HBT (a) before proton irradiation and (b) after proton irradiation

Moreover, this decrease of I_{E0} leads to the decreases of $I_{B,be20}$ and I_{C0} previously analyzed in the forward Gummel plot. Thus, we may conclude that the radiation-induced displacement damage in the emitter region, which leads to the radiation-induced carrier removal effect, is the responsible mechanism for the decreases of I_{C0}, I_{E0} and $I_{B,be20}$. The extracted parameters are shown in Table 4.1. In the BE diode characteristics measurement, the value of $R_E + R_B$ can be estimated by fitting the I-V curve under the large forward bias region. Since the value of R_E has been determined in the forward Gummel plot, the value of R_B can then easily be estimated. The value of R_C can further be determined from the extracted value of

$R_C + R_B$ in the inverse Gummel plot. The values of R_C are both 1.35 Ω for the pre- and post-irradiated devices, while R_B decreases from 5.6 to 1.5 Ω after proton irradiation. Thus, R_B is more sensitive to the proton radiation for our HBTs.

The slope of I_C - V_{CE} curves in the forward active region may be fitted by introducing avalanche multiplication factor, M. Thus, the collector current may be written as

$$I_{C,avalanche} = M \times I_C \qquad (4.7)$$

where I_C is the collector current without multiplication. The avalanche multiplication factor (M) is voltage dependent, and can be expressed as

$$M = \frac{1}{[1 - (\frac{V_{CB}}{BV_{CBO}})^r]} \qquad (4.8)$$

where BV_{CBO} is the breakdown voltage of the common-base breakdown voltage, and r is an empirical constant. The value of BV_{CBO} can be directly measured through common-base breakdown voltage measurement. The empirical constant, r, then can be estimated by fitting the slope of the experimental I_C - V_{CE} curve in the active region. As expected, both of common-base breakdown voltage (BV_{CBO}) and empirical constant (r) are about the same before and after proton irradiation, suggesting that proton-induced traps in the base and collect regions do not play a significant role in the output conductance effect in the polyimide passivated devices.

4.5.2. Simulation of $I_C - V_{CE}$ Characteristics

In this section, we show how the extracted parameters are employed to model the $I_C - V_{CE}$ characteristics. In the I_C - V_{CE} measurement, I_C is measured as function of the V_{CE} with a constant base current. In order to calculate the collector current, the individual potential drop across the BE and BC junction for a fixed

TABLE 4.1. A set of extracted parameters for MOVPE grown HBTs before and after proton irradiation.

Parameter	unexposed	$3.0 \times 10^{12}\ p/cm^2$
I_{C0} (A)	4.2×10^{-24}	2.0×10^{-24}
$I_{C,lk}$ (A)	1.26×10^{-8}	1.25×10^{-8}
$I_{B,be10}$ (A)	4.6×10^{-16}	1.8×10^{-15}
$I_{B,be20}$ (A)	4.0×10^{-26}	2.2×10^{-26}
$I_{B,bc10}$ (A)	4.2×10^{-14}	2.2×10^{-14}
$I_{B,bc20}$ (A)	~ 0	~ 0
$I_{B,belk}$ (A)	3.0×10^{-9}	1.5×10^{-9}
$I_{B,bclk}$ (A)	2.0×10^{-9}	2.0×10^{-9}
I_{E0} (A)	7.0×10^{-23}	5.5×10^{-24}
$I_{E,lk}$ (A)	4.0×10^{-9}	2.0×10^{-9}
m	1.03	1.02
n	2.40	2.44
m'	1.11	1.05
n'	1.89	1.83
R_C (Ω)	1.35	1.35
R_E (Ω)	1.35	1.3
R_B (Ω)	5.6	1.5
V_{BR} (V)	16	16
r	1.4	1.4

V_{CE} needs to be calculated. By using developed extended Ebers-Moll model and the approach explained in Chapter 2, the I_C - V_{CE} characteristics may be simulated by using a simple program, such as MATLAB.
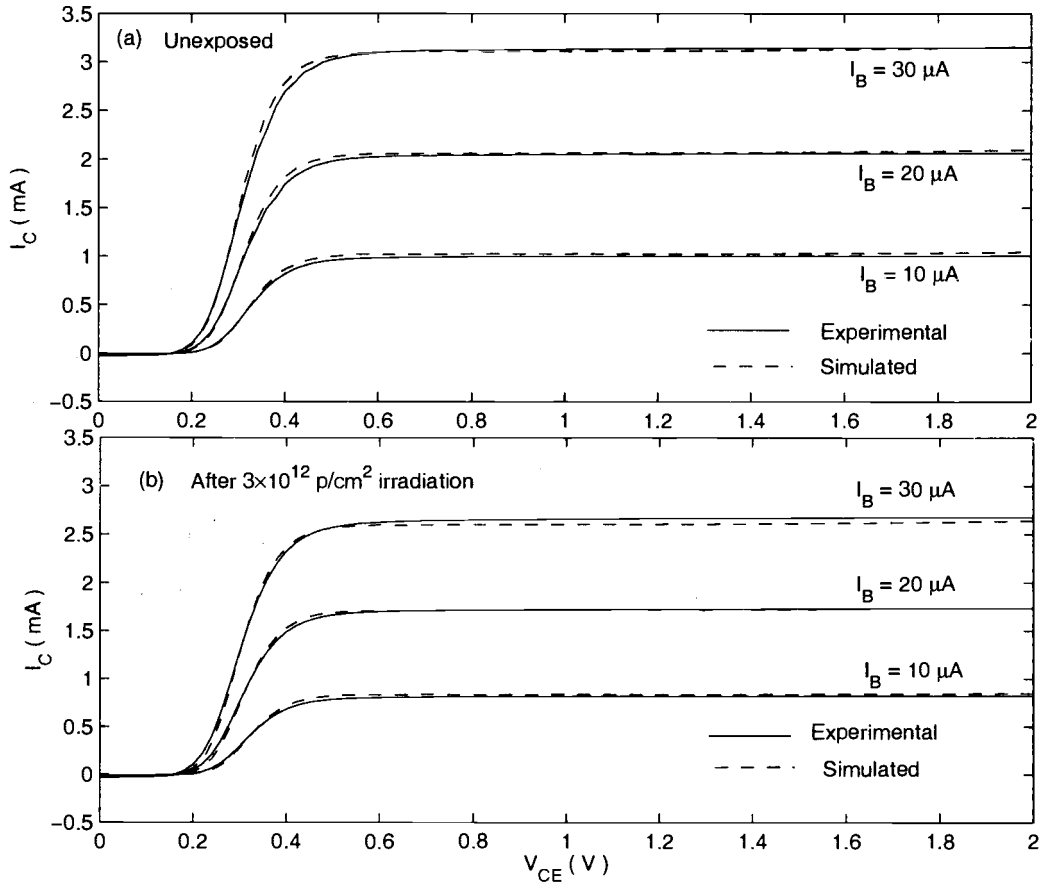
FIGURE 4.17. The measured (solid lines) and the simulated (dashed lines) I_C - V_{CE} characteristics at three different base currents for HBT (a) before proton irradiation and (b) after proton irradiation

The simulated I_C - V_{CE} plots for the HBT before and after irradiation are shown in Fig 4.17. By using the same approach, the forward and inverse Gummel plots are also simulated and shown in Fig. 4.15 and Fig 4.16, respectively. Excellent

agreement between the experimental and simulated curves is seen for both of the unexposed and irradiated HBT, indicating that the proposed extended Ebers-Moll model is sufficient not only to the normal HBT behaviors but also to the radiation degraded HBT behaviors.

4.6. Conclusion

This study has examined various aspects of radiation damage in InGaP/GaAs HBTs. Overall, the studied HBT devices are quite robust against high energy proton irradiation. These InGaP/GaAs HBTs are not sensitive to the radiation-induced offset voltage shift. Gain degradation is the main manifestation of the proton irradiation response of HBTs studied. The displacement damage in the bulk of base-emitter space-charge region, leading to the excess base current, is the responsible mechanism for the proton induced gain degradation. The radiation damage depends on operation current and is generally less at higher currents. Compared to the MBE grown devices, the MOVPE grown HBTs show superior characteristics both in initial performance and in proton irradiation hardness. The 67 MeV protons may do more damage than 105 MeV protons, due to their higher value of NIEL. Moreover, the MOVPE samples show good correlation between NIEL and damage coefficient, while MBE samples show some deviation from the correlation. The HBT I-V characteristcs of pre- and post-irradiation samples can be simulated successfully by employing the developed model and provide an insight into the proton irradiation effects in our HBTs.

5. NEUTRON IRRADIATION EFFECTS IN GALLIUM NITRIDE HETEROJUNCTION LEDS

5.1. Introduction

Gallium nitride (GaN) is a direct wide band gap III-V compound semiconductor that is a promising material for opto-electronic devices in the blue to UV range as well as for high power, high speed electronic devices. A gallium nitride based metal-insulator-semiconductor light emitter diode was first reported by Pankov in 1971 [69]. However, very few GaN commercial devices were made since then due to several material difficulties (lack of a convenient substrate for epitaxial growth and the difficulty of p-type doping), until a breakthrough came in 1994. Nakamura *et al.* in Nichia successfully developed GaN based double heterojunction (DH) blue light emitting diodes (LEDs) which could increase the optical storage density and are essential for full color display technologies [70]. As a result, tremendous efforts have been put into the development of GaN based devices in recent years.

It has been reported that GaN is two orders of magnitude less sensitive to proton irradiation as compared to GaAs [71]. However, limited work has been done on the proton irradiation effects in GaN devices [73] and no work, to our knowledge, has been done on neutron irradiation effects in GaN based LEDs. It is known that neutrons may cause more displacement damage than protons. Thus, it is of great interest to investigate the response of GaN based blue LEDs under neutron irradiation.
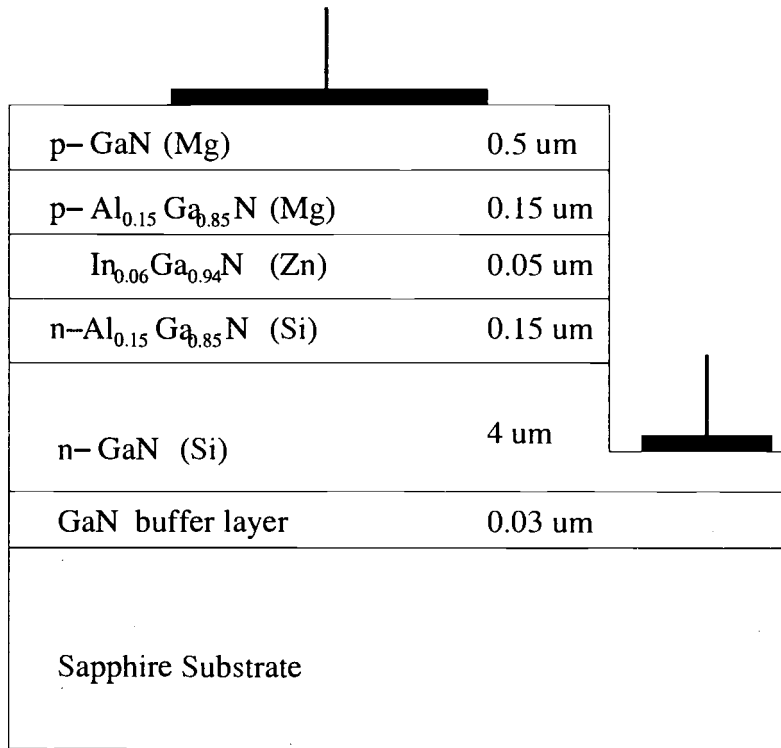
In this chapter, the neutron irradiation effects in GaN based double heterojunction (DH) LEDs from Nichia are investigated. First, the device structure and experimental details of neutron irradiation and characterization will be given. The

effects of neutron irradiation on the optical and electrical characteristics of GaN LEDs will be subsequently presented. The basic mechanisms of the radiation effects are also discussed. The current-enhanced annealing of irradiated LEDs will then be discussed. A conclusion will be given at the end of this chapter.

5.2. Device structure and experimental detail

The devices used in this study are Nichia GaN blue LEDs type NO. NSPB510ST. These LEDs are double heterostructures (DHs) with the n-type In-GaN active layer codoped with Si and Zn. The schematic cross section and epilayer sequence of the LED structure is shown in Fig 5.1.

All devices were optically and electrically characterized before neutron irradiation. Each set of samples (three LEDs) were shorted and encapsulated into a polyethylene vial which was placed inside a cadmium box. The boxes were positioned into the Rotating Rack (Lazy Susan) of the OSU TRIGA "MarkII" 1MW reactor. The samples were irradiated individually for 20 and 50 minutes at 100kW, and for 5, 15, 45, 120 minutes at 1MW. The calculated total neutron fluence (excluding thermal neutrons) are listed in Table 5.2. The samples were characterized after the samples cooled down, until their radioactivety had reached the acceptable safety limits. All devices were characterized again after irradiation. Electrical characterization was conducted by using a HP 4145B parameter analyzer. The measurement setup is similar to the one discussed in Chapter 2. Optical characterization was performed by using an Ocean Optics Inc. Fiber Optic spectrometer.

p– GaN (Mg)	0.5 um
p– Al$_{0.15}$ Ga$_{0.85}$N (Mg)	0.15 um
In$_{0.06}$Ga$_{0.94}$N (Zn)	0.05 um
n–Al$_{0.15}$ Ga$_{0.85}$N (Si)	0.15 um
n– GaN (Si)	4 um
GaN buffer layer	0.03 um
Sapphire Substrate	

FIGURE 5.1. Schematic cross section of the epilayer sequence of the InGaN DH LED.

5.3. GaN LED fundamentals

Although the InGaN based LEDs have been mass produced and commercialized, the mechanisms of the current transportation and light emission are still not very clear. The band diagram of GaN based blue LED is shown in Fig. 5.2. The current-voltage (I-V) characteristics of GaN based diodes may be expressed as a conventional equation

$$I = I_0 exp(qV/nkT) \qquad (5.1)$$

Sample	Reactor power	t (min)	Φ^{total} (n/cm^2)
1	100kW	20	7.2×10^{13}
2	100kW	50	1.8×10^{14}
3	1MW	5	1.8×10^{14}
4	1MW	15	5.4×10^{14}
5	1MW	45	1.6×10^{15}
6	1MW	120	4.3×10^{15}

TABLE 5.1. Neutron irradiation duration, and the corresponding total neutron fluence.

However, the ideality factor n is usually larger than 2, and the slope of $log(I) - V$ curves is quite insensitive to temperature. Thus, the current-voltage characteristics of GaN based diodes may be better expressed as

$$I = I_0 exp(\alpha V) \tag{5.2}$$

where I_0 is a constant, V is the bias voltage, and α may vary from 5.7 to 15 V^{-1}. Previous studies show tunneling is a dominant mechanism for the current transport in GaN LEDs [77, 78], due to the large ideality factor (from 3 to 6) and the almost temperature independent slope of the I-V curves. Also, the large band gap of GaN makes the diffusion mechanism not feasible. For example, the usual diffusion current for injecting holes into an n-type semiconductor can be given as [77]

$$I_P = \frac{q D_P n_i^2 A}{L_P N_d^+} [exp(qV/nkT) - 1] \tag{5.3}$$

where D_P is the hole diffusivity, n_i is the intrinsic carrier concentration, L_P is the diffusion length, and N_d^+ is the ionized donor concentration. For GaN at room

temperature, the value of n_i^2 is about 4×10^{-20} cm^{-6}. As a result, under normal bias condition, the diffusion current becomes very small, and the tunneling current dominates. The tunneling current across the interface of a heterojunction may be described as [78]

$$I_F = BN_T exp[\frac{4}{3\hbar}(\frac{m^*\epsilon}{N})^{1/2}V]$$
(5.4)

where **B** is a constant, N_T is the density of the traps in the forbidden gap at the interface or in the space charge region that provides the tunneling path, m^* is the carrier effective mass, ϵ is the electrical permitivity, and N is the doping concentration of the higher band gap material in the heterojunction.

Most tunneling carriers (electrons and holes) are captured and confined inside the quantum well and recombined. As a result, a very high quantum efficiency is achieved.
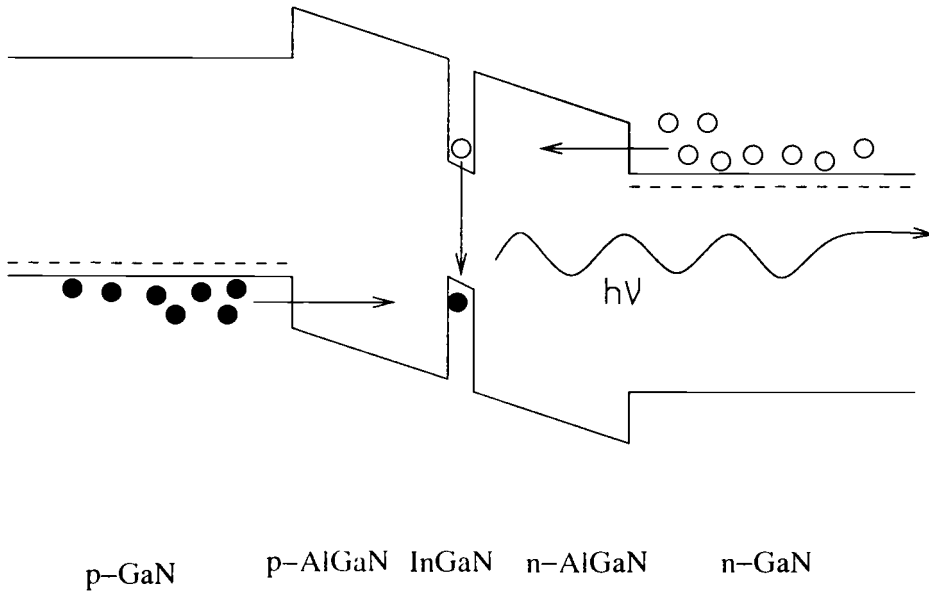

p-GaN   p-AlGaN InGaN n-AlGaN   n-GaN

FIGURE 5.2. Band diagram of GaN based blue LED

However, similar to electrical properties, the nature of the radiative transitions producing the emission in InGaN has been controversial. Nakamura *et al.* have suggested that recombination in InGaN multiple quantum well systems could occur in In-rich regions acting as quantum dots [74], while other groups have attributed the emission to the recombination of excitons localized either by In compositional fluctuations or at the band tail states [75, 76]. From the measurements of the photoluminescence (PL) decay lifetime in InGaN, and the pressure dependence of the photoluminascence and electroluminescence (EL), it has been suggested that alloy fluctuations and impurity states are the most likely candidates responsible for the emission mechanism. Moreover, the emission peak shows blue shift as injection current increases (see Fig. 5.3). In our measurement, the emission maximum shifts from 472 nm to 459.5 nm as injection current ramps up from 0.15 mA to 130 mA. This blue shift has been attributed to the band filling mechanism, which results from injected holes filling the empty acceptor states and valence band tails in the active layer [77].

5.4. Neutron irradiation effects in GaN LEDs

As compared with other III-V compound semiconductor devices, the main concern in the case of GaN LEDs is the radiation-induced atomic displacement. The energetic neutron may displace both Ga and N atoms from their lattice positions, and hence introduce the vacancy sites (V_N and V_{Ga}) and interstitials (N_I and Ga_I). These defects may introduce new trap states in the band gap. According to the first-principles total energy calculations, V_N has been reported to be a single, shallow donor, N_I is a single, deep acceptor at 1 eV above valence band, V_{Ga} is a triple acceptor and Ga_I is a single donor [79]. Both the electrical and optical properties of GaN LEDs may be affected by these neutron induced states.
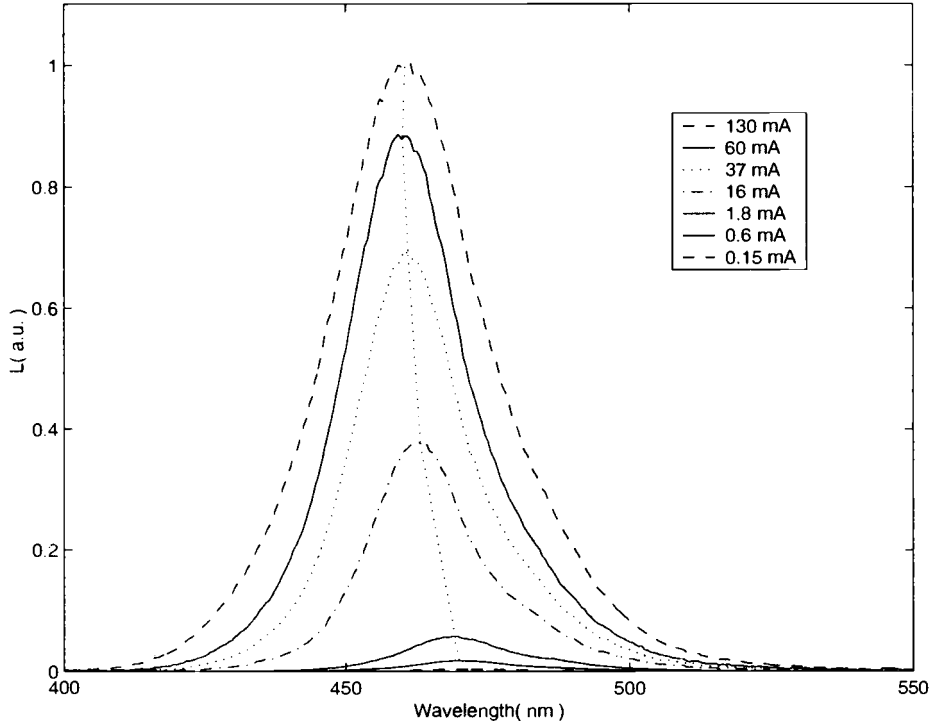
FIGURE 5.3. The emission spectra of GaN LEDs under different injection current.

5.4.1. Neutron effects on electrical properties

The I-V characteristics of the GaN LEDs before and after neutron irradiation are shown in Fig. 5.4. The most significant irradiation effects are the decreasing slope of curves (or decreasing α value in eq. 5.2) and increasing I_0. After the highest fluence neutron irradiation, devices show dramatic degradation in the I-V characteristics.

The extracted parameters, α and I_0, are plotted in Fig. 5.6 and Fig. 5.5 as a function of neutron fluence. The slope (α) decreases with increasing neutron fluence, while I_0 increases steadily with neutron fluence. According to eq. 5.4, α is a function of the doping concentration, N, while the magnitude of I_0 depends on the
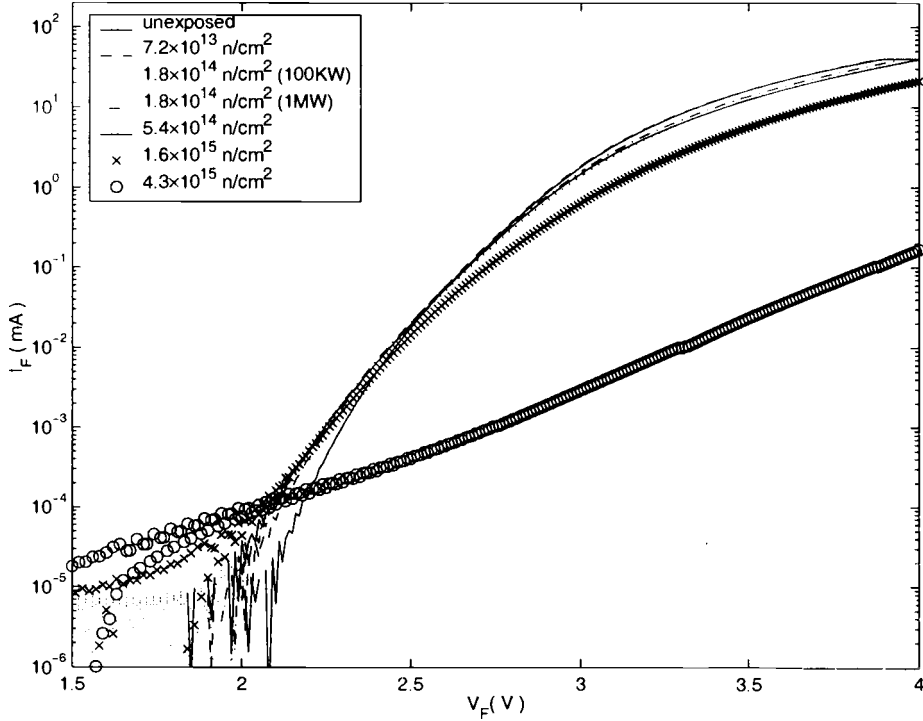
FIGURE 5.4. I-V characteristics of the GaN LEDs before and after neutron irradiation.

trap concentration, N_T. The decreasing α value after irradiation may be attributed to the neutron irradiation induced carrier removal effect, leading to a thicker barrier for tunneling. On the other hand, the increasing value of I_0 after irradiation may be attributed to the increasing trap concentration, N_T, after irradiation, indicating neutron irradiation introduces the trap states inside the band gap.

The degradation of I_0 may be used as a radiation damage indicator for these devices. According to equation 5.4, the extracted parameter, I_0, may be expressed as

$$I_{0,rad} = BN_T = B \times [N_{T0} + N_{TI}] \tag{5.5}$$

or
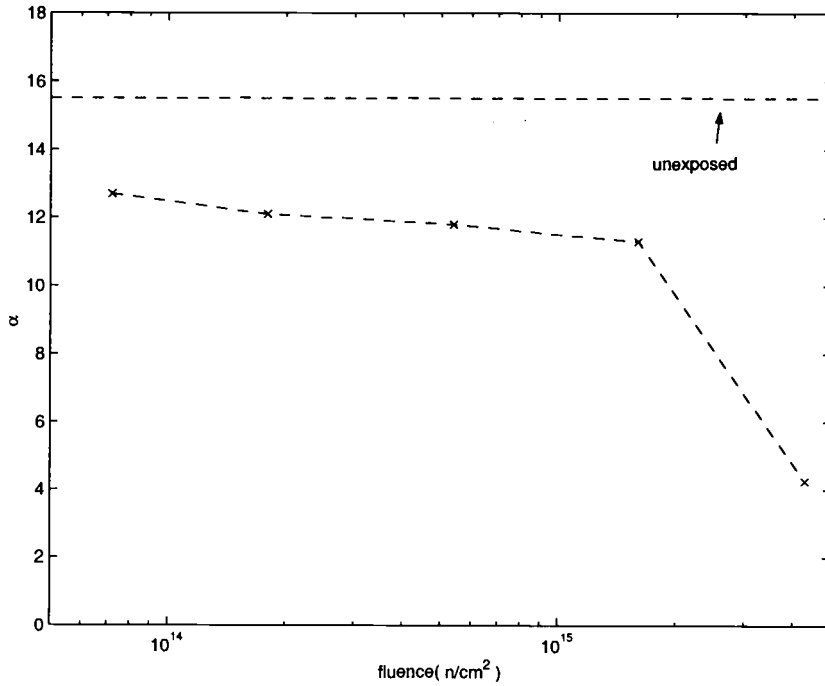
FIGURE 5.5. Extracted parameters, α, as a function of neutron fluence.

$$I_{0,rad} = I_{0,pre} + B \times N_{TI} \tag{5.6}$$

where $I_{0,rad}$ is the extracted I_0 after irradiation, $I_{0,pre}$ is the extracted I_0 before irradiation, N_{T0} is the density of the traps before irradiation, N_{TI} is the density of the traps introduced by irradiation. Moreover, N_{TI} may be written as

$$N_{TI} = C_T \times \Phi_n \tag{5.7}$$

where C_T is a constant and Φ_n is the neutron irradiation fluence. Thus, eq. 5.6 may be expressed as

$$I_{0,rad} = I_{0,pre} + B \times C_T \times \Phi = I_{0,pre} + K_{I_0} \times \Phi_n \tag{5.8}$$

where K_{I_0} is the damage coefficient for I_0 and may be extracted from the slope in $I_{0,rad} - \Phi_n$ plot. Fig. 5.7 shows $I_{0,rad}$ as a function of radiation fluence, Φ_n. The damage coefficient, K_{I_0}, is about 5.66×10^{-33} Acm^2/n for our LEDs.
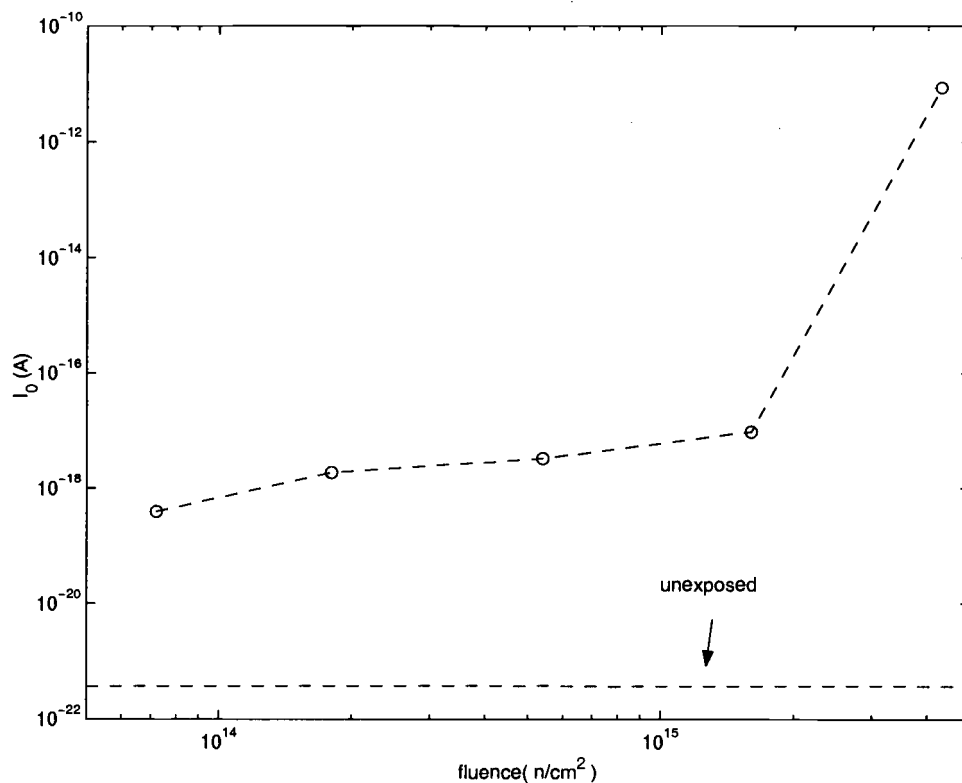
FIGURE 5.6. Extracted parameters, I_0, as a function of neutron fluence.

5.4.2. Neutron effects on optical properties

Fig 5.8 shows the emission spectra of GaN LEDs at a constant injection current before and after neutron irradiation. The curves have been normalized to the peak intensity of pre-irradiated samples. The spectrum consists of a strong blue emission band at 467 nm. The spectra show neither significant wavelength shift nor new emission peak after neutron irradiation. However, the overall intensity of emission decreases significantly with increasing neutron fluence, suggesting that the neutron-induced defects introduce nonradiative recombination centers in the active InGaN layer.
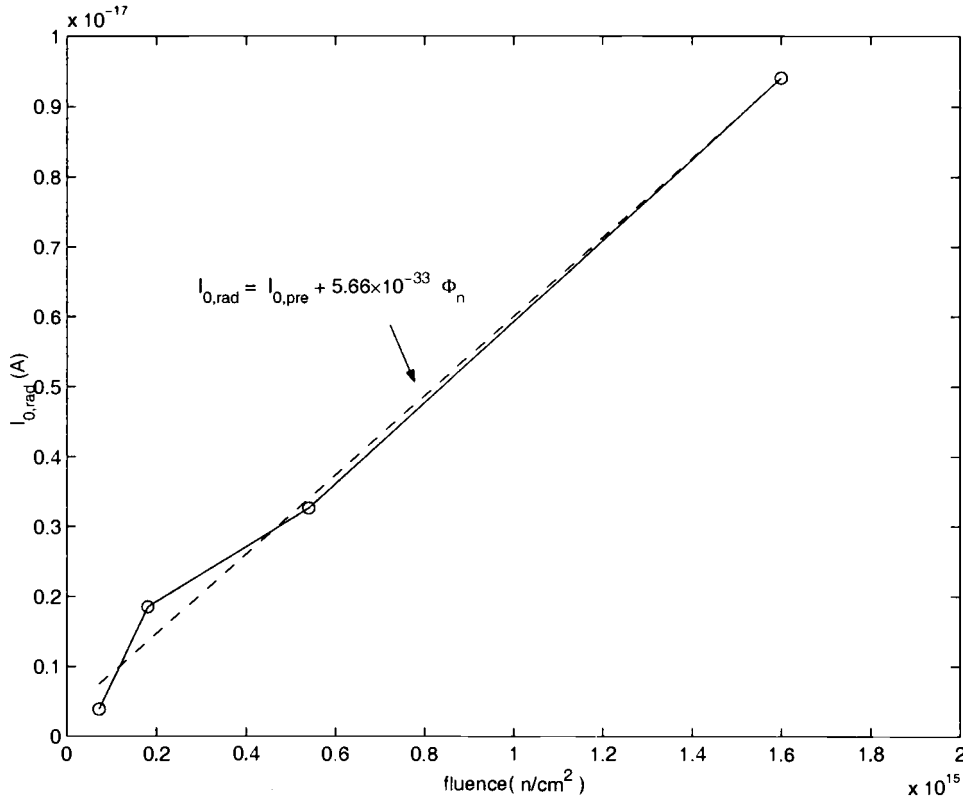
FIGURE 5.7. $I_{0,rad}$, as a function of neutron fluence.

Fig. 5.9 shows the degradation of L-I characteristics versus neutron fluence. The overall intensity is obtained by integrating the intensity counts over the scanned wavelength. The emission intensity is linearly dependent on the injection current for both the pre- and post-irradiated LEDs. And the emission intensity at a constant current decreases with increasing neutron fluence. Please note that the sample exposed to the highest neutron fluence is not shown in this figure, due to the difficulty of injecting desired current. Moreover, the samples exposed to the same neutron fluence but at different dose rate (100kW and 1MW) show almost identical L-I characteristcs, indicating our GaN LEDs are not sensitive to the dose rate effect.
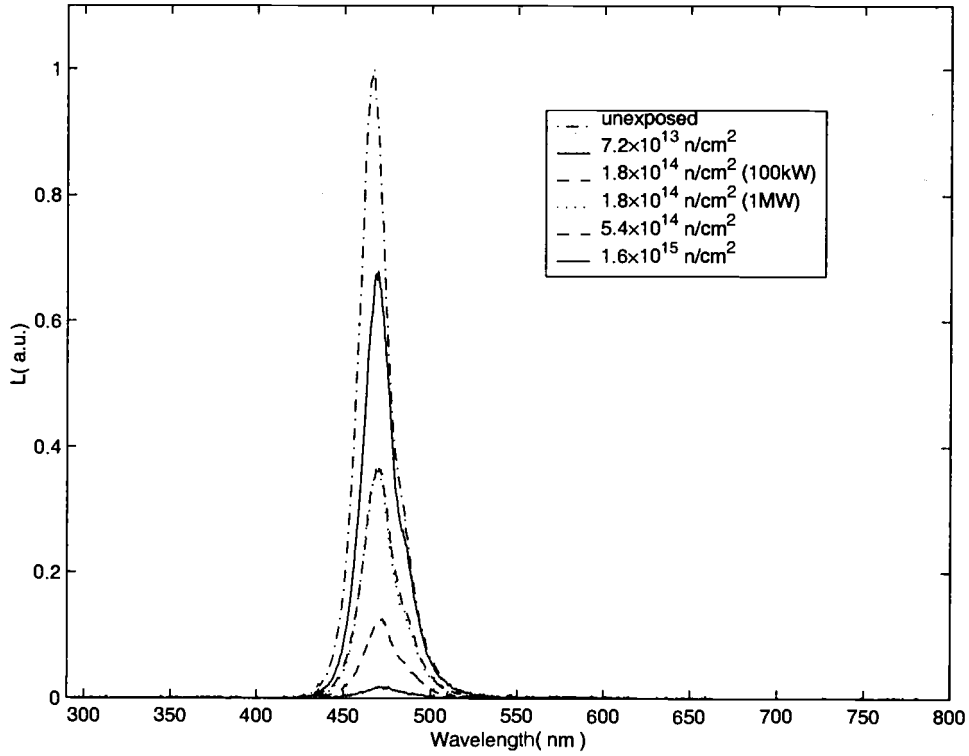
FIGURE 5.8. Emission spectra of GaN LEDs at a constant injection current before and after neutron irradiation.

Fig. 5.10 shows the degradation of LED light intensity after neutron irradiation. The light output (L) is normalized to the initial light output (L_0). The light output degrades with increasing neutron fluence, indicating that nonradiative recombination centers which compete with radiative centers for excess carriers are introduced by neutron irradiation and hence the overall minority carrier lifetime decreases. The light output degrades almost an order of two in magnitude after 1.6×10^{15} n/cm^2 neutron irradiation, suggesting that most of the current recombined through the neutron irradiation-induced nonradiative centers in the band gap of the active layer in this highly irradiated device.
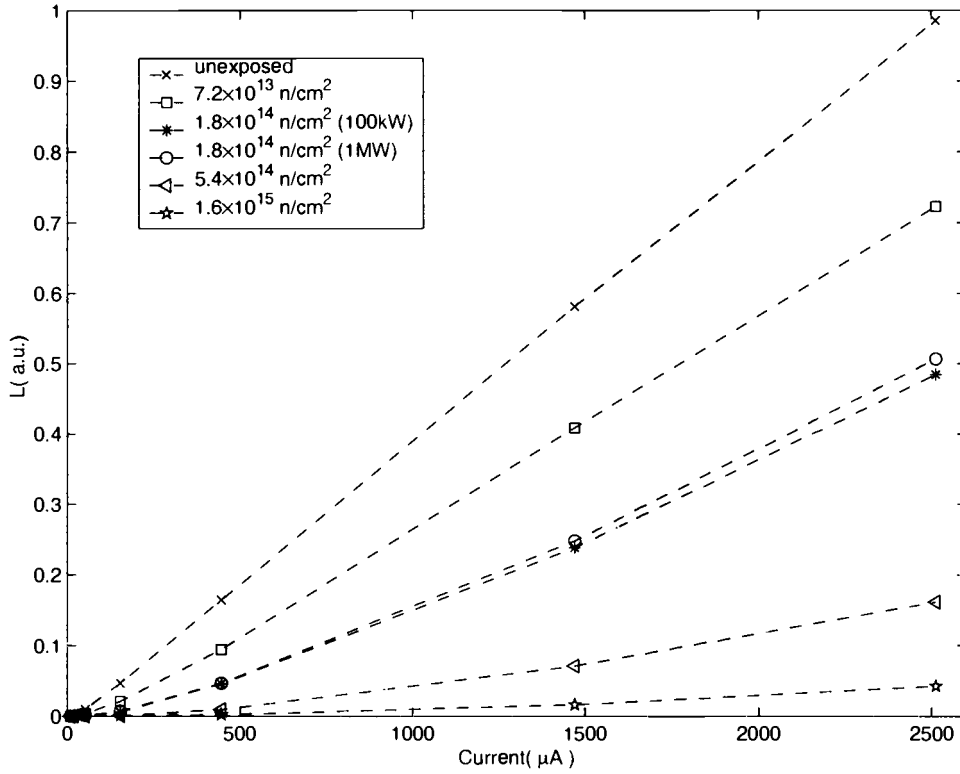
FIGURE 5.9. The degradation of L-I characteristics versus neutron fluence.

As mentioned, the increase of the radiation-induced nonradiative recombination centers may reduce the minority carrier lifetime. Thus, the minority carrier lifetime after neutron irradiation (τ) may be written as

$$1/\tau = 1/\tau_0 + 1/\tau_{I,NR} = 1/\tau_{0,R} + 1/\tau_{0,NR} + 1/\tau_{I,NR} \tag{5.9}$$

where τ_0 is total minority carrier lifetime before neutron irradiation, $\tau_{0,R}$ and $\tau_{0,NR}$ are the lifetime associated with radiative and nonradiative process before neutron irradiation and $\tau_{I,NR}$ is the lifetime associated with the induced nonradiative recombination centers, and may be written as

$$1/\tau_{I,NR} = \sigma_{I,NR} \times v_{th} \times N_{I,NR} \tag{5.10}$$
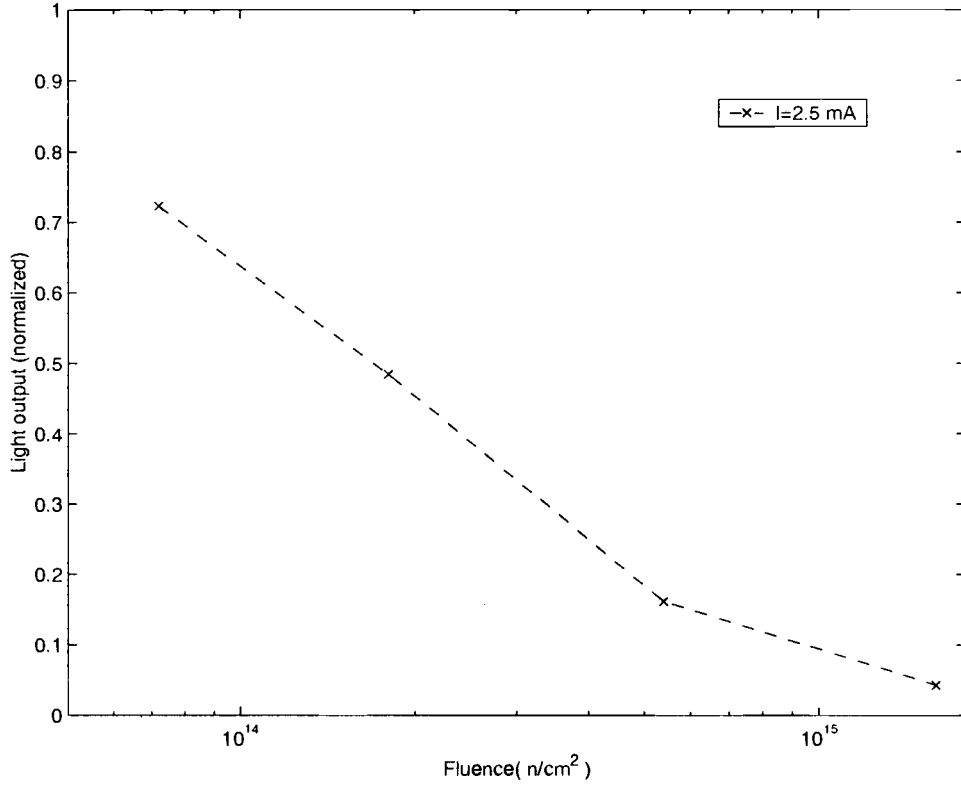
FIGURE 5.10. The degradation of LED light output after neutron irradiation.

where $\sigma_{I,NR}$ is carrier capture cross section associated with radiation-introduced nonradiative centers, v_{th} is the minority carrier thermal velocity, and $N_{I,NR}$ is the concentration of the radiation-introduced nonradiative centers. Thus, eq. 5.9 can be rewritten as

$$1/\tau = 1/\tau_0 + \sigma_{I,NR} \times v_{th} \times N_{I,NR} \tag{5.11}$$

The concentration of the radiation-introduced nonradiative centers, $N_{I,NR}$, may be defined as

$$N_{I,NR} = C_I \times \Phi \tag{5.12}$$

where C_I is a constant, Φ is the radiation fluence. Thus, eq. 5.11 may be rewriten as

$$1/\tau = 1/\tau_0 + \sigma_{I,NR} v_{th} C_I \Phi = 1/\tau_0 + K_\tau \Phi \qquad (5.13)$$

or

$$\tau_0/\tau = 1 + \tau_0 K_\tau \Phi \qquad (5.14)$$

where K_τ is the carrier lifetime damage coefficient and defined as

$$K_\tau = \sigma_{I,NR} \times v_{th} \times C_I \qquad (5.15)$$

Thus, eq. 5.14 provides the measure of radiation damage due to displacements. However, the measureable quantities in LEDs are the total light output and current as a function of the forward bias. Thus, the total minority carrier lifetime for LED is usually evaluated through light output rather than through direct measurement. In a conventional amphoterically doped LED, the light output, L, may be expressed as [80]

$$L = C_L \times \tau \times exp(qV/kT) \qquad (5.16)$$

where C_L is a constant. Thus, at a constant voltage, eq. 5.14 may be rearranged as

$$L_0/L = \tau_0/\tau = 1 + \tau_0 K_\tau \Phi = 1 + K_L \Phi_n \qquad (5.17)$$

where L_0 and L are the light outputs before and after irradiation, respectively; and K_L is the damage coefficient of the light output. However, the double heterojunction LEDs may not obey the relation derived for conventional amphoterically doped LEDs. Fig. 5.11 shows the measured $log(L_0/L) - 1$ as a function of neutron fluence $(\log(\Phi_n))$ at a constant bias voltage. The relation between L_0/L and Φ_n for our GaN DH LEDs may be better expressed as
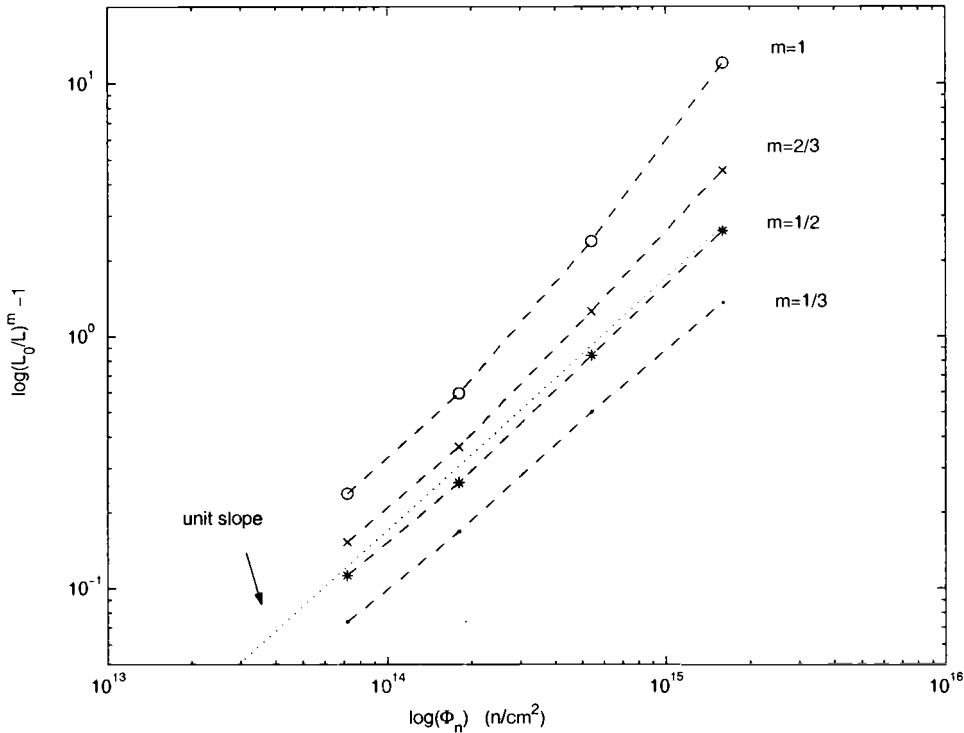
FIGURE 5.11. $\log(L_0/L)$ as a function of $\log(\Phi_n)$ at a constant voltage.

$$(L_0/L)^m = 1 + K_{L,v}\Phi_n \qquad (5.18)$$

where m is a constant. According to Fig. 5.11, the best fitted m is about $1/2$. Thus, the damage coefficent for a constant voltage, $K_{L,v}$, may be extracted from the slope of $[(L_0/L)^{1/2} - 1]$ - Φ_n curves (Fig. 5.12). The estimated $K_{L,v}$ for our LEDs is about 1.63×10^{-15} cm^2/n.

However, the LEDs are usually operated at a constant current rather than at a constant voltage. Thus, it would be useful to obtain the damage coefficient for LEDs operated at a constant current. Rose and Barnes derived the relationship for a conventional amphoterically doped LED at a constant current [80]

$$\left(\frac{L_0}{L}\right)^n - 1 = K_L\Phi \qquad (5.19)$$
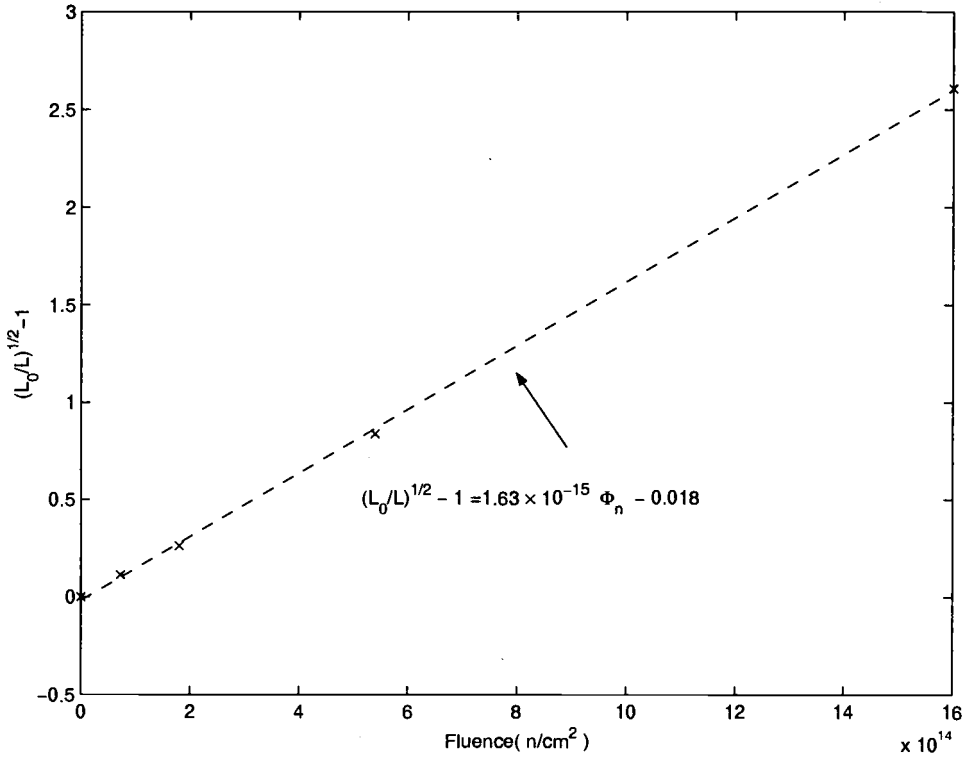
FIGURE 5.12. $(L_0/L)^{1/2} - 1$ as a function of Φ_n at a constant voltage.

where the value of n will depend on the mechanisms that control the light output and total current. If both of the light output and total current are diffusion controlled, $n=2/3$. On the other hand, if the light output is diffusion controlled and total current is controlled by space-charge recombination, $n=1/3$. However, due to the different mechanism that controls the injection current in our LEDs, the relation would be very complicated if the approach similar to the one Rose and Barnes did for conventional amphoterically doped LEDs is taken. Moreover, it has been reported that DH LEDs do not fit the relation (eq. 5.19) well and the more straightforward approach of evaluating normalized damage (L/L_0) is suggested [81]. Thus, for our GaN DH LEDs, the emission degradation at a constant current would be better expressed simply by normalized damage (L/L_0) as a function of neutron fluence

(Φ_n). Fig. 5.13 shows the normalized damage (L/L_0) as a function of neutron fluence (Φ_n) at two constant injection currents.
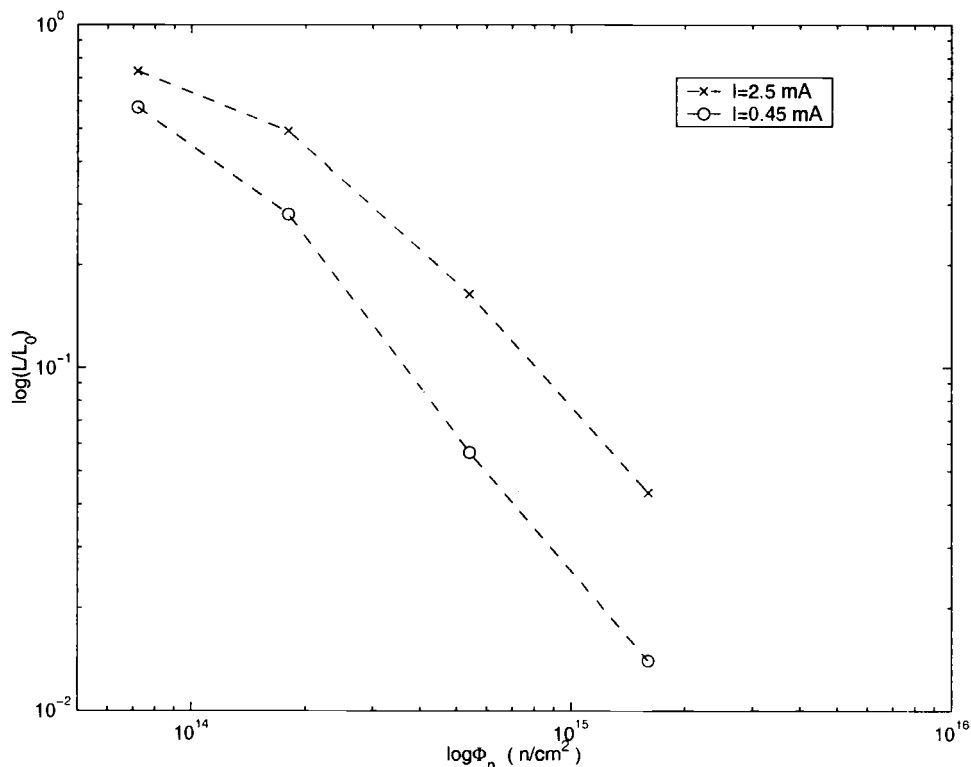
FIGURE 5.13. The normalized damage (L/L_0) as a function of neutron fluence (Φ_n) at two injection currents (0.45 mA and 2.5 mA).

According to Fig. 5.13, the normalized damage (L/L_0) is smaller at the higher operating current (2.5 mA), suggesting that GaN DH LEDs employed in the radiation environment should operate at the higher current where the radiation damage could be minimized.

5.5. Injection-enhanced annealing

It has been reported that applying a forward current to the damaged LED may help anneal the radiation damage [81, 82]. This effect is called injection-enhanced annealing effect. Fig. 5.14 shows the I-V characteristics of the pre- and post-annealing LED which has been exposed to 1.6×10^{15} n/cm^2 neutron irradiation. This figure shows slightly increase in the slope of curves (or increasing α value in eq. 5.2) and significant decreasing of I_0, indicating a lower defect density in GaN layer after 25 hours annealing. However, very little change shows after 25 hours of annealing.

FIGURE 5.14. I-V characteristics of the pre- and post-annealing LED which has been exposed to 1.6×10^{15} n/cm^2 neutron irradiation.

Fig. 5.15 shows the I-V characteristics of the pre- and post-annealing LED which has been exposed to the highest fluence (4.3×10^{15} n/cm^2) neutron irradiation. In this figure, the current shows significant decrease in the lower bias region, implying the neutron irradiation may introduce an unknown current component which is suppressed by the current annealing. F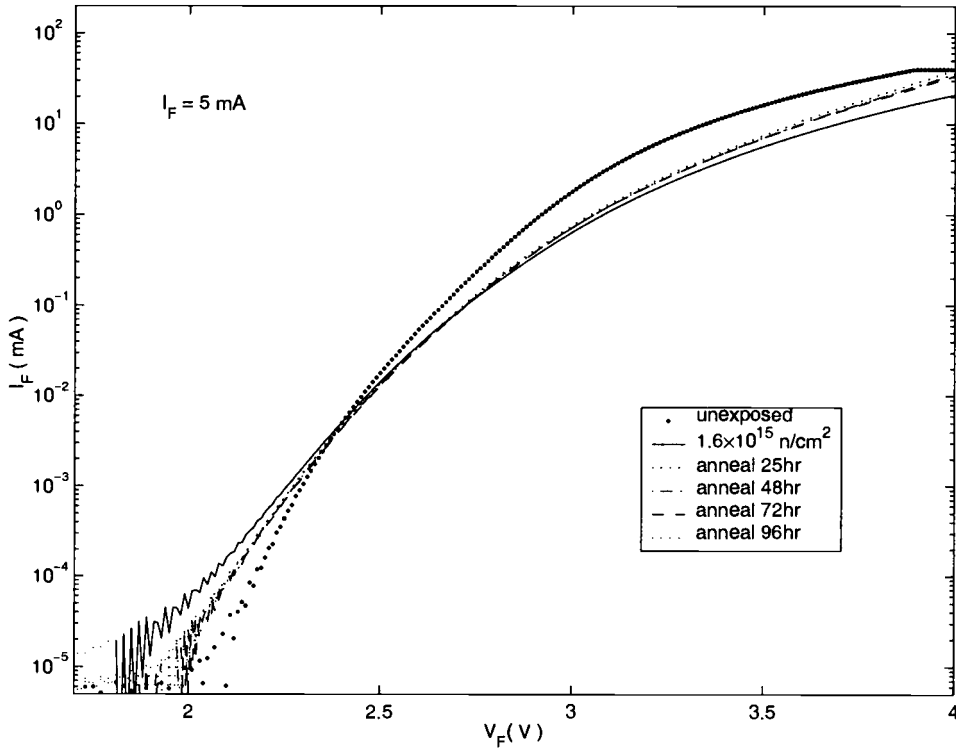ig. 5.16 shows the light output characteristics of the pre- and post-annealing LED which has been exposed to 1.6×10^{15} n/cm^2 neutron irradiation. The light output keeps increasing as the injection charge increases. However, the light output starts to degrade after 96 hours of annealing, indicating the aging effect becomes significant. The light output increases significantly (500%) after 72 hours of annealing, however, the overall light output after annealing is still only 15% of the pre-irradiated light output, indicating most neutron-induced defects may be defect clusters which are hard to be removed by injection-enhanced annealing.

5.6. Conclusion

This study has examined various aspects of radiation damage in GaN LEDs. Neutron irradiation may cause change in the I-V characteristics as well as light output. The atomic displacement is responsible for both of the electrical and optical degradations. The decreasing α value after irradiation may be attributed to the neutron irradiation induced carrier removal effect, while the increasing value of I_0 after irradiation may be attributed to the increasing trap concentration, N_T, after irradiation. Both electrical and optical properties degrade steadily in the low and medium neutron fluence. However, much more severe degradation is shown at the highest neutron fluence. The light output degrades almost 99% after 1.6×10^{15} n/cm^2 neutron irradiation, and the radiation-induced performance degradation depends on operating current and is generally less at higher operating currents.
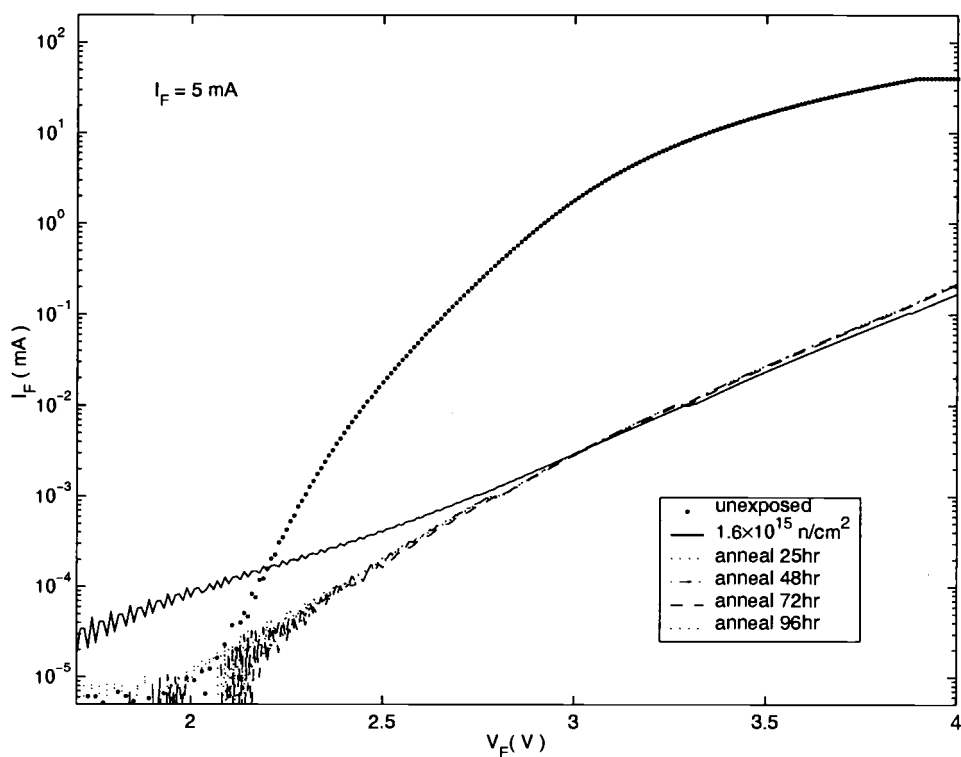
FIGURE 5.15. I-V characteristics of the pre- and post-annealing LED which has been exposed to 4.3×10^{15} n/cm^2 neutron irradiation.
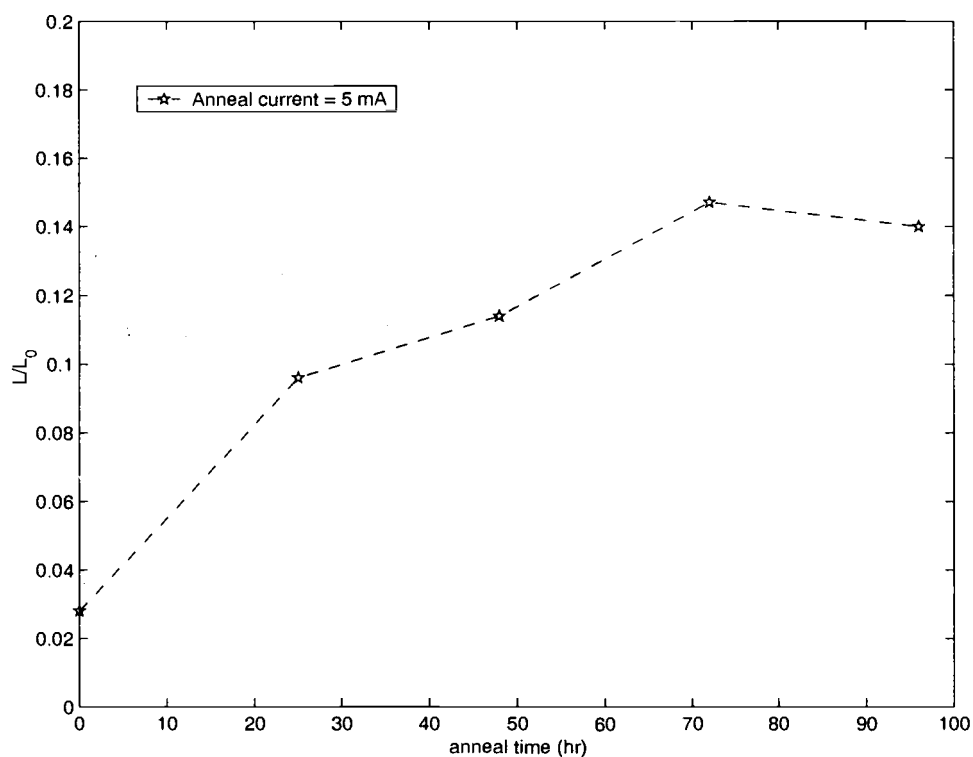
FIGURE 5.16. The light output characteristics of the pre- and post-annealing LED which has been exposed to 1.6×10^{15} n/cm^2 neutron irradiation (L_0 is pre-irradiated light output).

6. CONCLUSIONS AND FURTHER RESEARCH

6.1. Conclusions

This thesis has presented the study of radiation-induced degradation of III-V materials and heterojunction devices. Proton irradiation effects in InGaP/GaAs HBTs are studied as well as neutron irradiation effects in GaN heterojunction LEDs. Various aspects of radiation damage in both devices (HBTs and LEDs) are examined. After a review of the fundamentals of heterojunctions and operation of HBTs, the parameter extraction method and the extended Ebers-Moll (EM) model for HBTs are developed.

InGaP/GaAs HBTs are investigated for high energy (67 and 105 MeV) proton irradiation effects while GaN heterojunction LEDs are studied for neutron irradiation effects. A compact model and the parameter extraction procedures for HBTs are developed, and hence the $I_C - V_{CE}$ characteristics of pre- and post-irradiation HBTs can be simulated by employing the developed model.

HBTs are electrically characterized before and after proton irradiation. Overall, the studied HBT devices are quite robust against high energy proton irradiation. The most pronounced radiation effect shown in SHBTs is the gain degradation. The radiation-induced excess current is the cause of the current gain degradation. The displace damage in the bulk of the base-emitter space-charge region, leading to the excess base current, is the resiponsible mechanism for the proton-induced gain degraidation. On the other hand, the ionization effect which could introduce negative charges in the polyimide passivation layer may cause an accumulation layer in the base region and reduce the surface recombination, leading to a suppression of the base leakage current ($I_{B,lk}$). These accumulated charges are responsible for

the current gain improvement of the HBTs after low fluence proton irradiation. The performance degradation depends on operation current and is generally less at higher currents. Compared to the MBE grown devices, the MOVPE grown HBTs show superior characteristics both in initial performance and in proton irradiation hardness. The 67 MeV protons may do more damage than 105 MeV protons, due to their higher value of NIEL. Moreover, the MOVPE samples show good correlation between NIEL and damage coefficient, while MBE samples show some deviation from the correlation. Finally, the HBT I-V characteristcs of pre- and post-irradiated samples can be simulated successfully by employing the developed model.

GaN heterojunction LEDs are electrically and optically characterized before and after neutron irradiation. Neutron irradiation may cause degradation of I-V characteristics and light output. Both electrical and optical properties degrad steadily in the low and medium neutron fluence. However, much more severe degradation is shown at highest neutron fluence. Atomic displacement is responsible for both electrical and optical degradation. The forward current under a constant bias degrades after the neutron irradiation. Possible mechanisms responsible for the current degradation are the neutron-induced trap states and the carrier removal effect. The light output intensity of LEDs under a constant forward current also shows degradation after neutron irradiation. However, there is no siginigicant wavelength shift nor new illumination peak shown after neutron irradiation. The possible responsible mechanism for this neutron-induced light output degradation is the neutron-induced non-radiative recombination centers inside the active layer. The light output degrades by almost 99% after 1.6×10^{15} n/cm^2 neutron irradiation, and the radiation damage depends on operation current and is generally less at higher currents.

6.2. Further Research

Our InGaP/GaAs HBTs are quite robust against the high energy protons and show limited degradation after being exposed to the high-energy proton irradiation. In order to investigate the degradation response of these HBTs for proton irradiation, the higher proton fluence is desired. However, due to the irradiation facility and beam-time limitations, the higher proton fluence may not be plausible. Thus, the lower energy (e.g. 1-2 MeV) proton is desired, due to their higher NIEL. The more significant degradation may be observed under 1MeV proton irradiation at the same fluence. Moreover, the degradation characteristics of these HBTs under lower lenergy proton irradiation may provide more information of the correlation of NIEL and the damage coefficents.

The proton-induced gain improvement under low fluence as well as the radiation-induced series resistance decrease may need more study. The underlying mechanisms leading to these performance improvement may be useful for the design of better heterojunction devices.

BIBLIOGRAPHY

[1] W. R. Dawes, Jr., F. B. McLean, P. A. Robinson, Jr., and J. J. Silver, *Hardening Semiconductor Components againt Radiation and Temperature*. Noyes Data Corporation, 1989.

[2] W. N. Hess, *The Radiation Belt and the Magnetosphere.*, Blaisdell Publ. Co., 1968.

[3] E. G. Stassinopoulos, and J. P. Raymond, "The Space Radiation Environment for electronics," *Proc. of the IEEE,* col. 76, p1423,1988.

[4] A. Holmes-Siedle and L. Adams, *Handbook of Radiation Effects*. Oxford University Press, 1993.

[5] G. Messenger and M. Ash, *The Effect of Radiation on Electronic Systems*. Van Nostrand Reinhold Company, 1986.

[6] T. P. Cameron, R. Crampton, K. Tan, "High Linearity HBT RFICs Using AlGaAs, InGaP/GaAs, and SiGe Technologies for Basestation Repeater Designs ," *Microwave Product Digest, http://www.mpdigest.com/ Articles/ Jan2001/ stanford/ Default.htm, January*, 2001.

[7] A. Shatalov, S. Subramanian, A. Klein, "Correlation between nonionizing energy loss and the offset voltage shift in InP-InGaAs heterojunction bipolar transistors," *IEEE Trans. Nuc. Sci.,* vol. 48, pp. 2262-2268, 2001.

[8] A. Shatalov, S. Subramanian, S. Chandrasekhar, A Dentai, S. M. Goodnick, "Electron irradiation effects in polyimide passivated InP/InGaAs single heterojunction bipolar transistors," *IEEE Trans. Nuc. Sci.,* vol. 46, pp. 1708-1715, 1999.

[9] A. Shatalov, S. Subramanian, A Dentai, "Neutron irradiation effects in InP/InGaAs single heterojunction bipolar transistors," *IEEE Trans. Nuc. Sci.,* vol. 47, pp. 2551-2556, 2000.

[10] A. Sarkar, S. Subramanian, L. Ungier, S. M. Goodnick," Integrity of III-V heterojunction interfaces under gamma irradiation," *IEEE Trans. Nuc. Sci.,* vol. 44, pp. 1862-1869 1997.

[11] Y. Song, M. E. Kim, A. E. Oki, M. E. Hafizi, W. D. Murlin, J. B. Camou, and K. W. Kobayashi, " Effect of Neutron irradiation on GaAs/AlGaAs Hetrojunction Bipolar transistors," *IEEE Trans. Nuc. Sci.,* vol. 36, pp. 2155-2160, 1989.

[12] G. A. Schrantz, N. W. van Vonno, W. A. Krull, M. A. Rao, S. I. Long, and
H. Kromer, " Neutron irradiaton effects on AlGaAs/GaAs hetrojunction bipolar
transistors," *IEEE Trans. Nuc. Sci.,* vol. 35, pp. 1657-1661 1988.

[13] K. F. Brennan, P. K. Chiang, "Carbon-Doped InGaP/GaAs/InGaP Double
Hetrojunction Bipolar Transistors," *IEEE Trans. Electron Devices,* vol. 39, p.
2657, 1992.

[14] N. Pan *et al.,* "Hgih reliability InGaP/GaAs HBT," *IEEE Electron Devices
Lett.,* vol. 19, pp. 115-117, 1998.

[15] T. Chung, S. R. Bank, J. Epple and K. Hsieh, "Current Gain Dependence
on Subcollector and Etch-Stop Doping in InGaP/GaAs HBTs," *IEEE Trans.
Electron Devices,* vol. 48, p. 835, 2001.

[16] D. Scherrer, J. Kruse, J. Laskar, M. Feng, M. Wada, C. Takano, and J. Kasa-
hara, " Low-power performance of 0.5- m JFET for low-cost MMIC s in personal
communications," *IEEE Electron Device Lett.,* vol. 14, pp. 428-430, Sept. 1993.

[17] H. Kroemer, "Heterostructure bipolar transistors and integrated circuits," *Proc.
IEEE,* vol. 70, pp. 13-25, Jan. 1982.

[18] P. Asbeck, F. Chang, K.-C. Wang, G. Sullivan, and D. Cheung, " GaAsbased
heterojunction bipolar transistors for very high performance electronic circuits,"
IEEE Electron Device Lett., vol. 81, pp. 1709 1726, Dec. 1993.

[19] H. Kroemer, "Heterostructure bipolar transistors and integrated circuits," *Proc.
IEEE,* vol. 70, pp. 13-25, Jan. 1982.

[20] G. A. Baraff, J. A. Appelbaum, and D. R. Hamann, *Phys. Rev. Lett.,* vol. 38,
pp. 237, 1976

[21] R. L. Anderson, *Solid-State Electron.,* vol. 5, pp. 341, 1962.

[22] J. Batey and S. L. Wright, "Energy band alignment in GaAs:(Al,Ga)As Het-
erostructures: The dependence on alloy compositions ," *Journal of Applied
Physics* vol. 59, pp. 200-209, 1986.

[23] T. Kobayashi, K. Taira, F. Nakamura and H. Kawai, "Band lineup for a
GaInP/GaAs heterojunction measured by a high gain N-p-n heterojunction
bipolar transistor grown by metalorganic chemical vapor deposition ," *Journal
of Applied Physics* vol. 65, pp. 4849-4902, 1989.

[24] D. V. Lang, M. B. Panish, F. Capasso, J. Allam, R. A. Hamm, A. M. Sergent and
W. T. Tsang, " Measurement of Heterojunction Band Offsets by Admittance
Spectroscopy: " InP/Ga0.47In0.53As"," *Appied Physics Letter* vol. 50,NO. 12,
pp. 736 - 738, 1987.

[25] P. M. Asbeck, M. F.Chang, J. A. Higgins, N. H. Sheng, N. H. Sheng, G. J. Sullivan, and K. Wang, "GaAlAS/GaAs Heterojunction Bipolar Transistors: Issue and Prospects for Application," *IEEE Trans. Electron Devices,* vol. 36, pp. 2032-2042, 1989

[26] F. Ali and A. Gupta, editors, *HEMTs and HBTs: devices, fabrication and circuits.* Artech House, 1991.

[27] M. Razeghi, F. Omnes, M. Defour, Ph. Maurel, J. Hu, and D. Pavlidis, "High performance GaAs/GaInP HBT s grown by MOCVD," *Sem. Sci. Technol.,* vol. 5, pp. 278-280, 1990.

[28] G. I. Ng, D. Pavlidis, A. Samelis, D. Pehlke, J. C. Garcia, and J. P. Hirtz, "Demonstration of GaInP/GaAs HBT s grown with reduced toxicity all-metalorganic precursors," *IEEE Int. Conf. Indium Phosphide and Related Materials,* pp. 399-402, 1994.

[29] T. Takahashi, S. Sasa, A. Kawano, T. Iwai, and T. Fujii, " High-Reliability In-GaP/GaAs HBT s Fabricated by Self-Aligned Process," *Proc. IEEE Int. Electron Device Meeting (IEDM),* pp. 191-192, San Francisco, CA, 1994.

[30] J.-W. Park, S. Mohammadi, D. Pavlidis, C. Dua, J. Guyaux, and J. C. Garcia, "GaInP/GaAs HBT broadband monolithic transimpedance amplifiers and their high frequency small and large signal characteristics ," *IEEE MTT-S Int. Microwave Symp.,* pp.39-42, 1998.

[31] S. Mohammadi, J.-W. Park, D. Pavlidis, C. Dua, J. Guyaux, and J. C. Garcia, " High-gain GaInP/GaAs HBT monolithic transimpedance amplifier for high-speed optoelectronic receivers," *Proc. IEEE Int. Electron Device Meeting (IEDM),* pp. 661-664, San Francisco, CA, 1998.

[32] S. Kobayashi, T. Fujita, T. Yakihara, S. Oka, and A. Miura, "Ultrahighspeed InGaP/InGaAs HBT s using MG as the base dopant ," *Proc. Iridium Phosphide and Related Materials ,* pp. 58-61, 1997.

[33] D. Sawdai, J. O. Plouchart, D. Pavlidis, A. Samelis, and K. Hong, "Power performance of InGaAs/InP single HBTs," *IPRM Conference,* 1996

[34] A. Bandyopadhyay, S. Subramanian,S. Chandrasekhar, A. G. Dentai, S. M. Goodnick, "Degradation of DC Characteristics of InGaAs/InP Single Heterojunction Bipolar Transistors under Electron Irradiation ," *IEEE trans. Nuc. Sci.,* Vol. 46, NO. 5, pp. 840-849, 1999.

[35] G. Massobrio, P. Antognetti, *Semiconductor Device Modeling with SPICE ,* Mcgraw-Hill Inc., 1993.

[36] H. Lin, S. Lee, "Super-gain AlGaAs/GaAs heterojunction bipolar transistors using an emitter edge-thining design," *Appl. Phys. Lett.* , Vol. 47, pp. 839-841, 1985.

[37] J. J. Liou, C. I, Huang, B, Bayraktaroglu, D. C., Williamson, and K. B. Parab., " Base and collector leakage currents of AlGaAs/GaAs heterojunction bipolar tansistor ," *J. Appl. Phys.* , Vol. 76, NO. 5, pp. 3187-3193, 1994.

[38] D. Caffin, A. M. Duchenois, F. Heliot, C. Besombes, J. L. Benchimol, and P. Launay, " Base-collector leakage currents in InP/InGaAs double heterojunction bipolar tansistor ," *IEEE Trans. Electron Devices* , Vol. 44, NO. 6, pp. 930-936, 1997.

[39] G. Stassinopoulos, and J. P. Raymond, " The Space Radiation Environment for Electronics ," *Proc. of the IEEE* , Vol. 76, pp. 1423-1441, 1988.

[40] D. Hastings, H. Garrett, *Spacecraft Environment Interactions.* , Cambridge University Press, 1996.

[41] M. A. Xapsos, G. P. Summer, C. C. Blatchley, C. W. Colerico, E. A. Burke, S. R. Messenger, " Co^{60} gamma ray and electron displacement damage studies of semiconductors." *IEEE Trans. Nuc. Sci.* , Vol. 41,NO 6, pp. 1945-1949, 1994.

[42] B. R. Gossick, *J. App. Phys.* , Vol. 30, p. 1214, 1959.

[43] V. A. J. van Lint, R. E. Leadon and J. F. Colwell,, *IEEE Trans. Nuc. Sci.* , Vol. 19, p. 181, 1972.

[44] G. P. Summers, E. A. Burke, C. J. Dale, E. A. Wolicki, P. W. Marshall ,and M. A. Gehlhausen, " Correlation of particle-induced displacement damage in silicon." *IEEE Trans. Nuc. Sci.* , Vol. 34,NO 6, pp. 1134-1139, 1987.

[45] J. R. Srours, J. M. McGarrity, " Radiation effects in Microelectronics in space." *Proceedings of the IEEE* , Vol. 76, pp. 1443-1469, 1988.

[46] G. P. Summers, E. A. Burke, P. Shapiro,S. R. Messenger, and R. J. Walters, "Damage correlation in semiconductors exposed to gamma, electron and proton radiations." *IEEE Trans. Nuc. Sci.* , Vol. 40, NO 6, pp. 1372-1379, 1993.

[47] J. Lindhard, V. Nielsen, M. Scarff and P. V. Tomsen, "Integral equations governing radiation effects." *Mat. Fys. Medd. Dan. Vid. Selsk* , Vol. 33, NO 10, pp. 1-42, 1963.

[48] E. A. Burke, C. J. Dale, A. B. Campbell, G. P. Summers, W. J. Stapor, M. A. Xapsos, T. Palmer, and R. Zuleeg, "Energy dependence of proton-induced displacement damage in Gallium Arsenide" *IEEE Trans. Nuc. Sci.* , Vol. 34, NO 6, pp. 1220-1226, 1987.

[49] A. L. Barry, A. J. Houdayer, P.F. Hinrichsen, W. G. Letourneau, and J. Vincent, "The energy dependence of lifetime damage constants in GaAs LEDs for 1-500 MeV protons" *IEEE Trans. Nuc. Sci.* , Vol. 42, NO 6, pp. 2104-2107, 1995.

[50] A. H. Johnston, C. I. Lee, and B. G. Rax, "Enhanced Damage in bipolar devices at low dose rates: Effects at very low dose rates." *IEEE Trans. Nuc. Sci.* , Vol. 43, NO 6, pp. 3049-3059, 1996.

[51] M. Yamaguchi, C. Uemura and A. Yamamoto, "Radiation damage in InP single crystals and solar cells" *J. Appl. Phys.* , Vol. 55, pp. 1429-1436, 1984.

[52] B. E. Anspaugh, "Proton and electron damage coefficients for GaAs/Ge solar cells" *Proceedings of Twenty-Second IEEE PVSC* , pp. 1593-1598, 1992.

[53] Y. Yamaguchi and C. Amino, "Co-60 gamma ray and electron irradiation of GaAs single crystals and solar cells" *J. Appl. Phys.* , Vol. 54, pp. 5021-5029, 1983.

[54] J. R. Carter and R. G. Downing, "Charged particles radiation damage in semiconductors, XI: Effects of low energy protons and high energy electrons on silicon" *Interim Technical Final Report* , TRW Space Technology Laboratories, May 1965.

[55] T, Noguchi and M. Uesugi, "Electron energy dependence of relative damage coefficients of silicon solar cells for space use" *Technical Digest of the International PVSEC-5* , Tokyo, Japan, 1990.

[56] J. Roldan, W. E. Ansley, J. D. Cressler, S. D. Clark and Nguyen-Ngoc, "Neutron radiation tolerance of advanced UHV/CVD SiGe HBTs," *IEEE Trans. Nuc. Sci.* , Vol. 44, No 6, pp. 1965-1973, 1997.

[57] S. Zhang, G. Niu, J. D. Cressler, S. D. Clark and D. Ahlgren, "The effects of protin irradiation on RF performance of SiGe HBTs," *IEEE Trans. Nuc. Sci.* , Vol. 46, No 6, pp. 1716-1721, 1999.

[58] Y. Song, M. E. Kim, A. K. Oki, M. E. Hafizi, W. D. Murlin, J. B. Camou and K. W. Kobayashi, "Effects of neutron irradiation on GaAs/AlGaAs heterojunction bipolar transistors," *IEEE Trans. Nuc. Sci.* , Vol. 36, pp. 2155-2160, 1989.

[59] J. Roldan, G. Niu, W. E. Ansley, J. D. Cressler and S. D. Clark, "An investigation of the spatial location of proton-induced traps in SiGe HBT's," *IEEE Trans. Nuc. Sci.* , Vol. 45, pp. 2424-2430, 1998.

[60] E. W. Enlow, R. L. Pease, W. E. Combs, R. D. Schrimpf and R. N. Nowlin, "Response of advanced bipolar processes to ionizing radiation," *IEEE Trans. Nuc. Sci.* , Vol. 38, pp. 1342-1351, 1991.

[61] L. W. Aukerman and R. D Graft, "Annealing of electron irradiated GaAs," *Phys. Rev.* , Vol. 127, pp. 1576-1583, 1962.

[62] O. Yu. Borkovskaya, N. L. Dmitruk, V. G. Litovchenko and O.N. Mishchuk, "Model of the radiation-stimulated ordering effect in III-V semiconductors," *Sov. Phy. Semicond.* , Vol. 23, pp. 129-132, 1989.

[63] A. Jorio, M. Parenteau, M. Aubin, C. Carlone, S. M. Khanna, and J. W. Gerdes Jr., "A mobility study of the radiation induced order effect in gallium arsenide," *IEEE Trans. Nuc. Sci.* , Vol. 41, No. 6, pp. 1937-1944, 1994.

[64] S. M. Khanna, C. Rejeb, A. Jorio, M. Parenteau, C. Carlone and J. W. Gerdes Jr., "Electron and neutron radiation-induced order effect in gallium arsenide," *IEEE Trans. Nuc. Sci.* , Vol. 40, pp. 1350-1359, 1993.

[65] H. Ghamlouch, M. Aubin, C. Carlone and S. M. Khanna, "Electron irradiation of GaAs: Improvement of transport properties and observation of DX-like centers at ambient pressure," *J. Appl. Phys.* , Vol. 74, No.7, pp. 4357-4362, 1993.

[66] A. Wu, R. D. Schrimpf, H. J. Fleetwood, R. L. Pease and S. L. Kosier, "Radiation-induced gain degradation in lateral PNP BJTs with lightly and heavily doped emitters," *IEEE Trans. Nuc. Sci.* , Vol. 44, No.6, pp. 1914-1921, 1997.

[67] A. Shatalov, "Radiation effects on III-V semiconductors and heterojunction bipolar transistors," *Ph.D. Thesis* , Oregon State University, Corvallis, OR, 2000.

[68] B. Jun, "Radiation effects on III-V heterostructure devices," *Ph.D. Thesis* , Oregon State University, Corvallis, OR, 2002.

[69] J. I. Pankov, E. A. Miller and J. E. Berkeyheiser, *RCA Rev.* , Vol. 32, p. 383, 1971.

[70] S. Nakamura, M. Senoh, N. Iwasa and S.I. Nagahama, "High-Brightness InGaN Blue, Green and Yellow Light-Emitting Diodes with Quantum Well Structures," *apanese Journal of Applied Physics, letters* , Vol. 34, pp. 797-799, 1995.

[71] S. M. Khanna, J. Webb, H. Tamg, A. J. Houdayer and C. Carlone, "2 MeV proton radiation damage studies of gallium nitride films through low temperature photoluminescence spectroscopy measurements," *IEEE Trans. Nuc. Sci.* , Vol. 47, NO. 6, pp. 2322-2328, 2000.

[72] S. M. Khanna, D. Estan, H. C. Liu, M. Gao, M. Buchanan and A. J. SpringThorpe, "1-15 MeV proton and alpha particle radiation effects on GaAs quantum

well kight emitting diodes," *IEEE Trans. Nuc. Sci.* , Vol. 47, NO. 6, pp. 2508-2514, 2000.

[73] F. Gaudreau, C. carlone,A. Houdayer and S. M. Hhanna, "Spectral properties of proton irradiated gallium nitride blue diodes," *IEEE Trans. Nuc. Sci.* , Vol. 48, NO. 6, pp. 1778-1784, 2001.

[74] Y. Narukawa, Y. Kawakami, M. Funato, S. Fujita, and S.Nakamura, *Appl. Phys. Lett.* , Vol. 70, p. 981, 1997.

[75] W. Shan, B. D. Little, J. J. Song, Z. C. Feng, M. Schurman and R. A. Stall, *Appl. Phys. Lett.* , Vol. 69, p. 3315, 1996.

[76] P. Perlin, V. Iota,B. A. Weinstein, P. Wisniewski, T. Suski, P. G. Eliseev and M. Osinski, *Appl. Phys. Lett.* , Vol. 70, p. 2993, 1997.

[77] H. C. Casey, J. Muth, S. Krishnankutty and J. M. Zavada, "Dominance of tunneling current and band filling in InGaN/AlGaN diode heterostructure blue light-emitting diodes, *Appl. Phys. Lett.* , Vol. 68, pp. 2867-2869, 1996.

[78] I. Martil, E. Redondo and A. Ojeda, "Influence of defects on the electrical and optical characteristics of blue light-emitting diodes based on III-V nitrides," *J. Appl Physi.* , Vol. 81, NO 5, pp. 2442-2444, 1997.

[79] D. C. Look, D. C. Reyolds, J. W. Hemsky, J. R. Sizelove, R. L'Jones and R. J. Molnar, "Defect donor and aceeptor in GaN," *Physcal Review Letter* , Vol. 81, NO 5, pp. 2442-2444, 1997.

[80] B. H. Rose and C. E. Barnes, "Proton damage effects on light emitting diodes," *J. Appl. Phys.* , Vol. 43, pp. 1772-1780, 1982.

[81] A. H. Johnston and T. F. Miyahira, "Characterization of proton damage in light emitting diodes," *IEEE Trans. Nuc. Sci.* , Vol. 47, NO. 6, pp. 1778-1784, 2000.

[82] A. H. Johnston, "Proton displacement damage in light emitting and laser diodes," *IEEE Trans. Nuc. Sci.* , Vol. 48, NO. 6, pp. 1713-1720, 2001.